NATIONAL TECHNICAL UNIVERSITY OF ATHENS
SCHOOL OF NAVAL ARCHITECTURE AND MARINE ENGINEERING
MSc IN NAVAL AND MARINE TECHNOLOGY AND SCIENCE
SHIP BUILDING TECHNOLOGY LABORATORY

MSc THESIS

" Study of Microstructure and Corrosion Behavior of AH36 FSW Welds and HSLA S690 ARC Welds"

Dipl. Mechanical Engineering, NTUA

VASILIKI G. BOUTSALI

Thesis Examination Committee:

Prof. D. I. PANTELIS (Supervisor)

Prof. N. G. TSOUVALIS

Prof. G.-C. VOSNIAKOS

ATHENS 2016

NATIONAL TECHNICAL UNIVERSITY OF ATHENS
SCHOOL OF NAVAL ARCHITECTURE AND MARINE ENGINEERING
MSc IN NAVAL AND MARINE TECHNOLOGY AND SCIENCE
SHIP BUILDING TECHNOLOGY LABORATORY

MSc THESIS

" Study of Microstructure and Corrosion Behavior of AH36 FSW Welds and HSLA S690 ARC Welds"

Dipl. Mechanical Engineering, NTUA

VASILIKI G. BOUTSALI

Thesis Examination Committee:

Prof. D. I. PANTELIS (Supervisor)

Prof. N. G. TSOUVALIS

Prof. G.-C. VOSNIAKOS

ATHENS 2016

Acknowledgements

Mr. Dimitrios I. Pantelis, professor of the school of Naval Architecture and Marine Engineering at National Technical University of Athens, is the first person that I should thank for the award of this thesis. He helped me throughout the preparation of thesis, when it was needed and I am grateful for the confidence he showed in me.

I would also thank Ms. D. Tsiourva, Chemical Engineer and a member of the scientific staff of the Shipbuilding Technology Laboratory. She was very supportive and helpful in what I needed during the experiment procedure and the writing of this thesis.

Then, I thank Mr. G. S. Vosniakos, professor of the school of Mechanical Engineering at National Technical University of Athens, for the opportunity to use the structured white light 3D scanner of Manufacturing Technology Laboratory. The tests conducted by D. Tiris, graduate student, whom I thank too.

All the scientific staff of the laboratory, helped me in everything I needed throughout the experimental procedure, and I am thankful for this.

Final, I really thank my mother and all my friends, who were beside me and supported me throughout both undergraduate, and my postgraduate studies.

Contents

A. THEORITICAL PART

B. EXPERIMENTAL PART

Abstract

This thesis is entitled “Study of microstructure and corrosion behavior of AH36 FSW welds and HSLA S690 ARC welds”. The experiments took place at the Shipbuilding Technology Laboratory of the school of Naval Architecture and Marine Engineering at National Technical University of Athens. The purpose of the thesis is to study and compare the corrosion behavior of arc welding, a conventional welding method, with the friction stir welding, a new method of welding in shipbuilding. Thus, within the present thesis, the microstructure and the corrosion behavior of the above two welds were studied. Moreover, for these welds, two different shipbuilding steels have been used: the common shipbuilding steel (AH36) and a high strength low alloy steel, (HSLA - S690). The HSLA steels are used in recent years in Shipbuilding, as they exhibit improved properties concerning mechanical properties and particularly on the fatigue strength.

Specifically, the metallography of the welds and their micro-hardness are studied initially and then, their corrosion behavior. The study of corrosion was made by two methods: electrochemical and standardized methods of accelerated aging in a salt spray chamber. The electrochemical methods, which were used are the following: the linear polarization, the Tafel and the method of electrochemical impedance. Furthermore, it was attempted to measure the three-dimensional shape of a corroded specimen’s surface and compare it with the surface of a non-corroded one, by using a structured white light 3D scanner.

Finally, substantial conclusions which have arisen through the entire course of this research are noted.

Περίληψη

Η συγκεκριμένη διπλωματική εργασία εκπονήθηκε το έτος 2014-2015 στο εργαστήριο Ναυπηγικής Τεχνολογίας της σχολής Ναυπηγών Μηχανολόγων Μηχανικών του Εθνικού Μετσόβιου Πολυτεχνείου. Στόχος της μελέτης είναι η μελέτη και η σύγκριση της συμπεριφοράς σε διάβρωση της συγκόλλησης τόξου, που αποτελεί συμβατική μέθοδο συγκόλλησης, με τη συγκόλληση διά τριβής μέσω ανάδευσης, που αποτελεί νέα μέθοδο συγκόλλησης στις ναυπηγικές κατασκευές. Έτσι, στο πλαίσιο της παρούσας Μεταπτυχιακής Εργασίας μελετήθηκε η μικροδομή, καθώς και η συμπεριφορά σε διάβρωση των δύο αυτών συγκολλήσεων. Επιπλέον, για τις συγκολλήσεις αυτές έχουν χρησιμοποιηθεί δύο διαφορετικοί χάλυβες ναυπηγικών κατασκευών : ο κοινός ναυπηγικός χάλυβας (AH36), καθώς και ένας χάλυβας υψηλής αντοχής χαμηλής κραμάτωσης (HSLA – S690). Οι Χάλυβες Υψηλής Αντοχής Χαμηλής Κραμάτωσης χρησιμοποιούνται τα τελευταία χρόνια στη Ναυπηγική, δεδομένου ότι παρουσιάζουν βελτιωμένες ιδιότητες, σχετικά με τις μηχανικές τους ιδιότητες και συγκεκριμένα στην αντοχή σε κόπωση.

Ειδικότερα, μελετάται αρχικά η μεταλλογραφία των συγκολλήσεων και η μικρο-σκληρότητά τους και στη συνέχεια η συμπεριφορά τους σε διάβρωση. Η μελέτη του φαινομένου της διάβρωσης έγινε με την εφαρμογή δύο μεθόδων: με ηλεκτροχημικές μεθόδους και με προτυποποιημένες μεθόδους επιταχυνόμενης γήρανσης στο θάλαμο αλατονέφωσης. Στις ηλεκτροχημικές μεθόδους που εφαρμόστηκαν περιλαμβάνεται η μέθοδος της Γραμμικής Πόλωσης, η μέθοδος προεκβολής ευθειών Tafel και η ηλεκτροχημική Εμπέδηση. Επίσης, έγινε και η ψηφιακή αποτύπωση της επιφάνειας διαβρωμένου δοκιμίου και σύγκρισή της με επιφάνεια του δοκιμίου πριν από την έκθεση του σε περιβάλλον διάβρωσης, μέσω τρισδιάστατης σάρωσης με χρήση λευκού δομημένου φωτός.

Τέλος, αναφέρονται, τα συμπεράσματα που προέκυψαν από όλη την πειραματική διαδικασία και η ανάλυση αυτών.

Chapter 1: Welds in Metallic Materials

1.1. Introduction

In all components of human technological activity, seals are an essential part as connection machining, assembly and erection in general structures. With the use of the welding, we can get to 100% of the strength of the metal base to ensure the complete tightness of the connection, while there is no limitation to the thickness in connection plates. Through the welding, the loads are transferred from one part of the structure to the other.

Five big categories of metal binding methods are distinguished:

a. *Fusion welding*, where heat is imparted to the metals in connection to occur fusion.
b. *Electric - resistance* welding, where heat is imparted to the metals in connection with the aim of electric current (Joule phenomenon) and then an external pressure is applied.
c. *Liquid - solid phase* joining, where the metals in connection are heated to obtain heat less than their melting point and simultaneously is added a different metal (with lower melting point), in the liquid state, so that after thawing to create the connection in solid state.
d. *Adhesive* welding, where the connections are created as a result of molecular attraction between the surfaces in connection and the adhesive.

1.2. Joint types [7] [24]

There are five basic types of welding joints, with each having a number of variations in order to meet different needs (***Figure 1.1***):

A. *Butt Joint*. A butt weld, or a square-groove, is the most common and easiest to use. Consisting of two flat pieces that are parallel to one another, it also is an economical option. It is the universally used method of joining a pipe to itself, as well as flanges, valves, fittings, or other equipment.
B. *Corner Joint*. A corner weld is a type of joint that is between two metal parts and is located at right angles to one another in the form of a L. As the name indicates, it is

used to connect two pieces together, forming a corner. This weld is most often used in the sheet metal industry and is performed on the outside edge of the piece.

C. *Edge Joint*. Edge welding joints, a groove type of weld, are placed side by side and welded on the same edge. They are the most commonly replaced type of joints due to build up accumulating on the edges. They are often applied to parts of sheet metal that have edges flanging up or formed at a place where a weld must be made to join two adjacent pieces together.

D. *Lap Joint*. This is formed when two pieces are placed atop each other while also over lapping each other for a certain distance along the edge. Considered a fillet type of a welding joint, the weld can be made on one or both sides, depending upon the welding symbol or drawing requirements. It is most often used to join two pieces together with differing levels of thickness.

E. *Tee Joint*. Tee joints, considered a fillet type of weld, form when two members intersect at 90° resulting in the edges coming together in the middle of a component or plate. It may also be formed when a tube or pipe is placed on a baseplate.

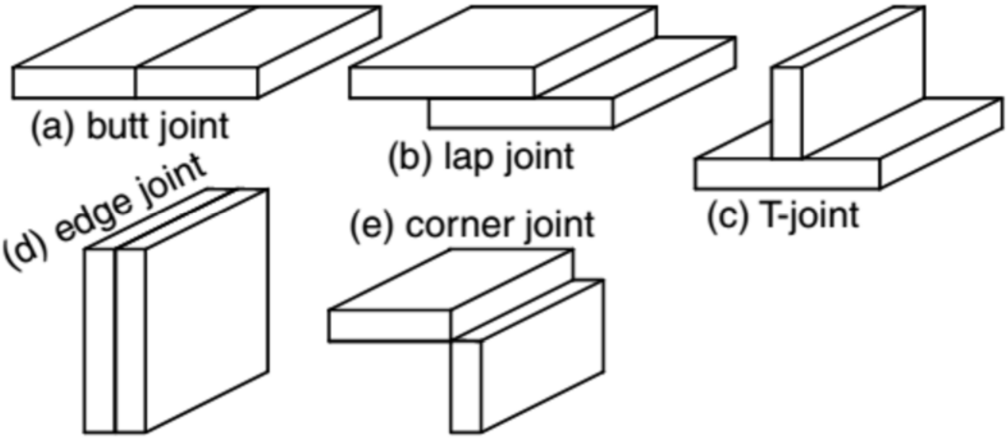

Figure 1.1: 5 basic types of welding joints [24]

Each type from the above welding joints can be made by different weld types or by a combination of them. The weld types, which are most used in shipbuilding are represented below.

A. Butt weld (***Figure 1.2***)

- *Closed butt or square groove* weld: the edges in welding plates, without any configuration, are contacted. The welding is made on one or both sides .

- *Open square butt or open square groove* weld: the two pieces have a small gap in between them during the welding process.
- *Type V*: Single-V butt welds are similar to a bevel joint, but instead of only one side having the beveled edge, both sides of the weld joint are beveled. In thick metals, and when welding can be performed from both sides of the work piece, a double-V joint is used. When welding thicker metals, a double-V joint requires less filler material because there are two narrower V-joints compared to a wider single-V joint. Also the double-V joint helps compensate for warping forces. With a single-V joint, stress tends to warp the piece in one direction when the V-joint is filled, but with a double-V-joint, there are welds on both sides of the material, having opposing stresses, straightening the material.
- *Type J*: Single-J butt welds are when one piece of the weld is in the shape of a *J* that easily accepts filler material and the other piece is square. A J-groove is formed either with special cutting machinery or by grinding the joint edge into the form of a J. Although a J-groove is more difficult and costly to prepare than a V-groove, a single J-groove on metal between a half an inch and three quarters of an inch thick provides a stronger weld that requires less filler material. Double-J butt welds have one piece that has a *J* shape from both directions and the other piece is square.
- *Type U*: Single-U butt welds are welds that have both edges of the weld surface shaped like a J, but once they come together, they form a U. Double-U joints have a U formation on both the top and bottom of the prepared joint. U-joints are the most expensive edge to prepare and weld. They are usually used on thick base metals where a V-groove would be at such an extreme angle, that it would cost too much to fill.

B. Fillet welding refers to the process of joining two pieces of metal together whether they be perpendicular or at an angle. These welds are commonly referred to as Tee joints which are two pieces of metal perpendicular to each other or Lap joints which are two pieces of metal that overlap and are welded at the edges. The weld is aesthetically triangular in shape and may have a concave, flat or convex surface depending on the welder’s technique (***Figure 1.2***).

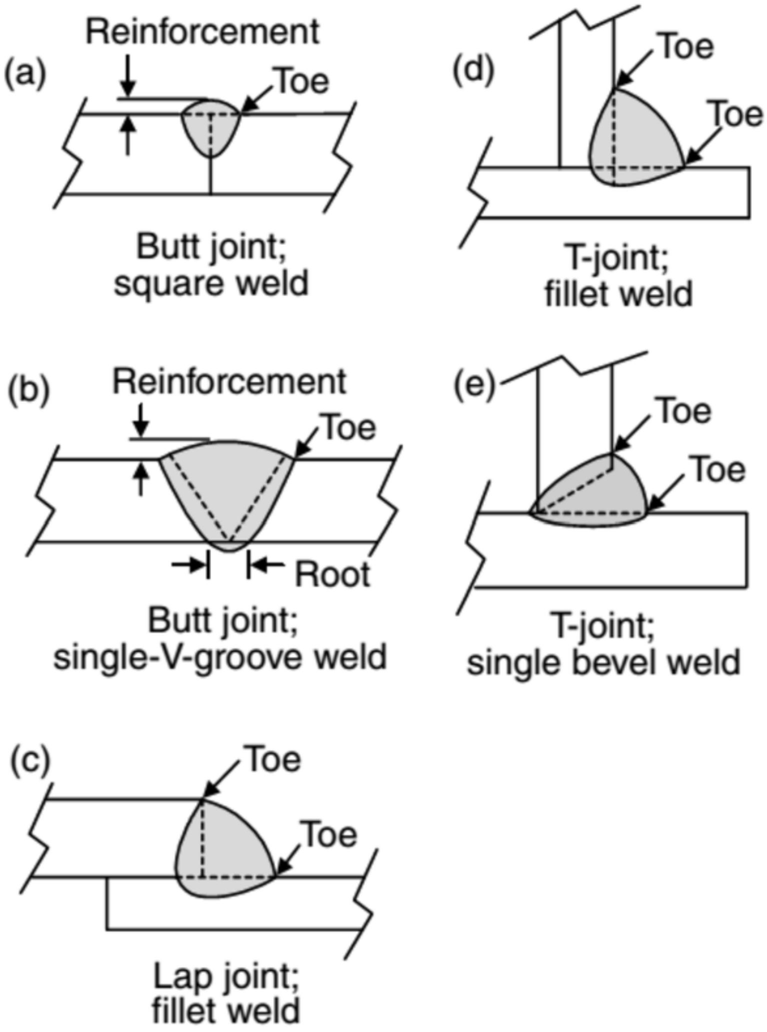

Figure 1.2: Some basic weld types [24]

1.3. Modern welding methods

The most known of modern welding methods are:

- Oxyfuel Gas Welding and Cutting.
- Shielded Metal Arc Welding (SMAW).
- Gas Tungsten Arc Welding (GTAW).
- Gas Metal Arc Welding (GMAW).
- Flux Cored Arc Welding (FCAW).
- Submerged Arc Welding (SAW).
- Vertical Automatic Welding Processes, specially electroslag and electrogas.
- Plasma Arc Welding (PAW) and Cutting (PAC).

- Laser.
- Friction Stir Welding (FSW).

In this thesis were studied 13 FCAW specimens and 13 FSW specimens. So, these methods are analyzed below.

1.3.1. Flux Cored Arc Welding – FCAW [7] [12] [17] [24] [28]

1.3.1.1. General Characteristics

Flux-cored arc welding (FCAW) was first developed in the early 1950s as an alternative to shielded metal arc welding (SMAW). The advantage of FCAW over SMAW is that the use of the stick electrodes used in SMAW is unnecessary. This helped FCAW to overcome many of the restrictions associated with SMAW.

FCAW is a semi-automatic or automatic arc welding process. FCAW requires a continuously-fed consumable tubular electrode containing a flux and a constant-voltage or, less commonly, a constant-current welding power supply. An externally supplied shielding gas is sometimes used, but often the flux itself is relied upon to generate the necessary protection from the atmosphere, producing both gaseous protection and liquid slag protecting the weld. The process is widely used in construction because of its high welding speed and portability.

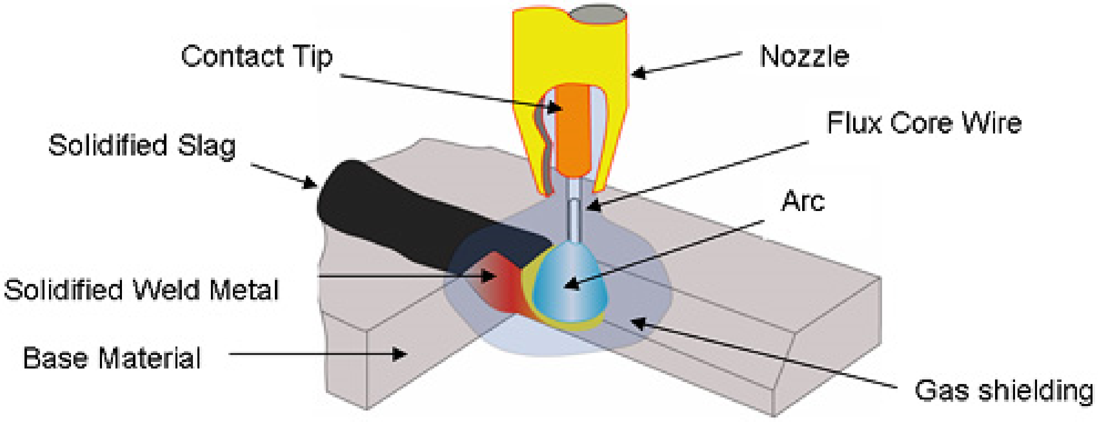

Figure 1.3: (a) overall process of FCAW [28]

One type of FCAW requires no shielding gas. This is made possible by the flux core in the tubular consumable electrode. However, this core contains more than just flux, it also contains various ingredients that when exposed to the high temperatures of welding generate a shielding gas for protecting the arc. This type of FCAW is attractive because it is portable and generally has good penetration into the base metal. Also, windy conditions need not be considered. Some disadvantages are that this process can produce excessive, noxious smoke (making it difficult to see the weld pool); As with all welding processes, the proper electrode must be chosen to obtain the required mechanical properties. Operator skill is a major factor as improper electrode manipulation machine setup can cause porosity (***Figure 1.4***).

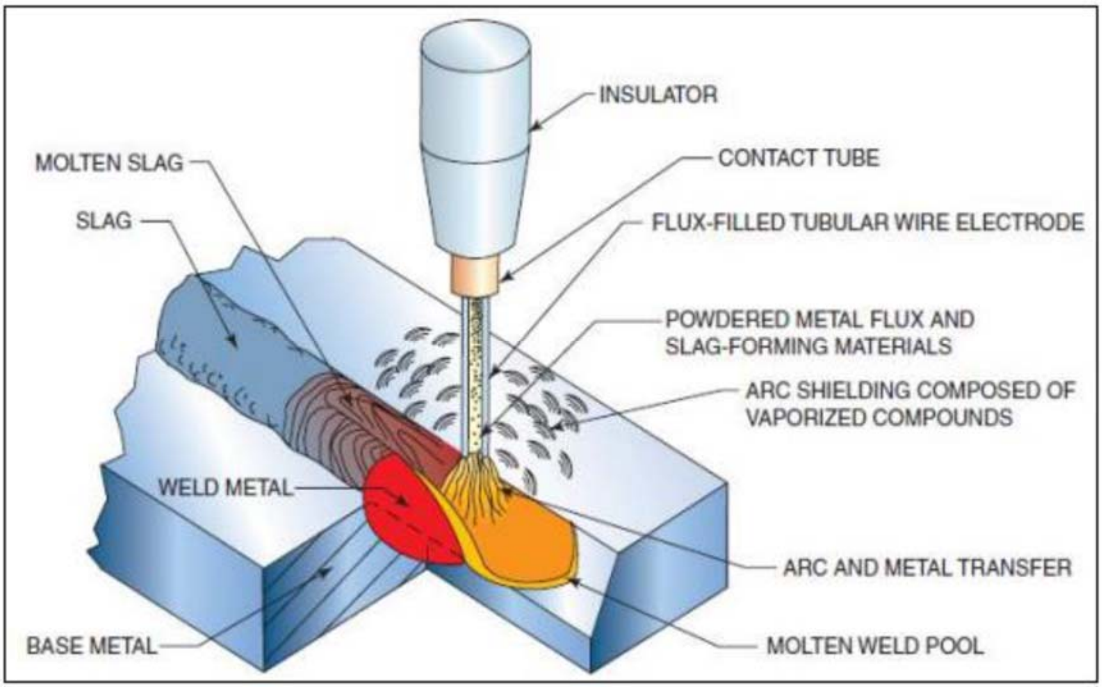

Figure 1.4: Self shielded FCAW or FCAW-S[28]

Another type of FCAW uses a shielding gas that must be supplied by an external supply. This is known informally as "dual shield" welding. This type of FCAW was developed primarily for welding structural steels. In fact, since it uses both a flux-cored electrode and an external shielding gas, one might say that it is a combination of gas metal (GMAW) and flux-cored arc welding (FCAW). This particular style of FCAW is preferable for welding thicker and out-of-position metals. The slag created by the flux is also easy to remove. The main advantages of this process is that in a closed shop environment, it generally produces welds of better and more consistent mechanical properties, with fewer weld defects than either the SMAW or GMAW processes. In practice it also allows a higher production rate, since the operator does not need to stop periodically to fetch a new electrode, as is the case in SMAW.

However, like GMAW, it cannot be used in a windy environment as the loss of the shielding gas from air flow will produce porosity in the weld (***Figure 1.5)***.

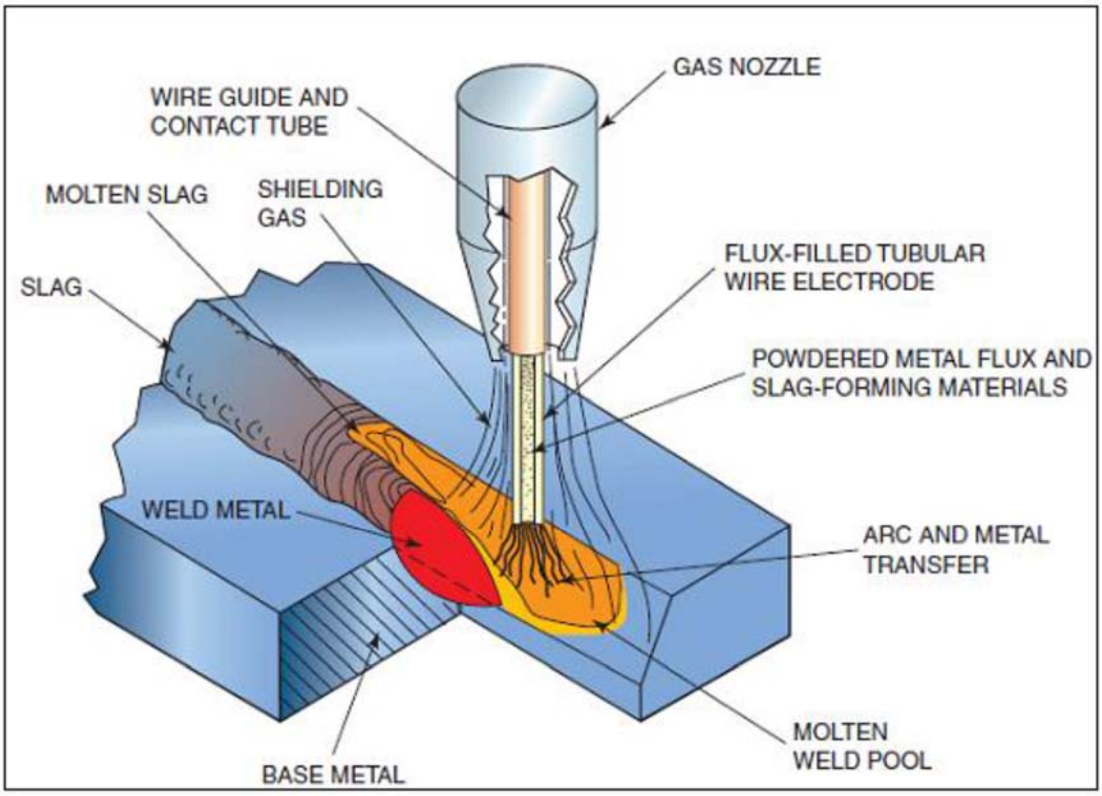

Figure 1.5: Gas shielded FCAW or FCAW-G

1.3.1.2. Process Variables- Advantages and Disadvantages

The process variables of FCAW are these:

- Wire feed speed (and current).
- Arc voltage.
- Electrode extension.
- Travel speed and angle.
- Electrode angles.
- Electrode wire type.
- Shielding gas composition (if required).
- Reverse polarity (Electrode Positive) is used for FCAW Gas-Shielded wire, Straight polarity (Electrode Negative) is used for self shielded FCAW.

The advantages of this method are represented below:

- FCAW may be an "all-position" process with the right filler metals (the consumable electrode).
- No shielding gas needed with some wires making it suitable for outdoor welding and/or windy conditions.
- Some "high-speed" (e.g., automotive) applications.
- As compared to SMAW and GTAW, there is less skill required for operators.
- Less precleaning of metal.
- Metallurgical benefits from the flux such as the weld metal being protected initially from external factors until the slag is chipped away.

Of course, all of the usual issues that occur in welding can occur in FCAW such as incomplete fusion between base metals, slag inclusion (non-metallic inclusions), and cracks in the welds. But there are a few concerns that come up with FCAW that are worth taking special note of:

- Melted Contact Tip – happens when the contact tip actually contacts the base metal, thereby fusing the two and melting the hole on the end.
- Irregular wire feed – typically a mechanical problem.
- Porosity – the gases (specifically those from the flux-core) don’t escape the welded area before the metal hardens, leaving holes in the welded metal.
- Costlier filler material/wire as compared to GMAW.
- The equipment is less mobile and costlier as compared to SMAW or GTAW.
- The amount of smoke generated can far exceed that of SMAW, GMAW, or GTAW.
- Changing filler metals requires changing an entire spool. This can be slow and difficult as compared to changing filler metal for SMAW or GTAW.
- Creates more fumes than stick welding.

1.3.2. Friction Stir Welding (FSW)

1.3.2.1. General Characteristics

Friction stir welding (FSW), invented by Thomas in December 1991, is a solid state joining process in which a constantly rotating, cylindrical-shouldered tool with a profiled probe is traversed at a constant rate along the joint between two clamped pieces of butted material. The probe is slightly shorter than the weld depth required, with the tool shoulder riding along the top of the work piece surface. The material is thermo-mechanically worked and heated high enough for plastic deformation to occur but well below its melting point. The basic concept of the process is shown in ***Figure 1.6***.

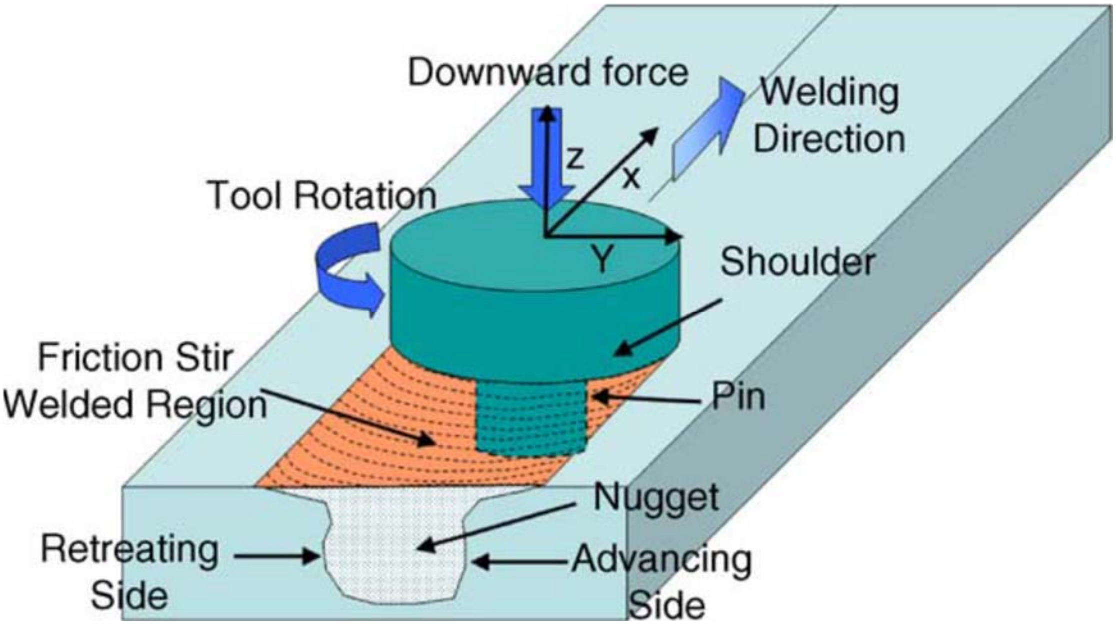

Figure 1.6: Schematic drawing of friction stir welding [20]

Frictional heat is generated between the tool and the work pieces. This heat, along with that produced by the mechanical mixing process and the adiabatic shearing within the material causes the stirred materials to soften without melting. As the tool is moved forward, a special profile on the probe forces plasticized material to the rear where clamping force assists in a forged consolidation of the weld. This process of the tool traversing along the weld line in a plasticized tubular shaft of metal results in severe solid state deformation involving dynamic recrystallization of the base material. FSW is a very complex multi-physics process incorporating mechanical and thermal processing of the material, considerable plastic deformation and high levels of flow stress; it is a process analogous to forging rather than casting which more closely resembles the conditions observed during conventional fusion welding.

FSW is currently being extensively employed in aluminum joining applications but there is significant interest by many industrial sectors in transferring the process and its advantages to steel.

1.3.2.2. Process Variables- Advantages and Disadvantages [6,7,20,21]

FSW involves complex material movement and plastic deformation. Welding parameters, tool geometry, and joint design exert significant effect on the material flow pattern and temperature distribution, thereby influencing the microstructural evolution of material. In this section, a few major factors affecting FSW/FSP process, such as tool geometry, welding parameters, joint design are addressed.

- Tool geometry: is the most influential aspect of process development. The tool geometry plays a critical role in material flow and in turn governs the traverse rate at which FSW can be conducted. An FSW tool consists of a shoulder and a pin as shown schematically in ***Figure 1.7***. The tool has two primary functions: (a) localized heating, and (b) material flow. In the initial stage of tool plunge, the heating results primarily from the friction between pin and work piece. Some additional heating results from deformation of material. The tool is plunged till the shoulder touches the work piece. The friction between the shoulder and work piece results in the biggest component of heating. From the heating aspect, the relative size of pin and shoulder is important, and the other design features are not critical. The shoulder also provides confinement for the heated volume of material. The second function of the tool is to ‘stir’ and ‘move’ the material. The uniformity of microstructure and properties as well as process loads are governed by the tool design. Generally, a concave shoulder and threaded cylindrical pins are used.

  With increasing experience and some improvement in understanding of material flow, the tool geometry has evolved significantly. Complex features have been added to alter material flow, mixing and reduce process loads.

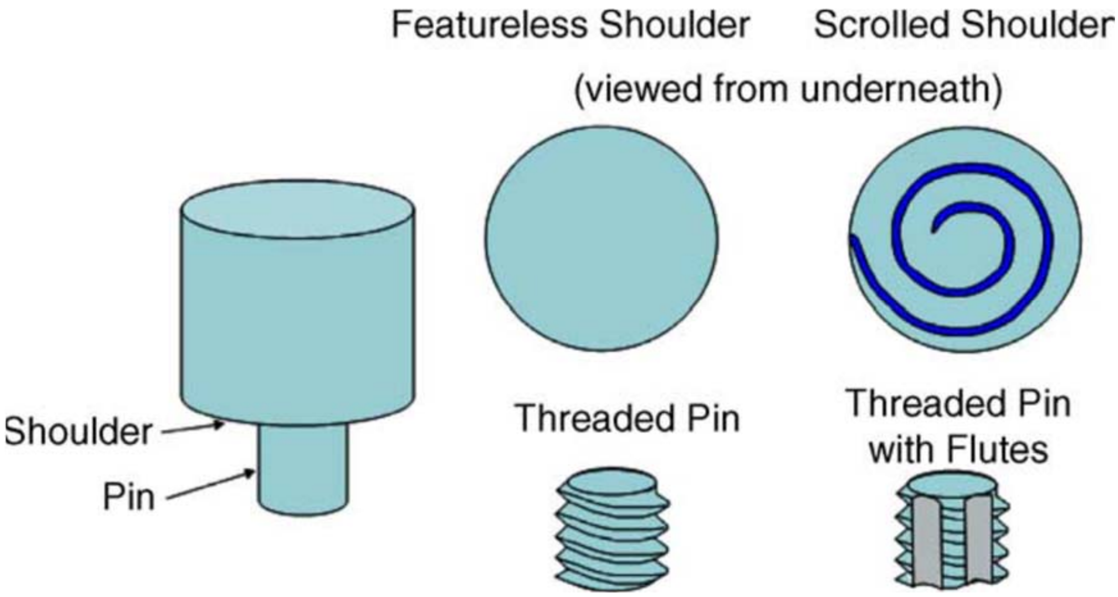

Figure 1.7: Schematic drawing of the FSW tool [20]

- Welding parameters: For FSW, two parameters are very important: tool rotation rate (v, rpm) in clockwise or counterclockwise direction and tool traverse speed (n, mm/min) along the line of joint. The rotation of tool results in stirring and mixing of material around the rotating pin and the translation of tool moves the stirred material from the front to the back of the pin and finishes welding process. Higher tool rotation rates generate higher temperature because of higher friction heating and result in more intense stirring and mixing of material as will be discussed later. However, it should be noted that frictional coupling of tool surface with work piece is going to govern the heating. So, a monotonic increase in heating with increasing tool rotation rate is not expected as the coefficient of friction at interface will change with increasing tool rotation rate. In addition to the tool rotation rate and traverse speed, another important process parameter is the angle of spindle or tool tilt with respect to the work piece surface. A suitable tilt of the spindle towards trailing direction ensures that the shoulder of the tool holds the stirred material by threaded pin and move material efficiently from the front to the back of the pin. Further, the insertion depth of pin into the work pieces (also called target depth) is important for producing sound welds with smooth tool shoulders. The insertion depth of pin is associated with the pin height. When the insertion depth is too shallow, the shoulder of tool does not contact the original work piece surface. Thus, rotating shoulder cannot move the stirred material efficiently from the front to the back of the pin, resulting in generation of welds with inner channel or surface groove. When the insertion depth is too deep, the shoulder of tool plunges into the work piece creating excessive flash. In this case, a significantly concave weld is produced, leading to local thinning of the welded plates. It should be noted that the recent development of ‘scrolled’ tool shoulder allows FSW with 08 tool tilt. Such tools are particularly preferred for curved joints.

Preheating or cooling can also be important for some specific FSW processes. For materials with high melting point such as steel and titanium or high conductivity such as copper, the heat produced by friction and stirring may be not sufficient to soften and plasticize the material around the rotating tool. Thus, it is difficult to produce continuous defect-free weld. In these cases, preheating or additional external heating source can help the material flow and increase the process window. On the other hand, materials with lower melting point such as aluminum and magnesium, cooling can be used to reduce extensive growth of recrystallized grains and dissolution of strengthening precipitates in and around the stirred zone.

- Joint design. The most convenient joint configurations for FSW are butt and lap joints. Two plates or sheets with same thickness are placed on a backing plate and clamped firmly to prevent the abutting joint faces from being forced apart. During the initial plunge of the tool, the forces are fairly large and extra care is required to ensure that plates in butt configuration do not separate. A rotating tool is plunged into the joint line and traversed along this line when the shoulder of the tool is in intimate contact with the surface of the plates, producing a weld along abutting line. On the other hand, for a simple lap joint, two lapped plates or sheets are clamped on a backing plate. A rotating tool is vertically plunged through the upper plate and into the lower plate and traversed along desired direction, joining the two plates (***Figure 1.6***). Many other configurations can be produced by combination of butt and lap joints. Apart from butt and lap joint configurations, other types of joint designs, such as fillet joints (***Figure 1.7***), are also possible as needed for some engineering applications.

  It is important to note that no special preparation is needed for FSW of butt and lap joints. Two clean metal plates can be easily joined together in the form of butt or lap joints without any major concern about the surface conditions of the plates.

The key benefits of friction stir welding are:

- Metallurgical benefits:
  - Solid phase process.
  - Low distortion of work piece.

  - Good dimensional stability and repeatability.
  - No loss of alloying elements.
  - Excellent metallurgical.
  - properties in the joint area.
  - Fine microstructure.
  - Absence of cracking.
  - Replace multiple parts joined by fasteners.

- Environmental benefits:
  - No shielding gas is required.
  - No surface's cleaning is required.
  - Elimination of grinding's wastes.
  - Eliminate solvents required for degreasing
  - Consumable materials saving, such as rugs, wire or any other gases.

- Energy benefits
  - Improved materials' use (e.g., joining different thickness) allows reduction in weight.
  - Only 2.5% of the energy needed for a laser weld.
  - Decreased fuel consumption in light weight aircraft, automotive and ship applications.

The disadvantages of the process, which have been identified are:

- Exit hole left when tool is withdrawn.
- Large down forces required with heavy-duty clamping necessary to hold the plates together.
- Less flexible than manual and arc processes (difficulties with thickness variations and non-linear welds).
- Often slower traverse rate than some fusion welding techniques, although this may be offset if fewer welding passes are required.

Chapter 2: Corrosion of Steel Welds

2.1. Steels [6,11]

2.1.1. Introduction

Steels are Fe-C alloys with carbon content ≤ 1.5% by weight. Depending on the use for which they are intended, steels are containing by case some other alloying elements, which modify their physicochemical and mechanical properties.

According to their chemical composition, steels are categorized as follows:

- Common or carbon steels.
- Alloyed or special steels.

According to their destination, they are categorized as follows:

- Steels for configuration.
- Cast steels.

According to their destination, they are categorized as follows:

- Construction steels.
- Tool steels.
- Stainless or heat resisting steels.
- Steels for electromagnetic applications.

2.1.2. Alloyed Steels

The carbon percentage in alloyed steels does not exceed practically the 1%, while the ordinary added elements are: Ni, Mn, Cr, Si, Mo (main additions) and V, W, Cu, Ti, Al, B, Pb, Nb (minor additions). Depending on the percentage of added elements, alloyed steels are divided into:

- Low-alloyed or micro alloyed steels, in which the percentage of added elements is less than 2%.
- Mild-alloyed steels, in which the percentage of added elements is between 2% and 10%.

- Strongly alloyed steels, in which the percentage of added elements is between more than 10%.

The addition of alloying elements improves the mechanical strength of the steel, the resistance to corrosion and the toughness ***(Table 2.1***). It affects the modification of Fe-C equilibrium diagram and the shifting of heat treatments curves (CCT and TTT). So, we can get various microstructures of steels (martensitic, austenitic, ferritic).

	Increase of hardenability	Improvement of mechanical properties	Corrosion resistance	Hardness	Aging inhibition	Resistance to mechanical damage
Ni	x	x	x			
Mn	(x)					
Cr	(x)		x			
Si	(x)	x	x	x		
Mo	x	x	x	x	x	x
W	x			x		x
V	x			x		x
Al	(x)					
Ti	x				x	
Co				x		

(): small increase

Table 2.1: Effect of alloying elements on the properties of steels

Carbon steel can be alloyed, singly or in combination, with chromium, nickel, copper, molybdenum, phosphorus, and vanadium in the range of a few percent or less to produce high strength low-alloy (HSLA) steels. In some circumstances, the addition of 0.3% copper to carbon steel can reduce the rate of rusting by one quarter or even by one half.

Typically, HSLA steels are low-carbon steels with up to 1.5% manganese, strengthened by small additions of elements, such as columbium, copper, vanadium or titanium and sometimes by special rolling and cooling techniques. Improved-formability HSLA steels contain additions such as zirconium, calcium, or rare-earth elements for sulfide-inclusion shape control. The higher alloy additions are usually for better mechanical properties and hardenability.

Because HSLA alloys are stronger, they can be used in thinner sections, making them particularly attractive for transportation-equipment components where weight reduction is important. The lower range of about 2% total maximum is of greater interest from the corrosion standpoint. Strengths are appreciably higher than those of plain carbon steel, but the most important attribute is a better resistance to atmospheric corrosion when freely exposed.

HSLA Steel is a type of steel alloys that provide many benefits over regular steel alloys. In general, they are much stronger and tougher than ordinary carbon based steel. It is used in cars, trucks, cranes, bridges and other structures that must be able to handle a lot of strain. HSLA Steel only contain a very small percentage of carbon, less than one percent, and only small amounts of other added metals.

2.2. Corrosion of Carbon Steel and Low-Alloyed Steel Welds [6,11,16]

2.2.1. Introduction

The corrosion behavior of carbon steel welds produced is dependent on a number of factors. Corrosion of carbon steel weldments can be due to metallurgical effects, such as preferential corrosion of the HAZ or weld metal, or it can be associated with geometrical aspects, such as stress concentration at the weld toe, or creation of crevices due to joint design. Additionally, specific environmental conditions can induce localized corrosion such as temperature, conductivity of the corrosive fluid, or thickness of the liquid corrosive film in contact with the metal. In some cases, both metallurgical and geometric factors will influence behavior, such as in Stress Corrosion Cracking (SCC).

2.2.2. Influence of Weld Microstructure

Consideration must be given to the compositional effects of the base metal and welding consumable and to the different welding processes used. The base metal experiences temperatures ranging from ambient at a distance away from the weld to the melting point at the fusion boundary during welding. Therefore, metallurgical transformations occur across the weld metal and HAZ, and these microstructures can significantly alter the intrinsic corrosion rate of the steel. Fusion welding produces a weld metal that, due to the high cooling rate, is effectively a chill casting containing a high density of lattice defects and segregation of elements. A wide range of microstructures can be developed in a weldment based on cooling rates, and these microstructures are dependent on energy input, preheat, metal thickness (heat sink effects), weld bead size, and reheating effects due to multipass welding. As a result of their different peak temperatures, chemical compositions, and weld inclusions (oxides and sulfides), weld metal microstructures are usually significantly different from those of the HAZ and base metal. Similarly, corrosion behavior can also vary, but in cases where corrosion mitigation measures are correctly applied, for example, coating or cathodic protection or inhibition, these will normally be adequate to prevent preferential corrosion of carbon steel weldments.

Another important factor to note is that for a given composition, hardness levels will be lowest for high heat inputs, such as those produced by submerged arc weldments, and will be highest for low-energy weldments (with faster cooling rates) made by, for example, the shielded metal arc, gas tungsten arc, and metal inert-gas processes. Note that in comparing the heat input, it is necessary to account for the arc efficiency
to compare processes. Depending on the welding conditions, weld metal microstructures generally, tend to be fine grained with basic flux and somewhat coarser with acid or rutile (TiO2) flux compositions.

2.2.3. Residual Stress

During welding, the base metal, HAZ, and underlying weld passes experience stresses due to thermal expansion and contraction. On solidification, high levels of residual stress, often close to the material yield stress, remain as a result of weld shrinkage. Stress-concentration effects as a result of geometrical discontinuities, such as weld reinforcement (excess weld metal) and lack of full weld penetration (dangerous because of the likelihood of crevice corrosion and the possibility of fatigue cracking), are also important because of the possibility of SCC in some environments.

2.2.4. Preferential HAZ Corrosion

A wide range of HAZ microstructures can be produced because, close to the fusion boundary, the HAZ transformation to austenite on heating will be followed on cooling by transformation to give either a ferrite-carbide microstructure or martensite, depending on material composition, peak temperature, and cooling rate. Farther from the weld, the material will be exposed to a lower peak temperature, so only partial reaustenization occurs, and those areas heated below the ferrite-to-austenite transformation temperature will not be significantly affected, other than by some carbide coarsening and tempering. Despite these variations, in the majority of applications, there is little influence on the corrosion performance, and preferential HAZ corrosion is relatively rare. Where preferential HAZ attack has been reported, it is more common in carbon and carbon-manganese steels than in higher-alloy grades.

Preferential HAZ corrosion in seawater was reported in the 1960s and attributed to the presence of low-temperature transformation products such as martensite, lower bainite, or retained austenite. Therefore, steel compositions favoring increased hardenability (e.g., increase in manganese content) may lead to increased localized corrosion, but microalloyed steels are not susceptible. Tramline corrosion is a term applied to preferential HAZ corrosion concentrated at the fusion boundaries and has been observed in acidic aqueous environments such as acid mine waters (***Figure 2.1***).

There is clearly a microstructural dependence, and studies on HAZs show corrosion to be appreciably more severe when the material composition and welding parameters are such that hardened structures are formed. It has been known for many years that hardened steel may corrode more rapidly in acid conditions than fully tempered material, apparently because local microcathodes on the hardened surface stimulate the cathodic hydrogen evolution reaction. The rate of corrosion is usually governed by the cathodic (reduction) rate when other limiting factors are not present, and therefore, it is a factor in acidic environments but less so in neutral or alkaline conditions. On this basis, it is proposed that water treatments ensuring alkaline conditions should be less likely to induce HAZ corrosion, but even at a pH near 8, hydrogen ion (H+) reduction can account for approximately 20% of the total corrosion current; pH values substantially above this level would be needed to suppress the effect completely. Furthermore, if such treatments may be useful to control preferential HAZ corrosion when it has not been anticipated, it is considered to be more reliable to avoid the problem through design. Avoidance through selection of appropriate material or welding procedure, for example, to minimize hardness, is the preferred remedial approach, because PWHT may necessitate temperatures high enough for normalizing to gain full benefit, which is usually impractical.

In some oil and gas production environments, preferential weldment corrosion may lead to enhanced HAZ attack or weld metal corrosion. In the late 1980s, studies of the problems associated with preferential weldment corrosion in sweet oil and gas production systems were undertaken (Ref 12). In some cases, the HAZ was attacked, while in other cases, the weld metal was preferentially corroded. Where enhanced HAZ corrosion was observed, the composition was more influential than the microstructure; however, hardened transformed microstructures suffered increased corrosion.

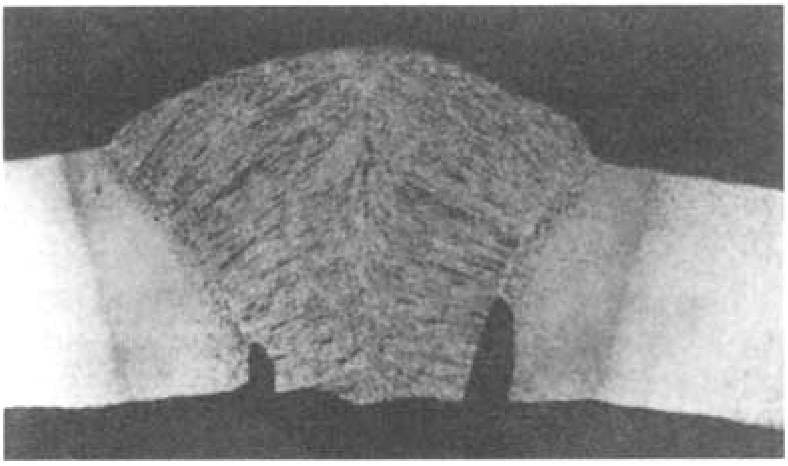

Figure 2.1: Preferential corrosion in the HAZ of a carbon steel weldment after service in an aqueous environment [11]

2.2.5. Preferential Weld Metal Corrosion

The weld metal in a carbon-manganese steel may suffer preferential corrosion, but again, if quality corrosion mitigation is in place for the main structure, such as coating or cathodic protection, this preferential attack is also normally prevented. However, there are cases where coating failure or inefficient inhibition can then lead to localized corrosion.

It is probable that similar microstructural considerations also apply to the preferential corrosion of weld metal, but in this case, the situation is further complicated by the presence of deoxidation products, their type and number depending largely on the flux system employed. Consumable type plays a major role in determining weld metal corrosion rate, and the highest rates of metal loss are normally associated with shielded metal arc electrodes using a basic coating. In seawater, for example, the corrosion rate for a weld made using a basic-flux-coated consumable may be three times as high as for weld metal from a rutile-flux-coated consumable. Fewer data are available for submerged arc weld metals, but it would appear that they are intermediate between basic and rutile flux shielded metal arc electrodes and that a corrosion rate above that of the base steel can be expected. In many cases, the underlying cause of the problem is the electrochemical potential difference between the weld metal and the adjacent parent steel, as discussed subsequently.

Preferential weld metal corrosion of carbon and low-alloy steels used for pipelines and process piping systems in carbon dioxide (CO2)-containing media has been observed increasingly in recent years. In particular, this has been on weldments made by the manual metal arc (MMA) process using electrodes containing nickel or nickel plus copper. One comprehensive study examined the link between preferential weld metal corrosion and electrode composition. Corrosion tests have shown these:

- Greatest resistance to preferential weld metal corrosion was obtained for autogenous root deposits or for welds deposited using consumables without significant alloying additions (matching filler metals).
- The addition of 1% Ni was detrimental, as was 1% Si.
- The addition of 0.5% Mo or 0.6 to 0.7% Cr to the weld metal had no consistent beneficial effect with respect to preferential weld metal corrosion.
- Preferential weld metal corrosion also increased with increasing hardness, increasing grain size, an increasing level of aligned second phase, and a decreasing level of microstructure refinement of the root by subsequent passes.

2.3. Types of Steel Welds Corrosion [6,11]

Weldes can suffer all the classic types of corrosion, however are particularly sensitive to corrosion types, which are affected by changes in the microstructure and the composition. Such types of corrosion such as galvanic corrosion, pitting, *stress corrosion cracking,* intergranular corrosion, *wet hydrogen sulfide cracking*, must be taken seriously into account when there are welds.

Galvanic Corrosion: Some of the earliest problems of weld metal corrosion related to ships in arctic waters, where ice abraded the paint to expose bare steel and damaged the anodes, thus rendering the cathodic protection system ineffective. In these cases, it was observed that enhanced corrosion of the weld metal was due to electrochemical potential differences between the weld metal and the base metal, such that the weld metal is anodic in the galvanic couple. Further detailed studies were undertaken in the late 1980s to assess more modern steels and welding consumables in arctic waters off Canada. Both HAZ and weld metal attack were observed, and the general conclusions were that for steels between 235 and 515 MPa (34 and 75 ksi) minimum yield strength with high manganese content (1.4%) in the parent steel, resulted in enhanced preferential HAZ attack, but this could be reduced via increased heat input during welding. Generally, the rate of weld metal attack was dependent on the nickel and copper contents of the welding consumable and was less influenced by parent steel composition, although a steel with copper, nickel, and chromium additions led to a more noble parent steel, hence accelerating weld metal attack. It was noted that parent steel with low silicon content led to increased weld metal corrosion, supporting the earlier findings that silicon <0.2% can be detrimental, but the opposite was observed for silicon in the weld metal.

Stress Corrosion Cracking-SCC: Stress-corrosion cracking is a term used to describe service failures in engineering materials that occur by slow, Environmentally Assisted Cracking (EAC) propagation. The observed crack propagation is the result of the combined and synergistic interaction of mechanical stress and corrosion reactions.

Stress corrosion is caused by the presence of external or internal stresses in addition to the corrosive medium. The following condition produced these factors in this case:

- After welding, the circumferential seam was heat treated by local stress relieving that does not ensure complete removal of residual stresses.
- The seam had been repaired twice without being stress relieved adding considerable residual stresses to the weld and nearby region.
- The solution passing through the vessel contained CO_2-CO-H_2O, KHCO, and Cl– ions, which induce SCC in carbon steels at temperatures greater than 100 °C.

To tackle the problem, after the welding process, heat treatments can be made. The aim of the treatments is to reallocate the focused loads at various points and to reduce the size of the residual tensile stresses that contribute to the initiation of cracks.

Wet Hydrogen Sulfide Cracking: Corrosion of carbon and low-alloy steels by aqueous hydrogen sulfide (H2S) solutions or sour waters can result in one or more types of EAC. Two of the more prevalent forms of EAC affecting weldment corrosion are hydrogen induced cracking (HIC) and sulfide stress cracking (SSC). It should be noted that there are actually two forms of HIC. The first form is cracking due to exposure to wet H2S as described in this section. A second form—weld-related HIC—is described later in this chapter.

*Hydrogen-induced cracking***,** which has been observed in both high- and low-strength steels even under nonstressed conditions, occurs primarily in the low-strength steels that are exposed to a hydrogen-containing environment. Because of its rapid cooling and solidification, weld metal forms a structure of dendrites and has oxide inclusions dispersed in the form of fine globules. It has been confirmed that weld metals, even when used without a filler metal of special chemistry, do not develop HIC up to a maximum hardness of 280 HV.

Sulfide stress cracking is the failure of steel caused by the simultaneous action of stress and hydrogen absorbed from corrosion by aqueous H2S. Susceptibility to SSC is a function of a number of variables, two of the more important are strength or hardness of the steel and the level of tensile stresses. Sulfide stress cracking is normally associated with high-strength steels and alloys—yield strength greater than 550 MPa (80 ksi)—and with high-hardness (>22 HRC) structures in weld HAZs. Non-post weld heat treated weldments are particularly problematic, because they often contain both high HAZ hardness and high residual tensile stresses that can initiate SSC and promote crack propagation. Resistance to SSC is usually improved through the use of lowercarbon- equivalent plate steels and quenchedand- tempered wrought steels.

Causes and preventive measures of cracks appearance due to Hydrogen Induced Cold Cracking on base metal and on welded metal are shown at the figures below (***Figures 2.2, 2.3***):

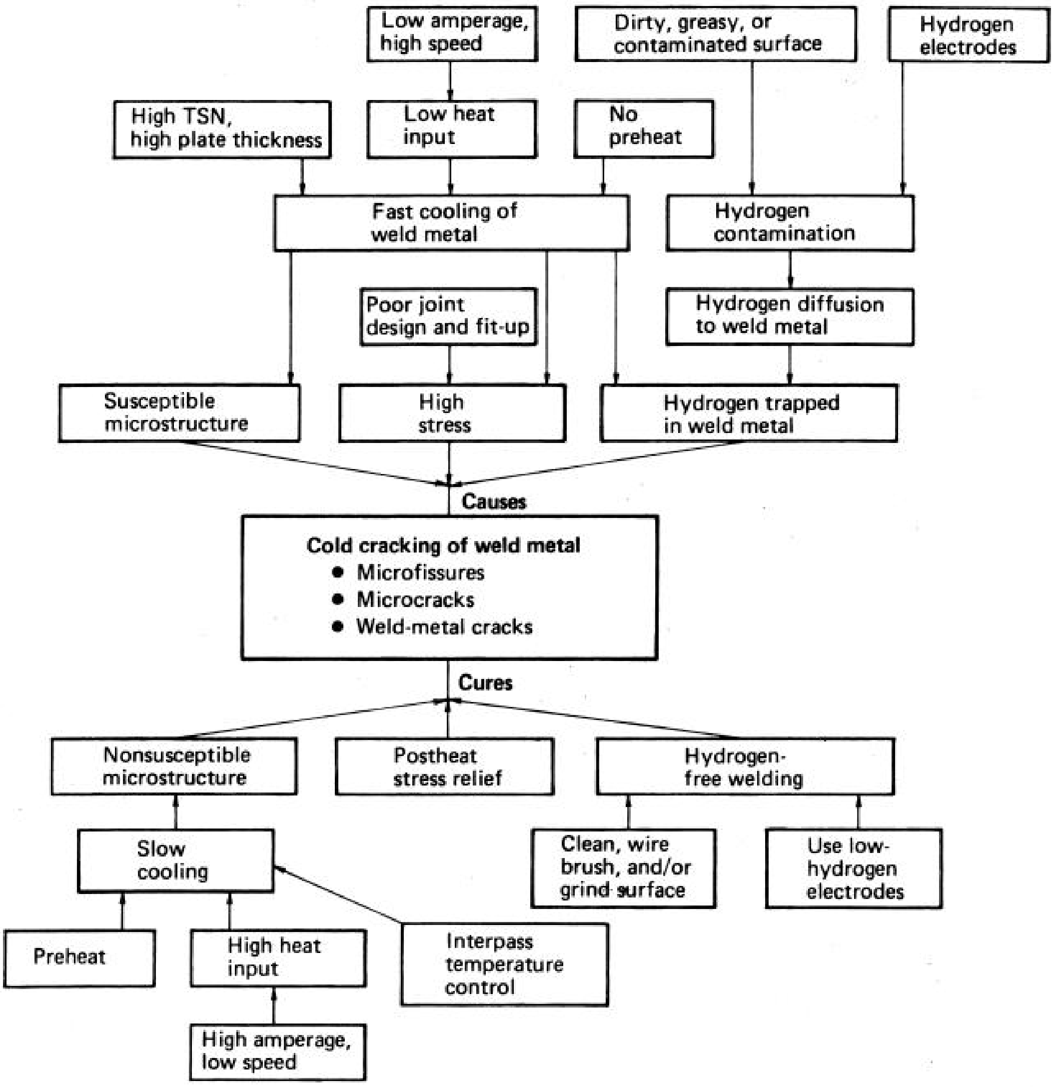

Figure 2.2: Causes and preventive measures of cracks appearance due to Hydrogen Induced Cold Cracking on welded metal [11]

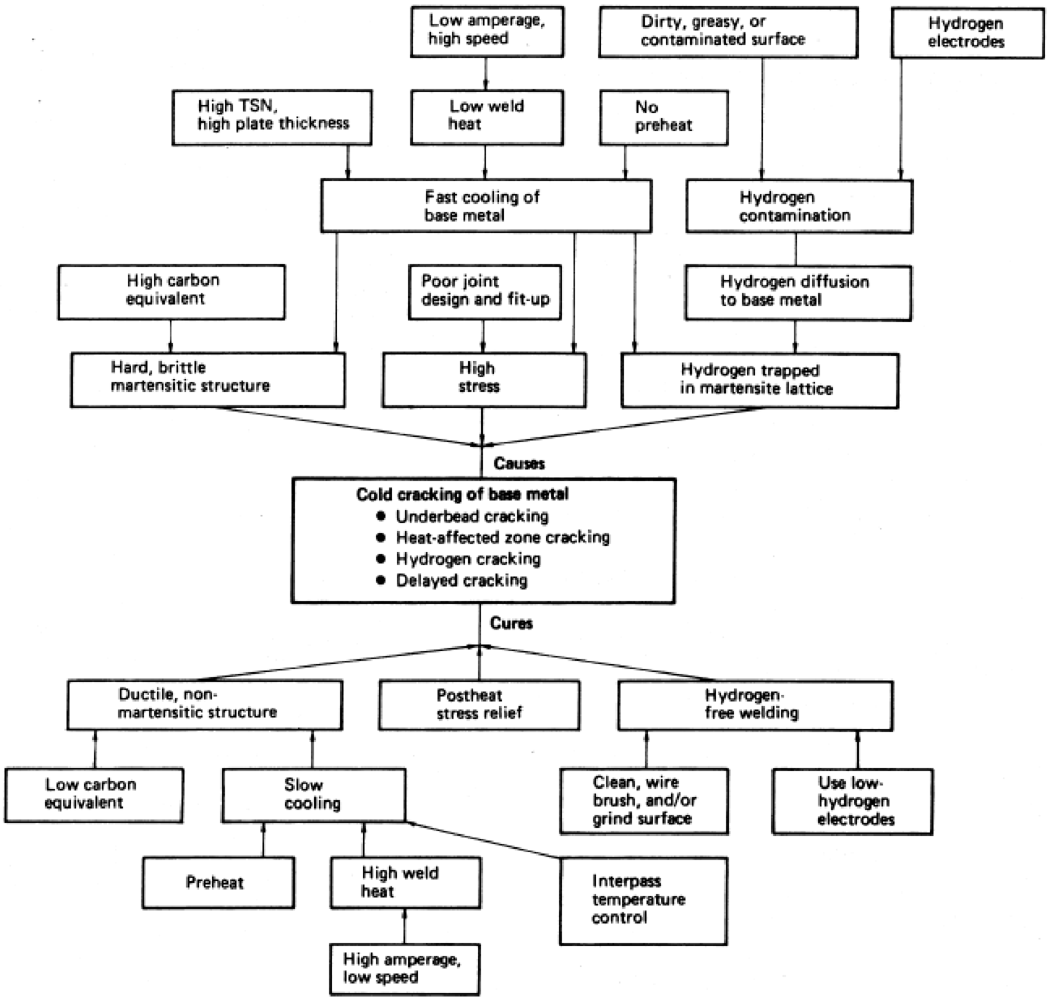

Figure 2.3: Causes and preventive measures of cracks appearance due to Hydrogen Induced Cold Cracking on base metal [11]

2.4. Corrosion of Steel Welds by FSW Method [20,23]

Welding is one of the most important processes for fabricating metallic structures. The study of welding metallurgy has long been addressed by academia, industry, and organizations such as the American Welding Society and the Edison Welding Institute in the United States and The Welding Institute in the United Kingdom. Similarly, extensive research has been carried out on the fundamentals of corrosion and the various types of corrosion that can render a structure useless. The welding process can influence both microstructural and corrosion behavior.

The zones of FSW exhibit different microstructural characteristics such as grain size and dislocation density, residual stress and texture, and precipitate size and distribution. Therefore, it is expected that the various microstructural zones will exhibit different corrosion susceptibility.

Studies have shown that the pits in FSW samples formed in the HAZ, whereas in GTAW for example samples the pits formed in the large dendritic region just inside the fusion zone. Second, FSW welds showed a pitting resistance higher than those of base metal. Frankel and Xia pointed out that although the differences in pitting potential were not very large, the trend of higher pitting potential for FSW samples was observed consistently.

Studies indicated that the hottest regions within the HAZ were the most susceptible to intergranular corrosion. Microstructural examinations on the hottest regions of the HAZ revealed significant Cu depletion at grain boundaries. Based on the experimental observations, Lumsden et al. attributed the mechanism of intergranular corrosion to a Cu depletion model linking intergranular corrosion with pitting corrosion. This is consistent with previous studies that the pitting potential decreases with a decrease of Cu.

Chapter 3: Experimental procedure

3.1. Introduction

One of the main purposes of this thesis is to study the corrosion behavior of high strength low alloy (HSLA) steel S690 parent metal and similar arc welding S690 (FCAW). The corrosion of high strength shipbuilding steel AH36 friction stir welding is also studied in this thesis. The mechanism of corrosion was investigated, firstly, by the method of mass loss and then by electrochemical experiments.

3.2. Materials - AH36 Steel (High Strength) and S690 Steel (High Strength Low Alloy) [6,11,12,22]

The materials, which are studied are the AH36 (High Strength Steel) and S690 Steel (High Strength Low Alloy). Their characteristics are analyzed below.

3.2.1. AH36 Steel (High Strength)

The first material that was studied, is the high strength steel AH36, which belongs to High Strength Steels. Welded specimens with dimensions: 70 x 100 x 12 mm^3 were studied (***Figure 3.1***).

The name and the classification as shipbuilding steel type AH36 follows the A131M standard of ASTM and comes from Lloyd's Register of Shipping Steels. By this name is known worldwide, but also found under another name, according to the classification of some countries (e.g. USA K11852, A36 Russia, 1.0565 Germany, etc.). The chemical composition of this steel is given in ***Table 3.1***.

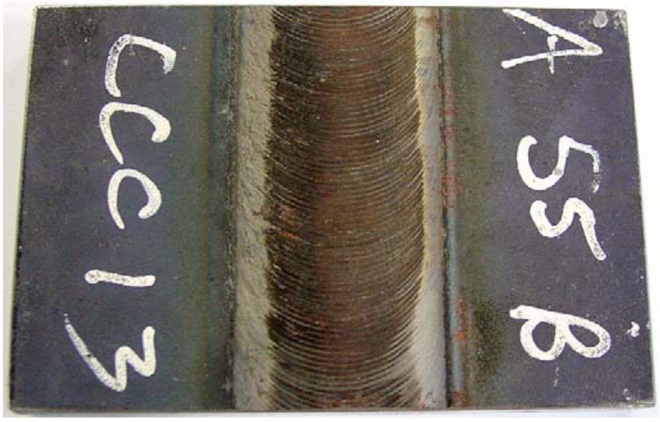

Figure 3.1: Specimen of Friction Stir Welding

Chemical Composition	% max. unless specified in range
C	0.18
Mn	0.90–1.60
Si	0.10–0.50
P	0.035
S	0.035
Al (acid Soluble) min	0.015
Nb	0.02–0.05
V	0.05–0.10
Ti	0.02
Cu	0.35
Cr	0.20
Ni	0.40
Mo	0.08

Table 3.1: Chemical composition (%w/w) of AH36 steel alloying elements

The yield strength of the steel is 36 Kp/mm^2 or 353.2 MPa. According to IACS (International Association of Classification Societies) the mechanical properties of the shipbuilding steels are shown in the following table (***Table 3.2)***. The hardness of this steel is approximately 180 Vickers.

Grade	**Yield Strength ReH (N / mm^2) min**	**Tensile Strength Rm (N / mm^2)**
A B D E	235	400 - 520
AH32 DH32 EH32 FH32	315	440 - 570
AH36 DH36 EH36 FH36	355	490 - 630
AH40 DH40 EH40 FH40	390	510 - 660

Table 3.2: Mechanical properties of shipbuilding steels

For thicknesses up to 12.5 mm (0.50 in) the steel is semi-quiescent, i.e. fully deoxidized. Also, for plate thickness up to 12.5 mm, the minimum Mn content may reach 0.70% w/w, whereas for such thickness and for semi-quiescent steels 10% w/w, the minimum Si content may be less than 10% w/w.

When one of Al Nb and V is used, must be respected the minimum level which is set for each, and when they are combined, the total sum of the content of Al, Nb and V must not exceed the 0,12% w/w. The hardness of AH36 steel is approximately 180 Vickers. The value of the equivalent carbon content (ECC) of high strength steel AH36 is given by the following equation:

$$C_{eq}=C+\frac{Mn}{6}+\frac{Cr+Mo+V}{5}+\frac{Ni+Cu}{15}(\%)$$

The value of the equivalent carbon content (Ceq) for AH36 varies from 0.38 % to 0.57 %, since there is great variation in the content of Mn. Usually the value of Ceq for AH36 trade does not exceed the 0.40 %. The CCT diagram of AH36 steel is shown in ***Figure 3.2***.

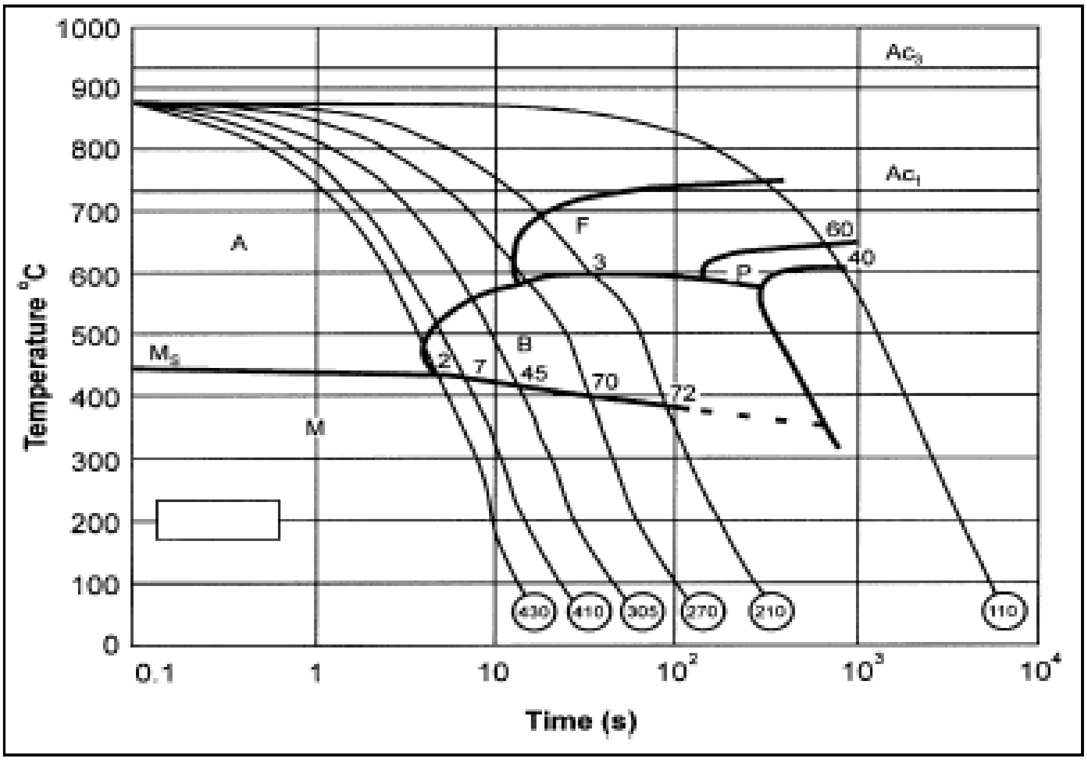

Figure 3.2: The CCT diagram of AH36 steel

3.2.1.1. The use of AH36 Steel

The hull and the tanks of the ships are usually made of common shipbuilding steel. However, in recent years the use of high strength steels expands. The result of this use is thinner and lower weight sheets, compared to carbon steels.

Compared with common mild steel, the high-strength steel AH36 has (***Table 3.3***):

- Lower carbon content.
- Greater hardness.
- Higher strength.
- The same resistance to fatigue.
- As good weldability.
- The similar resistance to corrosion.

	% max. unless specified in range	
Chemical Composition	**Common steel**	**High strength steel**
C	0.18- 0.21	0.18
Mn	min 0.60	0.90–1.60
Si	0.35 – 0.50	0.10–0.50
P	0.035	0.035
S	0.035	0.035
Al (acid Soluble) min	-	0.015
Nb	-	0.02–0.05
V	-	0.05–0.10
Ti	-	0.02
Cu	-	0.35
Cr	-	0.20
Ni	-	0.40
Mo	-	0.08

Table 3.3: Alloying elements in common steel and in high-strength steel

In high-strength steel there are greater stresses (due to reduced thickness) so, the abrasion of protective coatings is made faster, thus increasing the likelihood of crack initiation and therefore the risk of corrosion of mechanical stress. Finally, due to the reduced thickness, when high strength steel is used, the corrosion margin is reduced too. Therefore, the constructions by HS steels may be more susceptible to corrosion, than the constructions by common mild steel.

3.2.2. S690 Steel (High Strength Low Alloy)

The second material that was studied is the S690 steel, which belongs to HSLA (High Strength Low Alloy) steels. The first S means structural. 13 welded specimens with dimensions: 70 x 110 x 12 mm^3 and 25 parent metal specimens with dimensions: 70 x 100 x 12 mm^3 were studied (***Figure 3.3.***).

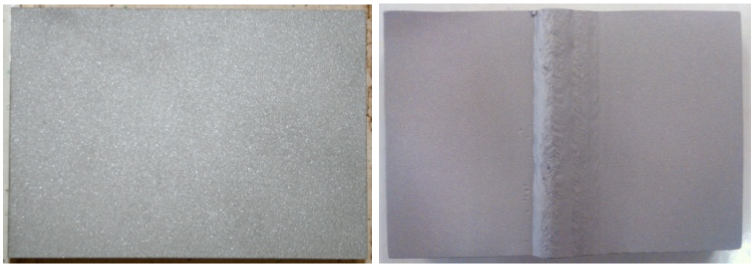

Figure 3.3: Left: Specimen of Parent Metal S690, Right: Specimen of FCAW S690

High strength low alloy (HSLA) steels have been developed since the 1960s originally for large diameter oil and gas pipelines. The requirement was high strength as compared to mild carbon steel, combined with improved toughness and good weldability. These steels are containing less than 3.5% of alloying elements e.g. 2.25% Cr 1% Mo.

The S690 steel is a high strength steel with minimum yield stresses of 690 MPa for thicknesses below 16 mm. The S690 steel grade should have a tensile strength between 770 and 940 MPa, also for thicknesses below 16 mm. The hardness of this steel is approximately 280 Vickers. The CCT diagram of S690 steel is shown in ***Figure 3.4*** and its chemical composition is shown at the table below (***Table 3.4***):

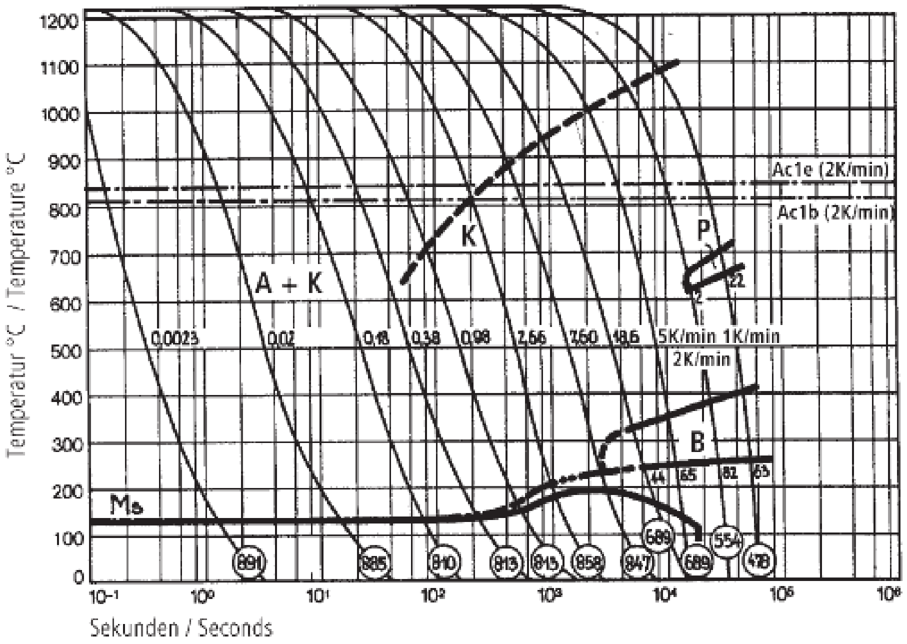

Figure 3.4: The CCT diagram of S690 steel

Chemical Composition	% max. unless specified in range
C	0.20 max
Mn	1.70 max
Si	0.80 max
P	0.025 max
S	0.015 max
Al	0.015 min
Nb	0.06 max
V	0.12 max
Ti	0.05 max
Cu	0,50 max
Cr	1.50 max
Ni	2.0 max
Mo	0.70 max
B	0.005 max
Zr	0.15 max

Table 3.4: Chemical composition (%w/w) of S690 steel alloying elements

3.2.2.1. The use of S690 steel

The steel was chosen due to improved fatigue crack initiation and crack arrest properties, compared to conventional marine steels. The fatigue crack growth property is reported to be superior to that of conventional steel because it possesses an optimum ferrite and bainite dual phase microstructure and the dual phase boundaries reduce fatigue crack growth.

The 690 grade steels are increasingly used in lifting appliance construction due to the weight reductions and/or extra lifting capacity. The ship building industry is looking to higher strength steels in order to develop lighter and more fuel efficient ships with S690 type grades being the highest strength of the series of grades under consideration.

HSLA is:

- Much stronger and tougher than ordinary carbon steels.
- Ductile.
- Highly formable.
- Weldable.
- Highly resistant to atmospheric corrosion - which is important since the structure may be in place for a long time.

HSLA can be found in these applications until now:

- Bridges.
- Suspension Components.
- Building Structures.
- Vehicles/Transportation
- Tubular Components.
- Heavy Equipment.
- Rails.
- Off-shore/Platforms.

Higher steel grades (e.g. S690) are usually applied in steel members and/or in bridge regions with very high static stresses in order to reduce the cross sectional dimensions and plate thicknesses of these members (***Figure 3.5***). As a result, the overall steel self-weight of the bridge will be reduced leading to a more economical design in comparison to the case where the same (equivalent) design is made out of mild steels only.

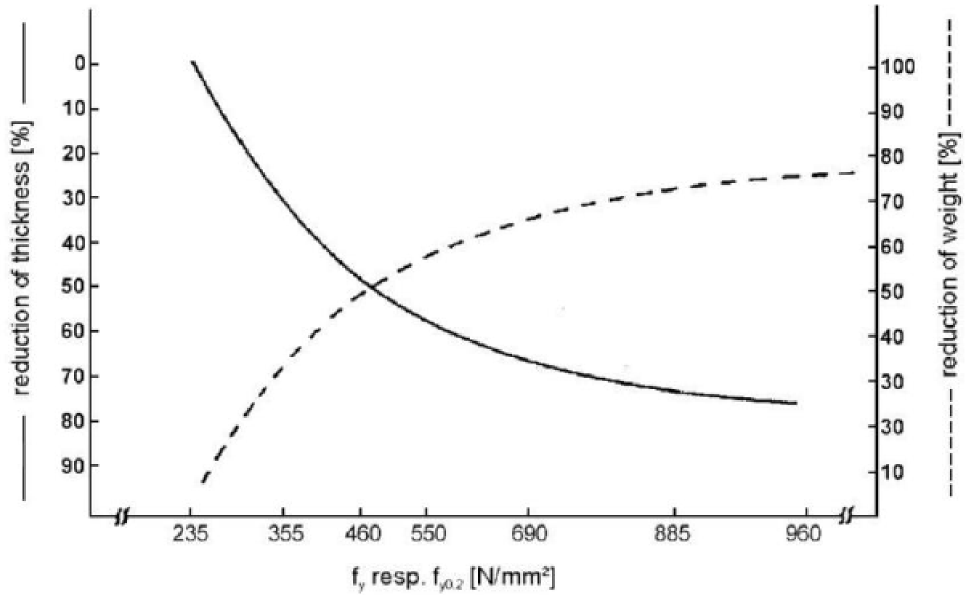

Figure 3.5: Weight and thickness reduction with increasing steel strength

3.3. Welds

From the 48 specimens, the 24 were welded. The welds were similar AH36 Flux-Core Arc Welding (FCAW) and similar S690 Friction Stir Welding (FSW). The processes were fully automated and took place at the technological center AIMEN (the FCAW specimens) and at TWI (the FSW specimens) respectively.

3.3.1. Flux-Core Arc Welding (FCAW)

The design of the joint of the pieces and the weld pass are shown in the following figure (***Figure 3.6***):

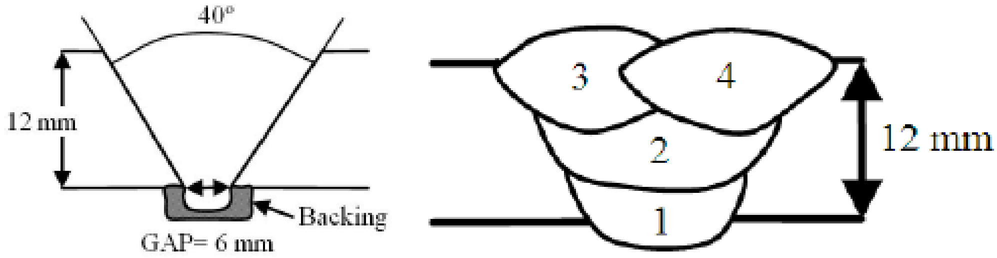

Figure 3.6: Form of the joint and the number of passes at the welding process

In FCAW method was used the electrode under the tradename FLUXOFIL M42, which has a diameter of 1.2 mm. ***Table 3.5*** shows the parameters of the welds. The shielding gas used was Ar15%CO_2 and the gas flow was 15 l/min.

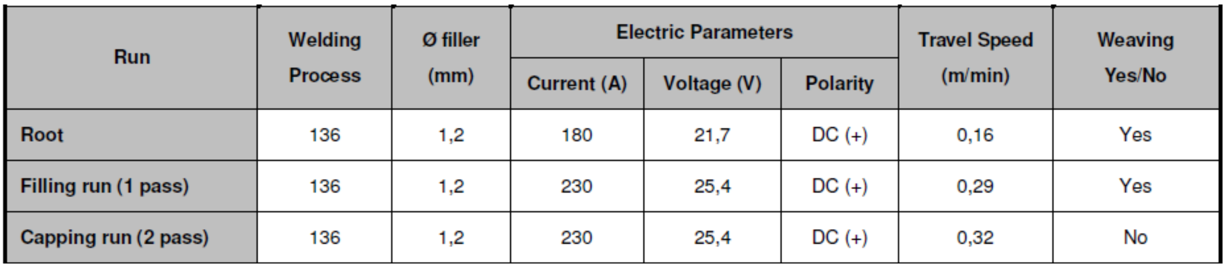

Run	Welding Process	Ø filler (mm)	Electric Parameters			Travel Speed (m/min)	Weaving Yes/No
			Current (A)	Voltage (V)	Polarity		
Root	136	1,2	180	21,7	DC (+)	0,16	Yes
Filling run (1 pass)	136	1,2	230	25,4	DC (+)	0,29	Yes
Capping run (2 pass)	136	1,2	230	25,4	DC (+)	0,32	No

Table 3.5: Weld parameters of FCAW

3.3.2. Friction Stir Welding (FSW)

The welds were made at a tool traverse rate of 100mm/min and a nominal tool rotation speed of 150 rpm (***Figure 3.7***). Small adjustments were made to the tool rotation speed during the course of the weld when required to control the process stability. Argon at a flow rate of 14 l/min was used as a shielding gas to protect the FSW tool from oxidation during the welding process. Though it was not the primary purpose of the shielding gas, it also assisted in protecting the surface of the welded plate from oxidation.

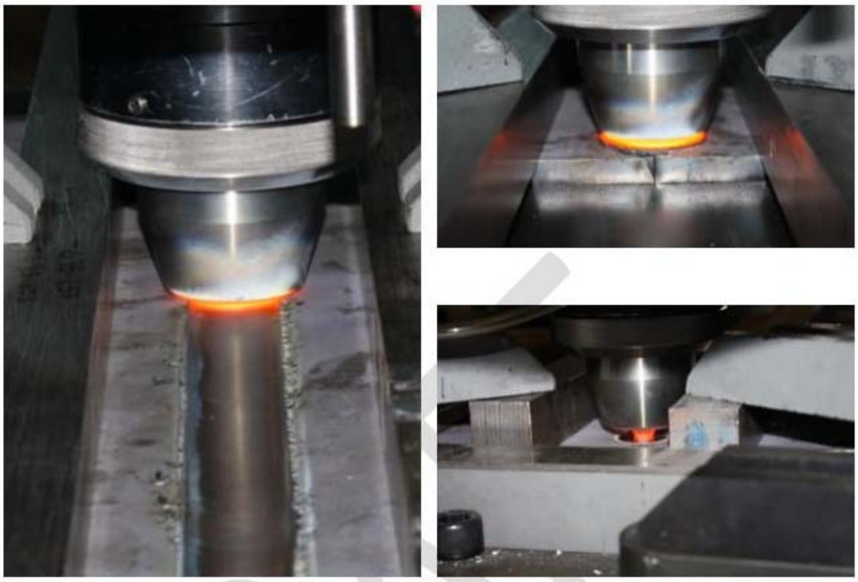

Figure 3.7: A weld being made in AH36 steel at a tool traverse rate of 100mm/min. This weld was witnessed by a surveyor from Lloyd's Register.

Left: The tool and weld surface at the midpoint of the weld.
Upper right: Tool being plunged into the steel at the weld start.
Lower right: Tool being extracted from the steel at weld end.

3.4. Microstructure – Micro-hardness [6]

For a better understanding of each metal and its welds, it was considered appropriate the study of their microstructure and micro - hardness. The procedure, which was followed, is presented below.

3.4.1. Chemical etching and Optical microscopy

The Optical Microscopy is a very important method of observation and interpretation of the microstructure of materials, which is the main subject of the metallography. To be each specimen suitable for observation under optical microscope, needs to follow some preparation, the stages of which are:

- *Cutting* of specimens with discotom in the laboratory (***Figure*** **3.7**) and then they are immersed in two-component epoxy resin (resin and hardener), as shown in ***Figure 3.8***.

Figure 3.7: Discotom of the Lab of Naval Technology

Figure 3.8: Specimens immersed with an epoxy resin

- *Surface* abrasion for observation. It is done either by mechanical or electrochemical methods and seeks to eliminate the geometric irregularities of the surface. In this thesis mechanical abrasion (***Figure 3.9***) was used. In this way, for the abrasion, abrasive papers are used with hard grain SiC or Al_2O_3, where the scrubbing action eliminates surface irregularities having a size greater than the average size of the abrasive grains. Using paper with ever smaller grains, the abrasion becomes more detailed. In this thesis were used the following papers: grit 80, 120, 220, 500, 800, 1200, 2000, 4000. The final stage of this process called polishing includes polishing in special velvets using sol or ointment Al_2O_3 (alumina grain up to 0.1 μm), spray with fine grain diamond, etc. At this procedure for the specimens was used ointment Al_2O_3 grained alumina 1 and 0.1 μm.
- *Etching* of the metal surface with the aim to reveal details of the microstructure of the material, since the final surface can yield relatively few information. It is the most used technique revealing the features of the structure and is based on 'selective' corrosion of grain boundaries. Also, the atoms which belong to different crystal lattices (i.e. in different phases), are dissolved, at different rates, thus creating contrast in the surface, the appearance and the display of the microstructural characteristics when they are observed by the optical microscope. The etching was done by immersing the smooth metal surface in an appropriate chemical reagent.

Figure 3.9: Machine of abrasion / polishing Struers LaboPol-5 the Lab. of Naval Technology

In the case of the shipbuilding steel AH36 and S690 steel was selected the reagent Neital (a solution of pure ethanol with 2 % v/v HNO_3) which gives very good results by immersing the specimens in a small container with the reagent for different duration for each specimen.

Following the treatment, which was mentioned above, the specimens were ready for observation under the optical microscope of Laboratory of Naval Technology, which is type Leica DMILM.

The main parts of the microscope are (***Figure 3.10)***:

- The light source.
- The lenses that guide the light beam.
- The diaphragm.
- The magnifiers.
- The semi - reflective mirror.
- The objective lens.
- The table on which the specimen is placed for observation and allows its movement by suitable devices suitable.
- The eyepiece.

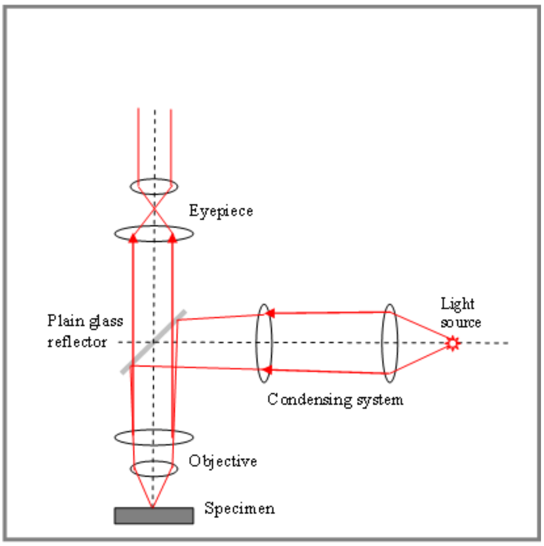

Figure 3.10: Schematic representation of the optical microscope function [31]

Besides the above, the optical microscope is equipped with a suitable device for the camera fastening. It also has two types of magnifiers: the objective and eyepieces. The first is the most important, because they collect the reflected light from the metal piece and compose the image. They are usually screwed and placed in a rotating base, which receives four lenses with different magnification for each. The eyepieces have a fixed magnification. They are at the point from which the user observes the microscope and magnify the generated image from the objective lens, giving the final result. The total magnification of the observed image is the product of the growth of these two lenses.

3.5. Accelerated Testing - Salt Spray Champ [1,3,4,5,19,26]

3.5.1. Accelerated corrosion Testing in a Salt Spray Chamber

It is known that the corrosion of metallic materials with or without corrosion protection is influenced by many environmental factors. It is impossible, therefore, to design accelerated laboratory corrosion tests in such a way that all environmental factors influencing the resistance to corrosion are taken into account. Laboratory tests are designed to simulate the effects of the most important factors enhancing the corrosion of metallic materials.

In order to conduct corrosion tests on steel protective coatings, first proposed test in a neutral salt spray solution under standard ASTM B117. Many improvements and updates have been made in recent years in salt spray testing and in the chambers which are used.

The most generally accepted methods of salt spray tests are described accurately in these the standards:

- ASTM B117 “Standard method of salt spray (FOG) testing”.
- BS368 “Standard test method for copper-accelerated acetic - salt spray (FOG) testing”.
- ASTM G 85 “Standard practice for modified salt spray (FOG) testing”.

There are corrosion tests in which high humidity is applied, where distilled water is used as a component of corrosion and which do not include salt as a corrosion element (ASTM D1735, ASTM D2247, ASTM G 60).

The salt spray tests are divided into two categories:

- Tests on "static" conditions.
- Tests on "cyclic" conditions.

In static tests the conditions and the atmosphere remain constant throughout the test: temperature, cloud density, pH of the electrolytic solution. Tests may last 24 hours a day, 7 days a week throughout the exposure time. Then the specimens are removed from the chamber for study and analysis.

During cyclic tests, the specimens are subjected to repeated and specified time steps with different atmosphere, until the preset exposure time or number of cycles will be completed. A complete set of steps constitutes one cycle.

These steps include:

- Different temperatures.
- Varying levels of relative humidity RH (20-100%).
- Various corrosive components (contaminants, electrolytes).

3.5.1.1. Tests on "static" conditions

The ASTM B117 standard describes static conditions in salt spray tests. The process of this standard defines constant exposure to salt spray 5% at 35°C. In the last 70 years the standard ASTM B 117 has really improved. However, despite the improvements it is common that the salt spray test results in static conditions are not satisfying the corrosion phenomena, which are observed in the operating environment.

3.5.1.2. Tests on "cyclic" conditions

The cyclic corrosion tests are considered more realistic. During cyclic tests, corrosion of materials is caused in a way that responds better to the reality, than the conventional routes of exposure. Since the operating environment of a material usually includes wet and dry conditions, the aim is the laboratory tests to simulate natural cyclic conditions. In cyclic corrosion, test specimens are exposed to a different environment in repeated cycle. Simple cycles consist of repeated salt spray conditions and dry. Most modern automatic methods include cycles of many steps, such as humidity or condensation with salt spray and dry.

For cyclic corrosion tests in salt spray chamber, various standards have developed that determine accurately the conditions of the experiment:

- ASTM G85 “Standard practice for modified salt spray (FOG) testing”
- ISO 14993 (2001) “Corrosion of metals and alloys – Accelerated testing involving cyclic exposure to salt mist, “dry” and “wet” conditions”.

In this thesis, for the study of the corrosion of AH36 (HS) and S69O (HSLA), the ISO 14993 (2001) standard was adopted.

The conditions of salt spray - drying - humidity in which the specimens were exposed, are described in detail below:

- *Salt spray* (or Fog), (***Figure 3.11***): During the operation of the salt spray, the chamber operates as a conventional salt spray device:
    - The compressed air is liquefied by passing the bubble tower on its way to the spray nozzle.
    - Corrosive solution is pumped from the inner reservoir to the spray nozzle, where it is mixed with compressed air.
    - Spray nozzle vaporizes the solution and the air, creating fog corrosion.
    - Chamber heaters maintain the default temperature of the chamber.

- *Dry* (***Figure 3.12***): During the dry, the air compressor leads the room air in an air chamber heater. This creates low humidity conditions inside the chamber. The temperature of the chamber is controlled by chamber and air heaters.

- *Humidity* (***Figure 3.13***): During this operation, the chamber is maintained at the 100% of relative humidity, giving water vapors to the chamber.

Below is a schematic representation of a complete cycle in the salt spray chamber:

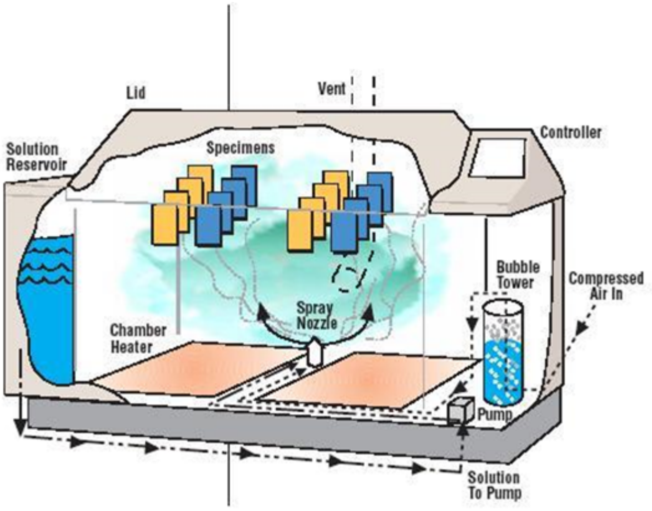

Figure 3.11: Salt mist conditions in the climatic chamber

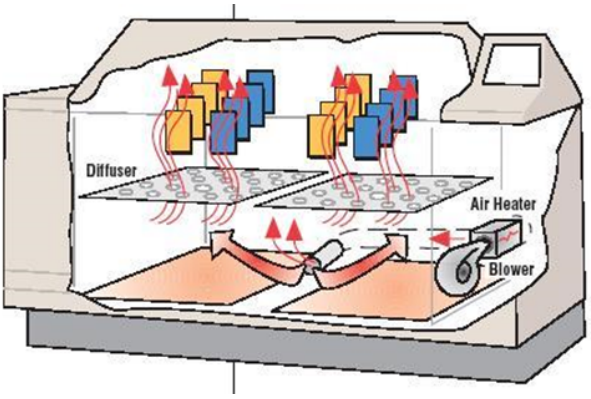

Figure 3.12: Dry conditions in the climatic chamber

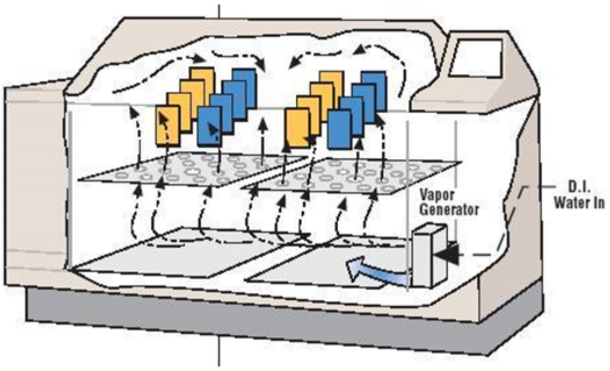

Figure 3.13: Humidity conditions in the climatic chamber

3.5.2. Technical Characteristics of Salt Spray Chamber

The salt spray chamber used in this thesis is the Q FOG CCT1100 (***Figure 3.14***), the company Q Panel and has the following characteristics:

- Nominal size: 1100 l
- Capacity with liquid: 1103 l
- Capacity without liquid: 857 l

Figure 3.14: Salt Spray Chamber (Q FOG CCT 1100)

The salt spray chamber has a quite large capacity so as to ensure uniform conditions of temperature distribution conditions, humidity and spray distribution. The upper parts of the chamber are designed so that drops, which are formed from the salt spray on its surfaces, not to fall in the samples.

The main parts of the chamber are:

- Salt Solution Reservoir: The 120 l ensure enough solution, so that take part salt spray for 5 consecutive days.
- Bubbles Tower: The purpose of this provision is the saturation of air with humidity before it reaches the nozzle spray. Therefore, air saturation is achieved at temperatures higher than those of the chamber. The temperature and saturation controlled automatically.
- Vapor Generator: During the humidity operation, the chamber is maintained at 100% of relative humidity by vapors, which are produced by heating water in Vapor Generator.
- Purge Blower and Air Heater: The Purge Blower is activated during the dry operation to bring the room air in the chamber.
- Heating plates: The two plates are located at the bottom of the chamber. They are used during salt spray. They are, also, activated, whenever is its necessary, during the operation of dry to maintain the programmed temperature of the chamber.

A schematic representation of Salt Spray Chamber is shown in ***Figure 3.15***:

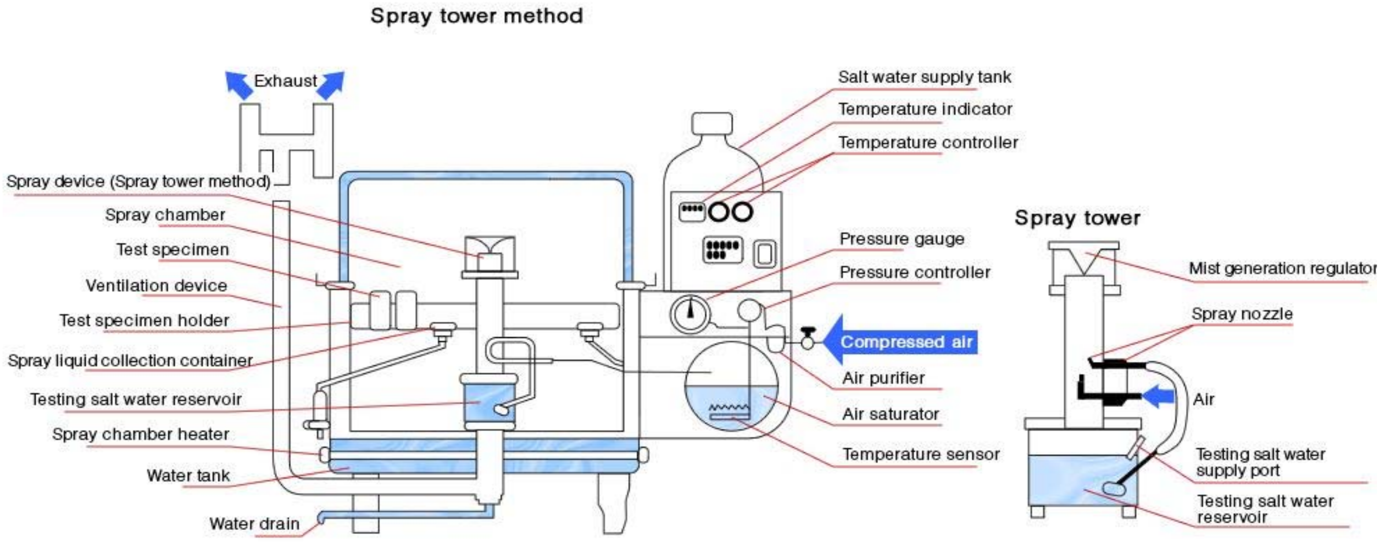

Figure 3.15: Schematic representation of Salt Spray Chamber [26]

3.5.3. Standard test by ISO 14993: 2001[3]

The accelerated corrosion test method is designed to simulate and enhase the environmental influence on a metallic material of exposure to an outdoor climate where exposure to salt-contaminated conditions occurs and may promote corrosion The test method involves cyclic exposure of test specimens to a mist of salt solution, to dry conditions and to periods with high humidity. The method provides valuable information on the relative performance of materials exposed to slat-contaminated environments similar to those used in the test.

The equipment, which is required, is the climatic chamber described above. Also, before placing the specimens in the chamber, the specimens have to:

- Sandblasted in the sandblasting machine, to remove the shop primer of the steel from the side of the specimen, that will be exposed to corrosive conditions.
- Cleaned with distilled water, then with ethanol, followed by drying with hot air.
- Weighed in balance (3 decimal).

The solution, which is used, is a solution of NaCl 5%, according to ISO 14993. According to this standard, each cycle includes three steps: salt spray, dry, humidity. The total time of each cycle is 8 hours, and it us consisted of three steps: 2 hours salt spray, 4 hours dry conditions, 2 hours humidity.

To study the behavior of the (AH36 and S690) in this thesis, 48 samples were placed in a climatic chamber.

Specifically, the test conditions are summarized in the ***Table 3.6*** below:

1	**Salt mist conditions** (1) Temperature (2) Salt solution	**2 hours** 35 ^{0}C±2 ^{0}C 50 g/l ± 5 g/l NaCl solution
2	**Dry conditions** (The air is purged under dry conditions) (1) Temperature (2) Relative humidity	**4 hours** 60 ^{0}C±2 ^{0}C <30%RH
3	**Wet conditions (Humid)** (Condensation on the test specimens shall not occur under wet conditions) (1) Temperature (2) Relative humidity	**2 hours** 50 ^{0}C±2 ^{0}C >90%RH
4	**Period and content of a single exposure cycle**	Total period 8 hours as follows: Salt mist spray 2 hours Dry conditions 4 hours Wet conditions 4 hours (These times include the time for reaching the specified temperature for each condition)
5	**Time to reach the specified condition** (i.e. period taken for temperature and humidity to reach the specified values once the test condition has begun)	Mist to Dry < 30 min Dry to wet < 15 min Wet to mist < 30 min (Mist conditions are attained almost instantaneously once this conditions begins
6	**Angle** at which test specimens are supported	20^{o} to the vertical

Table 3.6: Exposure conditions of specimens in a climatic chamber

For the support of some specimens in the chamber, formed plastic tubes made of polypropylene random (PPR) were used.

Moreover, according to the standard, the back side and edges of all specimens were covered with special adhesive tape, so that only the one side of specimens will be exposed in corrosion conditions.

3.5.4. Preparation and marking of specimens

In the chamber were placed three groups of specimens. The first group consisted of 24 specimens of parent metal S690 (100x70 mm^2). The second group consisted of 12 specimens (similar AH36 friction stir welding, 100x70 mm^2) and the third group consisted of 12 specimens (similar S690 FCAW, 110x70 mm^2). Overall, 48 specimens were examined. All groups remained together in the chamber from January 14, until February 13, 2015. The characterization of the specimens, without etched name, was made as follows: ijk.

i: number of plate: I, II, ..., X

j: the line in which the specimen belongs (A, B, C, where B always represents the welding specimens and A, C represent the base metal specimen's sides right and left of the weld).

k: The column in which the specimen belongs.

For exposure to salt mist chamber, the test, initially, sandblasted of the sandblasting machine of the Lab of Laboratory of Naval Technology (***Figure 3.16***). Then, they cleaned with distilled water, ethanol and were dried with hot air directly. Finally, according to the ISO 14993 standard, the specimens were exposed in the chamber to the corrosive environment only from the one side. Therefore, the other side of each specimen was covered by protective tape (3M 471 Vinyl Tape).

Figure 3.16: Sandblasting machine of the Laboratory of Naval Technology

3.5.5. Specimens in the salt spray chamber (Planned Interval Test) [1]

The specimens were placed in the chamber according to the standard ASTM G31-72 (1999), known as Planned Interval Test (***Figure 3.17***).

An example of the proposed procedure Planned Interval Test is the following:

- *Specimen* A_1: Removed from the chamber at the time corresponding to a unit time.
- *Specimen* A_t: Removed from the chamber at time t.
- *Specimen* A_{t+1}: Removed the chamber at time t + 1 (where 1 = unit time).
- *Specimen B*: Replaces At specimen when it is removed from the chamber at time t and comes out with the specimen At + 1, i.e. it remains in the chamber time equal to unit time.

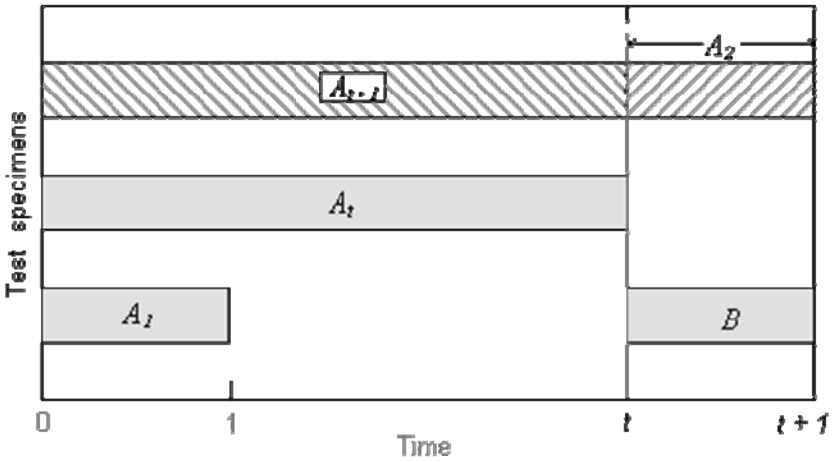

Figure 3.17: A schematic representation of Planned Interval Test

In this way, by comparing the corrosion rate of the A and B, which are remained in the chamber the same time but at different periods, we can extract conclusions about the conditions that exist in the chamber and if they are change (corrosive environment).

Comparing the corrosion rate of B with the difference of the corrosion rate between At and At + 1, we can see how behaves the metal as it is corroded. We can see if the corrosion rate is constant, reduced, or increased by the of corrosion progress. In this thesis, the unit time = 5 days. The specimen's installation in the chamber during the experiment was made in such a way that there are at least two specimens that will be remained the same time in the chamber, but at different periods.

3.5.6. Mass Loss Calculation - Corrosion Rate

For removal of corrosion products and corrosion rate calculation the procedure, that was chosen, is described in ISO 8407 (1991) Standard.

After the removal from the chamber, the specimens are cleaned with distilled water and then it is soaked in a solution of 1000 ml, for as long as necessary, composed of:

- 500ml HCl (37%)
- 3.5 g (hexamethyletetramine)
- distilled water to complement 1000ml

After the exposure to the solution, the specimens are cleaned with distilled water and ethanol and dried with hot air. Then, the specimens are weighed again and by the mass loss, the corrosion rate is calculated using this equation:

$$\text{Corrosion\_rate} = \frac{K \times W}{A \times T \times D}$$

Where:

K: a constant (depending on the unit of measurement of corrosion rate (***Table 3.7***),

W: mass loss in g, to nearest 1 mg,

A: area in cm^2 to the nearest 0,01 cm^2,

T: time of exposure in hours to the nearest 0.01h,

D: density in g/cm^3

Corrosion Rate Units Desired	**Constant (K) in Corrosion Rate Equation**
mils per year (mpy)	$3,45x10^6$
inches per year (ipy)	$3,45x10^3$
inches per month (ipm)	$2,87x10^2$
millimetres per year (mm/y)	$8,76x10^4$
micrometres per year (μm/y)	$8,76x10^7$
picometres per second (pm/s)	$2,78x10^6$
grams per square metre per hour (g/m^2h)	$1,00x10^4xD^A$
milligrams per square 50 decimetre per day (mdd)	$2,40x10^6xD^A$
micrograms per square metre per second ($\mu g/m^2s$)	$2,78x10^6xD^A$

Table 3.7: Constant K values for different units measure of the corrosion rate

3.6. Structured white light 3D scanning

Three-dimensional sensing technologies can be classified as passive or active. Passive systems, such as classical photogrammetry, use image intensities to obtain object coordinates. High accuracy can be achieved with passive systems when surfaces are covered with artificial or natural texture and have well defined edges, but in the absence of these features successful recording is troublesome. Active systems use laser beams or structured light to measure size and shapes of objects.

The measurement principle of structured light scanners is based on detecting the deformation of a pattern of light projected onto the surface of an object. The pattern may be one dimensional (line) or two dimensional. A camera placed slightly offset from the projector records the shape of the line at an angle (***Figure 3.18***) and the distance to every point on the line is computed using a technique similar to triangulation.

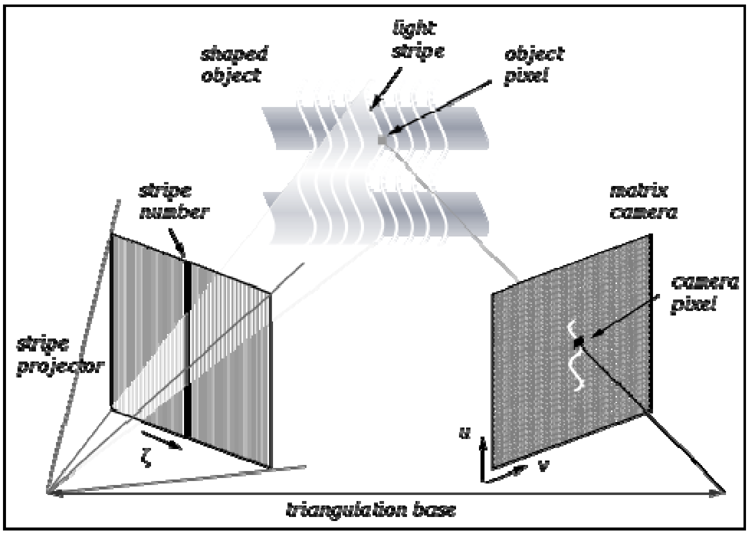

Figure 3.18: Schematic representation of operation principle of scanning method using structured light [32]

When a line pattern is used, the line is swept over the surface one strip at a time. Faster and more versatile is the projection of many stripes at once, allowing the simultaneous acquisition of multiple samples. A camera records the deformation of the pattern and a complex algorithm calculates the distance to points on the lines (***Figure 3.18, right***). The displacement of the stripes allows for an exact retrieval of the 3D coordinates of any surface detail. The advantage of structured light 3D scanners is speed, as they scan multiple points or the entire field of view at once. Some systems even enable the scanning of moving objects in real time. As with all optical methods, reflective or transparent surfaces cause difficulties. Light is either reflected away from the camera or right into its optics, as curved surfaces always have areas parallel to the image plane of the camera. The resulting reflective holes are difficult to handle. (Semi) transparent surfaces have to be coated with a thin, opaque lacquer.

In the present thesis the mapping of the corroded surface was attempted, for three kinds of specimens, in total six (6) specimens, after the removal of the corrosion products:

- Parent Metal S690 specimens: IA1, regular, 15 days and IB1, regular, 30 days
- Similar AH36 Friction Stir Welded specimens: S40009, regular, 15 days and S40008, regular, 30 days
- Similar S690 FCA Welded specimens: specimen IA2, regular, 15 days and IB2, regular, 30 days

The specimens, firstly, were scanned after sandblasting, so to compare the surfaces before and after the corrosion process in the salt spray chamber. The scanner scanned each specimen separately, creating a grid every time. Afterwards both grids were compared using two different software, the CloudCompare and Rapidform XOR3.

The scanner, employed is IScan M300 (***Figure 3.19***) of Imetric company. ***Figure 3.20*** shows an example of the pattern that displays the scanner of the Laboratory.

The scanning of the specimens were performed by Dimitris Tyris, Dipl. Mechanical Engineeer, in Manufacturing Laboratory of Materials (Machine & Mechanical Factory), School of Mechanical Engineering of NTUA, under the supervision of Prof. G. Vosniakos.

Figure 3.19: Immetric.Swiss 3D scanner systems [33]

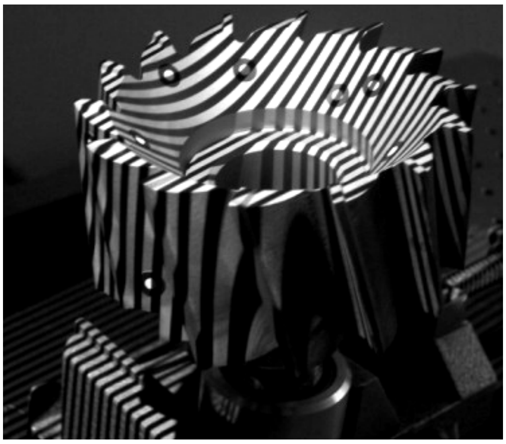

Figure 3.20: Pattern lines, which are projected by a structured white light scanner [33]

3.7. Electrochemical measurements for the corrosion study [6,35]

Almost all phenomena of corrosion can be interpreted in terms of electrochemical reactions. Therefore, an electrochemical method can be used to study these phenomena. Potential/Current measurements under carefully controlled conditions can provide information about the corrosion rate, coatings, passivation, the trend to pitting corrosion appearance and other important data.

The potentiodynamic anodic polarization is characteristic of a metal specimen from the relationship potential - current. The potential of the specimen is slowly increased in the positive direction and therefore the piece acts as an anode, corrodes or forms oxide layer. These measurements are used to determine the characteristics of corrosion of metallic specimens in an aqueous environment. An integrated diagram of potential - current can be obtained in a few hours or a few minutes.

These methods are applied to study phenomena such as passivation, and the action of corrosion inhibitors or oxidizing agents. In this way, different metals and alloys can be compared and also can to study the compatibility of material - environment.

3.7.1. Potentiodynamic polarization measurements

When a metal specimen is immersed in a corrosive, environment its surface occurs simultaneously oxidation and reduction. Usually, the specimen is oxidized (corroded) and the solvent is reduced. Under acidic conditions hydrogen ions H^+ are reduced. To study the corrosion behavior of the specimen should operate both as an anode and as a cathode and on its surface should be developed anodic and cathodic currents. The phenomena of corrosion are usually the result of anodic currents.

When a specimen is in contact with a corrosive liquid and the specimens are not conductively connected with any device, the specimen has potential (relative to the reference electrode) called corrosion potential Ecorr. A specimen in E_{corr} potential has both anodic and cathodic currents on the surface. However, these currents are exactly equal in values so that no measured net current. The specimen, then, is in equilibrium with the environment, even if it appears that it is corroded.

It is important to note that when a specimen is in a potential E_{corr} both polarities of current are present. If the specimen is polarized light more positive than E_{corr}, then anodic prevail against cathodic current. Since the potential of the specimen increases towards more positive values, cathode current is inconsiderable relative to the anodic.

Experimentally, the characteristics of polarization are measured by charting the applied potential to the resulting current. Because the value of the current may have values in different orders of magnitude, the graph is semi-logarithmic. This graph is called potentiodynamic polarization graph (because, of course, the graph is semi-log, is not displayed in the graph the polarization). Rates of potential more negative than E_{corr} cause the increase in cathodic current and positive values cause increase in anodic current.

3.7.1.1. Polarization resistance or linear polarization

The electrochemical techniques of polarization resistance are used to measure the absolute values of the corrosion rate, usually in mpy (mill-inches per year). The polarization resistance measurements can be made very quickly. The literature refers a square relationship between corrosion rate values by the method of the polarization resistance and conventional mass-loss methods. The polarization resistance also called linear polarization.

The measurement of the polarization resistance (linear polarization) is performed by scanning the potential of the specimen in a range which is very close to the corrosion potential. The value of the potential is typically ± 25mV of the potential E_{corr}. The resulting current is plotted on the graph relative to the potential (***Figure 3.21 & 3.22***). The corrosion current i_{corr} associated with the slope of the graph using the following equation:

$$\Delta E/\Delta i = \frac{\beta_\alpha \cdot \beta_c}{2{,}3 \cdot I_{corr} \cdot (\beta_a + \beta_c)}$$

Where:

ΔE/Δi : the slope of the graph of Polarization Resistance, where ΔE is in volts and Δi is in μA. The slope has units of resistance (polarization resistance),

β_α, β_c : Tafel constant, respectively (defined by Tafel diagram). The constants have units of volts / decade of current

I_{corr}: corrosion current, μA.

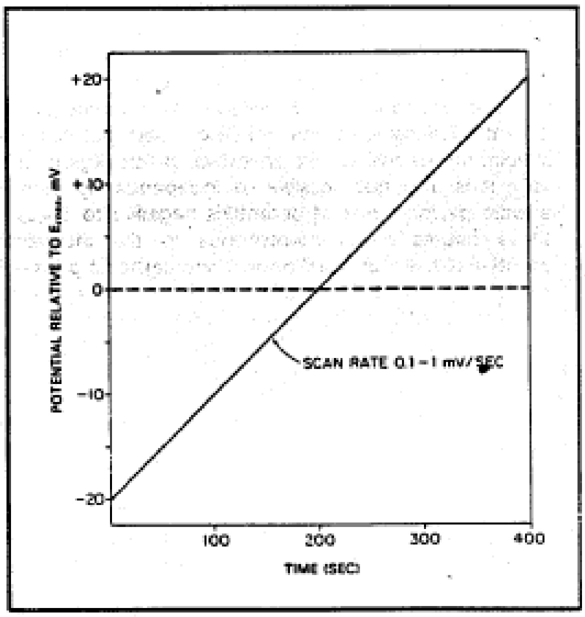

Figure 3.21: Potential scan of the polarization resistance by reference to time

From the previous equation, I_{corr} can be calculated:

$$I_{corr} = \frac{\beta_\alpha \cdot \beta_c}{2{,}3 \cdot (\beta_a + \beta_c)} \frac{\Delta i}{\Delta E}$$

According to the references $\frac{\Delta i}{\Delta E}$ can be replaced by R_p.

The corrosion current is directly related to the corrosion rate by the following equation:

$$\text{Corrosion Rate (mpy)} = \frac{0.13 * I_{corr} * (E.W.)}{d}$$

Where:

E.W.: equivalent weight of the corroded specimen, (g)

d: density of corrode specimen, (g / cm^3)

I_{corr}: the density of corrosion current, (μA / cm^2)

The method of the polarization resistance is an extremely fast process to determine the corrosion rate. For a scan rate of 0.1 mV / sec, the range of 50 mV requires less than 10 minutes of scanning.

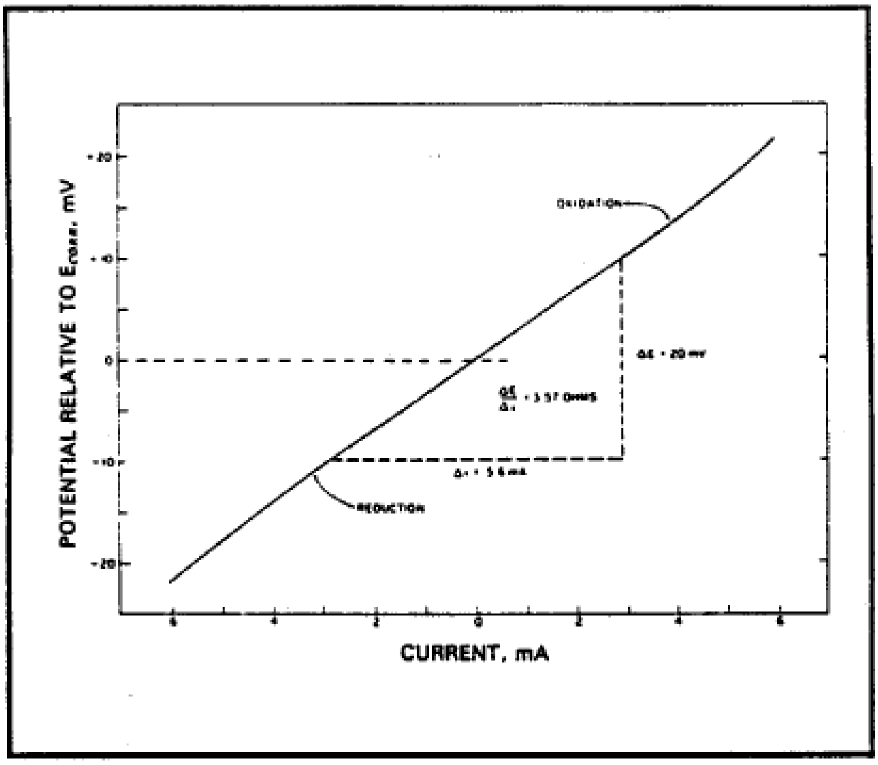

Figure 3.22: Potential scan of the polarization resistance by reference to current

Since the applied potential is not removed too far from the corrosion potential (E_{corr}), the surface of the specimen is not altered, as a result the specimen may be used in other measurements.

For more accurate results, it has to be defined the Tafel constants, βα and βc independently from the Tafel diagram. For fast measurements Tafel constants are generally considered to 0.1 V / decade. According to Pourbaix, if Tafel constants are considered 0.1 V / decade, the calculated corrosion rate should be multiplied by a factor of 2.2. In many cases, the actual values of the Tafel constants can be found in references for similar chemical systems.

3.7.1.2. Tafel method - graphs

The Tafel graphs are applied to measure the corrosion rate. A Tafel graph is generated by the polarization of a metal specimen for about 300 mV anodic (positive) and cathodic (negative) relative to the corrosion potential (E_{corr}), as shown in ***Figure 3.23***. The resulting current is shown in logarithmic graph, as shown in ***Figure 3.25***.

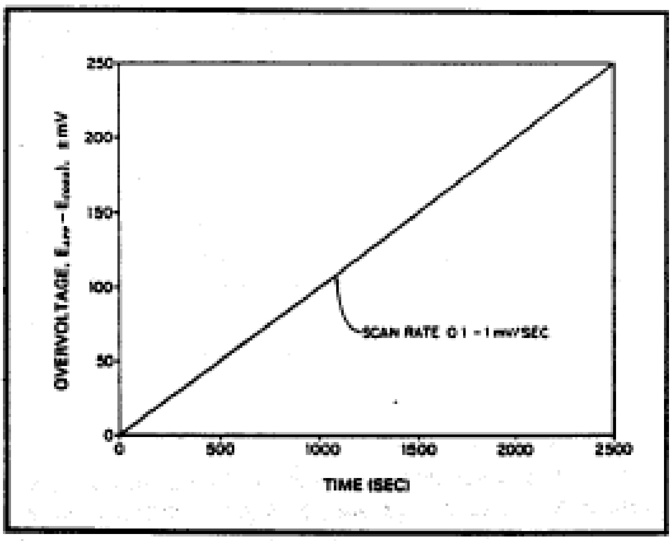

Figure 3.23: Potential scan of the polarization resistance by reference to current

The corrosion current I_{corr} Tafel diagram taken from a extrapolation of the linear portion of the curve at value of the corrosion potential (E_{corr}) (*Figure* 3.25). The corrosion rate can be calculated from the value of I_{corr} by the following equation:

$$\text{Corrosion Rate (mpy)} = \frac{0.13 * I_{corr} * (E.W.)}{d}$$

The anodic and cathodic Tafel graphs described by the Tafel equation:

$$\eta = \beta \log \frac{i}{I_{corr}}$$

Where:

η: overpotential, the difference between the potential of the specimen and the corrosion potential (E_{corr}),

β : Tafel constant,

I_{corr}: corrosion current,

i: current in overpotentional η, μA.

From the previous equation, arises the following:

$$\eta = \beta\ (\log i - \log I_{corr})$$

This equation has the form: $y = mx + b$, so a diagram of the overpotentional to logi is a straight line with slope β. In previous equation is observed that when $\eta = 0$ (E_{corr}), $\log i / I_{corr} = 0$ or $i / I_{corr} = 1$, or $i = I_{corr}$.

The Tafel constants β_α and β_c are calculated from the anodic and cathodic parts respectively of Tafel graph. The units for Tafel constants either mV / decade or V / decade. Tafel constants, as mentioned above, are used for calculation of the corrosion rate of polarization resistance data (***Figure 3.24***).

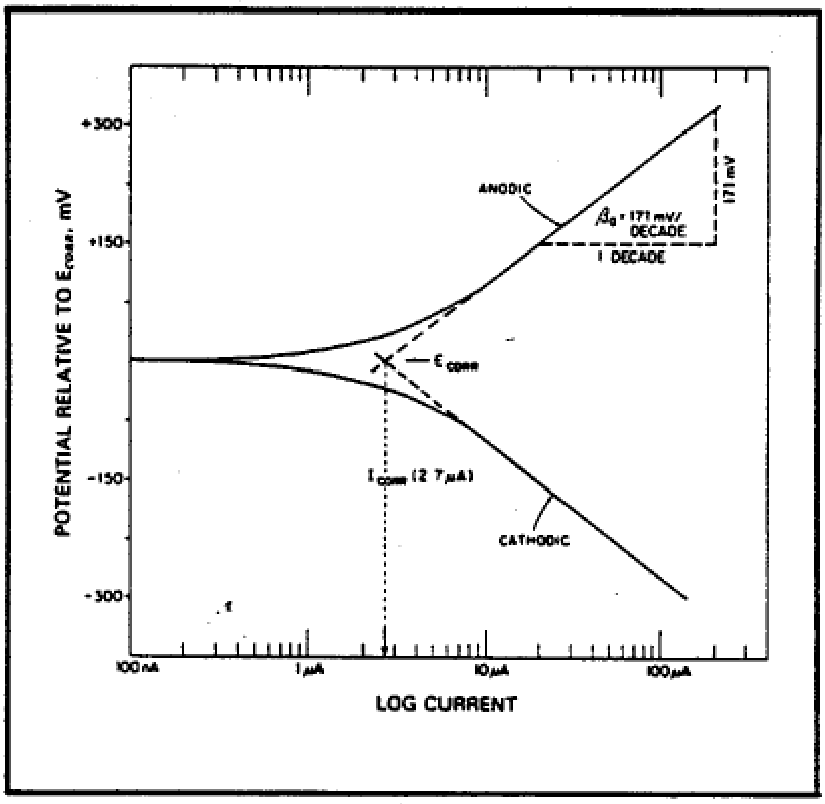

Figure 3.24: Typical Tafel graph

Tafel graphs provide a direct measurement of the corrosion current, which is related to the corrosion rate. This technique compared to the method of mass loss is extremely fast. The Tafel constants β_α and β_c, which are obtained, can be used in the method of Polarization Resistance to calculate the exact value of the corrosion rate.

One of the disadvantages of this method is the longer time duration of the measurement compared to the method of Linear Polarization. Also, because the range of polarization is large, the surface of the specimen is altered after the application of the method. Phenomena such as concentration polarization can affect the range of the linear area which makes it difficult to calculate the I_{corr}. Many times, also, happens that the extrapolations of the linear area of the anode and cathode part of the graph does not intersect the price of the E_{corr}. In most cases, the error is on the anodic area.

3.7.1.3. Electrochemical Impedance Spectroscopy (EIS)

The electrical resistance, as it was referenced above, is the ability of a circuit element to resist the flow of electrical current. Ohm's law defines resistance in terms of the ratio between voltage, E, and current, I.

$$R = \frac{E}{I} \quad : \text{ Ohm's law}$$

While this is a well-known relationship, its use is limited to only one circuit element, the ideal resistor. An ideal resistor has several simplifying properties:

- It follows Ohm's Law at all current and voltage levels.
- Its resistance value is independent of frequency.
- AC current and voltage signals though a resistor are in phase with each other.

However, the real world contains circuit elements that exhibit much more complex behavior. These elements force us to abandon the simple concept of resistance, and in its place we use impedance, a more general circuit parameter. Like resistance, impedance is a measure of the ability of a circuit to resist the flow of electrical current, but unlike resistance, it is not limited by the simplifying properties listed above.

Electrochemical impedance is usually measured by applying an AC potential to an electrochemical cell and then measuring the current through the cell. Assume that we apply a sinusoidal potential excitation. The response to this potential is an AC current signal. This current signal can be analyzed as a sum of sinusoidal functions (a Fourier series).

Electrochemical impedance is normally measured using a small excitation signal. This is done so that the cell's response is pseudo-linear. In a linear (or pseudo-linear) system, the current response to a sinusoidal potential will be a sinusoid at the same frequency but shifted in phase (***Figure 3.25***). Linearity is described in more detail in the following section.

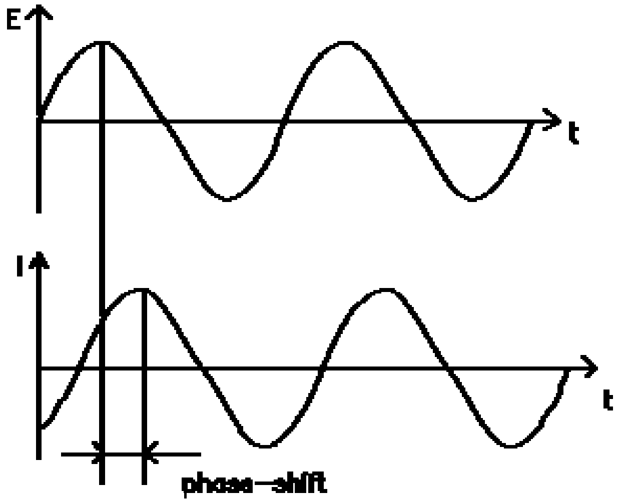

Figure 3.25: Sinusoidal Current Response in a Linear System

The excitation signal, expressed as a function of time, has the form:

$$E_t = E_0 \sin(\omega t)$$

where E_t is the potential at time t, E_0 is the amplitude of the signal, and ω is the radial frequency. The relationship between radial frequency ω (expressed in radians/second) and frequency f (expressed in hertz) is:

$$\omega = 2\pi f$$

In a linear system, the response signal, I_t, is shifted in phase (Φ) and has a different amplitude than I_0.

$$I = I_0 \sin(\omega t + \varphi)$$

An expression analogous to Ohm's Law allows us to calculate the impedance of the system as:

$$Z = \frac{E_t}{I_t} = \frac{E_0 \sin(\omega t)}{I_0 \sin(\omega t + \varphi)} = Z_0 \frac{\sin(\omega t)}{\sin(\omega t + \varphi)}$$

The impedance is therefore expressed in terms of a magnitude, Z_o, and a phase shift, Φ.

If we plot the applied sinusoidal signal E(t) on the X-axis of a graph and the sinusoidal response signal I(t) on the Y-axis, the result is an oval (***Figure 3.26***). This oval is known as a "Lissajous Figure". Analysis of Lissajous Figures on oscilloscope screens was the accepted method of impedance measurement prior to the availability of modern EIS instrumentation.

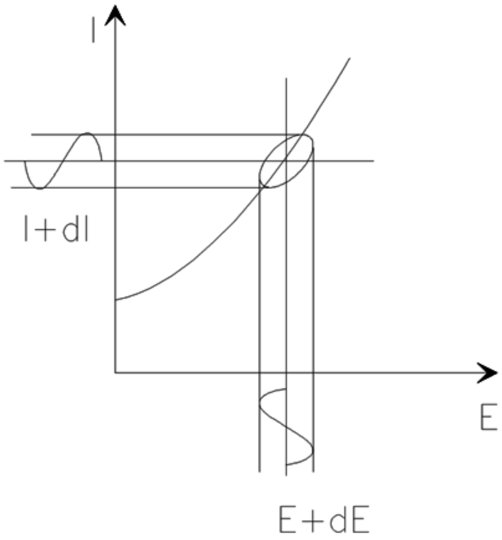

Figure 3.26: Origin of Lissajous Figure

With Euler's relationship,

$$\exp(j\varphi) = \cos\varphi + j\sin\varphi$$

It is possible to express the impedance as a complex function. The potential is described as,

$$E_t - E_o \exp(j\omega t)$$

and the current response as,

$$I_t = I_0 \exp(j\omega t - \varphi)$$

The impedance is then represented as a complex number,

$$Z(\omega) = \frac{E}{I} = Z_0 \exp(j\varphi) = Z_0(\cos\varphi + j\sin\varphi)$$

The expression for Z(ω), at the equation above, is composed of a real and an imaginary part. If the real part is plotted on the X-axis and the imaginary part is plotted on the Y-axis of a chart, we get a "Nyquist Plot". Notice that in this plot the Y-axis is negative and that each point on the Nyquist Plot is the impedance at one frequency. ***Figure 3.27*** has been annotated to show that low frequency data are on the right side of the plot and higher frequencies are on the left.

On the Nyquist Plot the impedance can be represented as a vector (arrow) of length |Z|. The angle between this vector and the X-axis, commonly called the “phase angle”, is f (=arg Z).

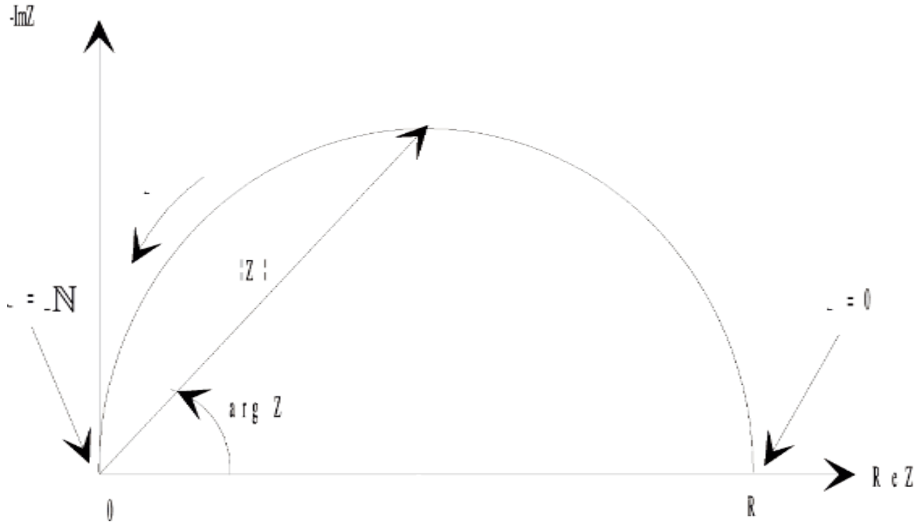

Figure 3.27: Nyquist Plot with Impedance Vector

Nyquist Plots have one major shortcoming. When you look at any data point on the plot, you cannot tell what frequency was used to record that point.

The Nyquist Plot in Figure results from the electrical circuit of ***Figure 3.28***. The semicircle is characteristic of a single "time constant". Electrochemical impedance plots often contain several semicircles. Often, only a portion f a semicircle is seen.

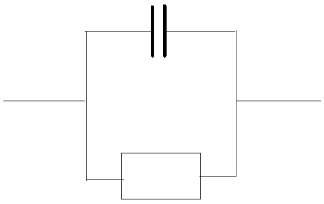

Figure 3.28: Simple Equivalent Circuit with One Time Constant

Another popular presentation method is the Bode Plot. The impedance is plotted with log frequency on the X-axis and both the absolute values of the impedance (|Z|=Z_0) and the phase-shift on the Y-axis.

The Bode Plot for the electric circuit is shown in ***Figure 3.29***. Unlike the Nyquist Plot, the Bode Plot does show frequency information.

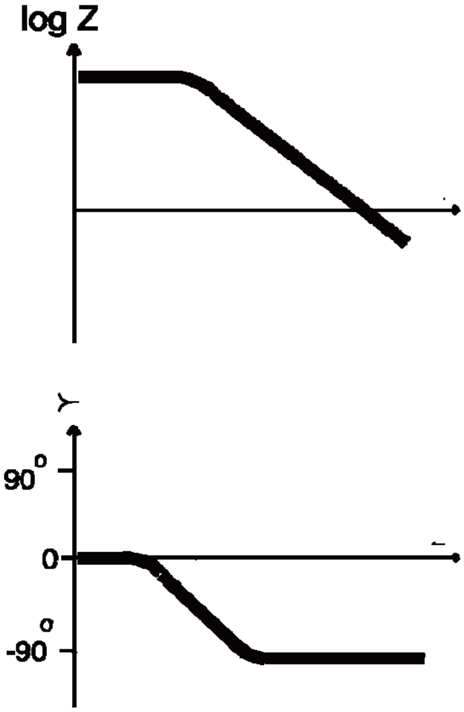

Figure 3.29: Bode Plot with One Time Constant

3.7.2. Experimental Setup

The experimental setup for carrying out the electrochemical measurements (***Figure 3.30***), consists of:

- Potentiostat-Galvanostat, VersaStat 4 of Princeton Applied Research,
- Electrolytic cell, K0235 Flat Cell - Princeton Applied Research,
- PC Pentium 4 CPU 1.6GHz, in which is installed software of "Virtual Potentiostat" for managing the potentiostat and of "PowerCorr" for taking polarization curves.

Based on the theory of electrochemical measurements, the study of the corrosion behavior is based on the potential of the specimen and the leaked current. The electrolytic cell (***Figure 3.31***) allows the measurement of the potential of the specimen (working electrode) in the electrolytic solution relative to the reference electrode.

The reference electrode f the cell, which is used in our experiment is the saturated calomel electrode (SCE) with potential E = + 244mV versus SHE. The electrode consists of a mercury reservoir covered with a paste of mercury - mercury chloride (calomel) immersed in potassium chloride. The contact is made with platinum wire immersed in mercury.

It is about the half element Cl^- / Hg_2Cl_2, Hg, whose action is:

$$Hg_2Cl_2 \Leftrightarrow 2Cl^- + Hg^{+2}$$

In practice it is usually used as electrolyte saturated KCl solution with a few crystals of solid KCl to maintain always the saturated nature of the solution.

The relative potential - current of the working electrode, with the potentiostatic method, is determined by applying constant potential between the working electrode and the counter electrode. The counter electrode is of an inert material (alloy of Platinum / Rhodium (Pt / Rh)). The change in potential at the working electrode due to current flow is measured against the reference electrode. The distance between the working electrode and counter electrode is 80 mm.

To minimize any voltage, drop due to the resistance of the solution (IRS drop - in the electrolyte, between the reference electrode and the working electrode), the reference electrode is in contact with the electrolytic solution through pipe which ends in thin capillary, known as capillary Luggin. This is placed near the surface of the working electrode, spaced not more than twice the outside diameter of the capillary. It is made of Teflon, diameter 0,6 mm, connecting the glass container (capacity 5 ml), into which the reference electrode is placed, to study the surface of the specimen (***Figure 3.31***).

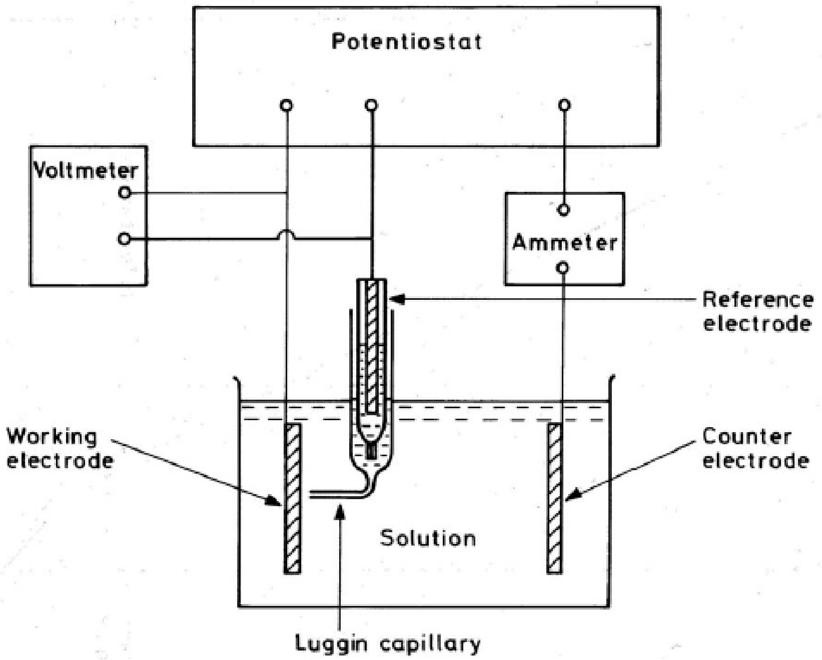

Figure 3.30: Schematic layout diagram for the determination of metal polarization curves in solution using potentiostat

In potenstiostatic method, the potential of the working electrode is given a specific value with the aid of a potentiostat. The imposed potential difference is applied between the working electrode and the reference electrode. The changes of the intensity of the current flowing through the electrolytic cell are measured or recorded at the end of a resistance located on the potentiostat between working electrode and counter electrode (***Figure 3.30***).

The device has a feed-back circuit for passing the suitable current from the working electrode so that the potential, which is measured against the reference electrode, is maintained at the desired value, independently of changes in current, corresponding to changes in the rate of reactions. The potentiostatic polarization method has the advantage that it can accurately monitor the behavior of metals, especially during formation and rupture of passivated layers, where the behavior mainly depends on the potential of the metal, and large changes in current may occur at a constant potential.

Chapter 4: Experimental results

4.1. Metallography of specimens

Metallography is the study of the structure of metals and alloys. The results of the optical microcopy are presented below. In the following paragraphs the microstructure of the specimens examined, are presented.

4.1.1. AH36 Parent Metal

Regarding the parent metal, ferritic-perlitic microstructure was observed as shown in ***Figure 4.1***. The ferritic structure has a greater extent, which was expected due to the chemical composition of steel (0.18% C). Also, the ferrite and pearlite grains have a strong orientation, due to the production process (rolling) of the steel plates. The orientation of the grains is vertical to the direction of load imposition. The specimens were etched Nital solution for 15 seconds.

(α) (b)

Figure 4.1: Parent Metal AH36

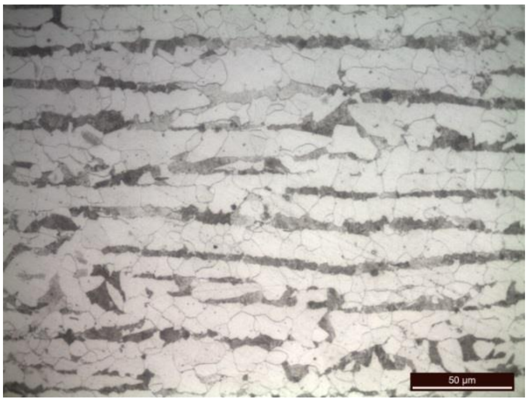

Figure 4.2: Parent Metal AH36

4.1.2. Similar AH36 – AH36 Friction Steel Welds

The following nomenclature is adopted in the present study in accordance with the terminology proposed by Threadgill and the main regions of the weld zone, which are illustrated in ***Figures 4.3 - 4.6***. The specimens were etched with Nital solution for 10 seconds to reveal the microstructure.

Where:

- AD: advancing side, the side where the rotating FSW tool pushes the metal towards the weld direction, i.e. forwards. The convention employed for the entire thesis is that samples are prepared so that the advancing side is presented on the left side of all images.
- RT: retreating side, the side where the rotating tool pushes the metal in a direction opposite to the weld direction, i.e. backwards.
- SZ: The zone where the FSW tool stirs the metal.
- TMAZ: Thermo-mechanically affected zone in which the material has been thermo-mechanically stirred by the FSW tool.
- Weld root: part of TMAZ, around and below the tip of the FSW tool's pin.
- HAZ: heat affected zone, where the metal has been affected by heat as it dissipates from the TMAZ, but not mechanically stirred.
- PM: Parent material, metal not affected by the process.

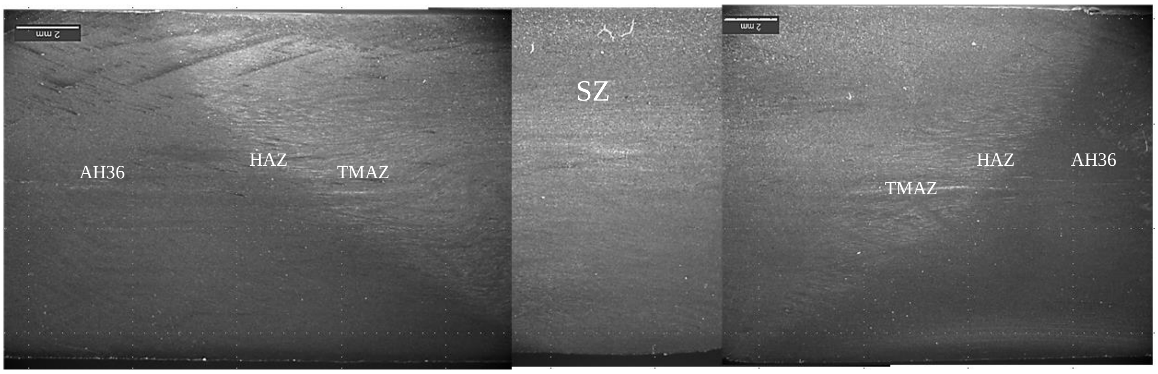

Figure 4.3: A macrograph of the friction stir weld region

The microstructure in the Stir Zone presents acicular ferrite Widmastätten and perlite. (***Figure 4.4***).

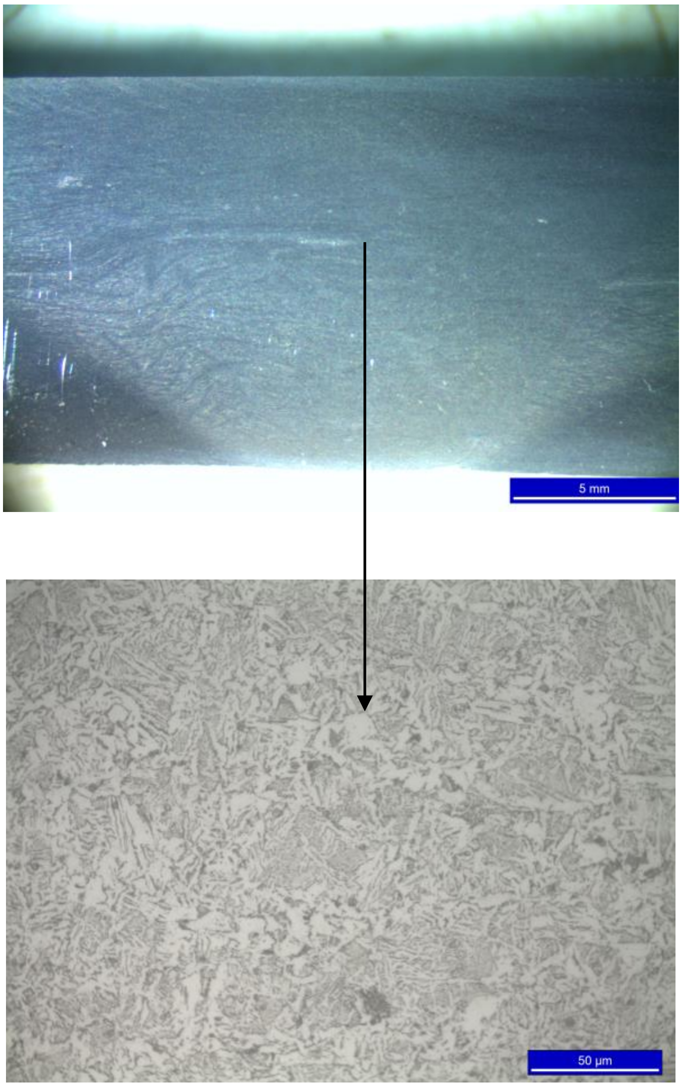

Figure 4.4: Microstructure of Stir Zone

The microstructure in the weld root presents ferrite and perlite (***Figure 4.5***).

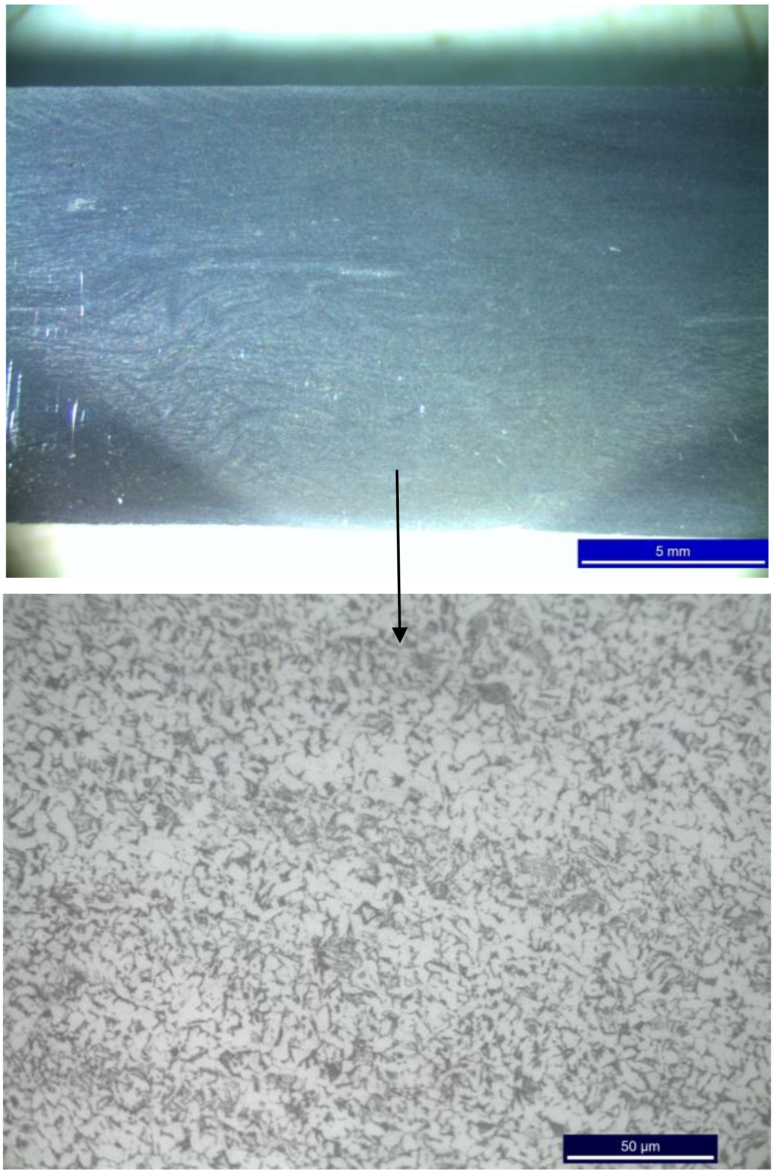

Figure 4.5: Microstructure of Weld root

4.1.3. Microstructure of S690 Parent Metal

The S690 steel, as an HSLA steel, is a combination of ferrite and bainite (***Figure 4.6***). The specimen had to stay 20 seconds in Nital solution for its observation with stereoscope and microscope. The microstructure of S690 consists of perlite, bainite and martensite recovery. No orientation of the grains is observed, owing to the thermo-mechanical process.

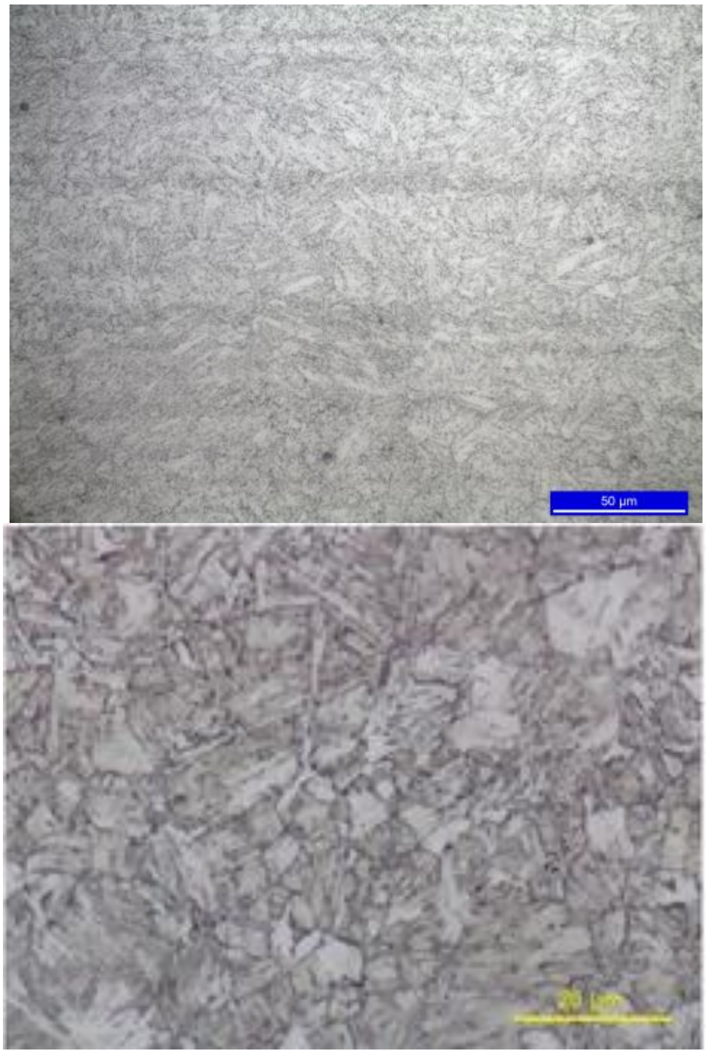

Figure 4.6: Microstructure of S690 steel

4.1.4. Similar S690 – S690 Flux Cored Arc Welds (FCAW)

The specimen had to stay 15 seconds in Nitan solution. According to the technical sheet of the welding procedure four passes have been performed (***Figure 4.7***).

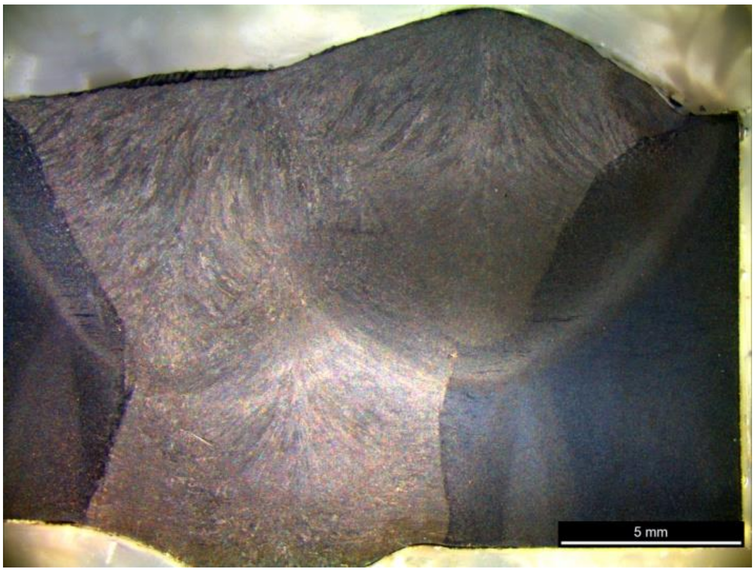

Figure 4.7: A typical macrograph of the ARC S690 - S690 weld region

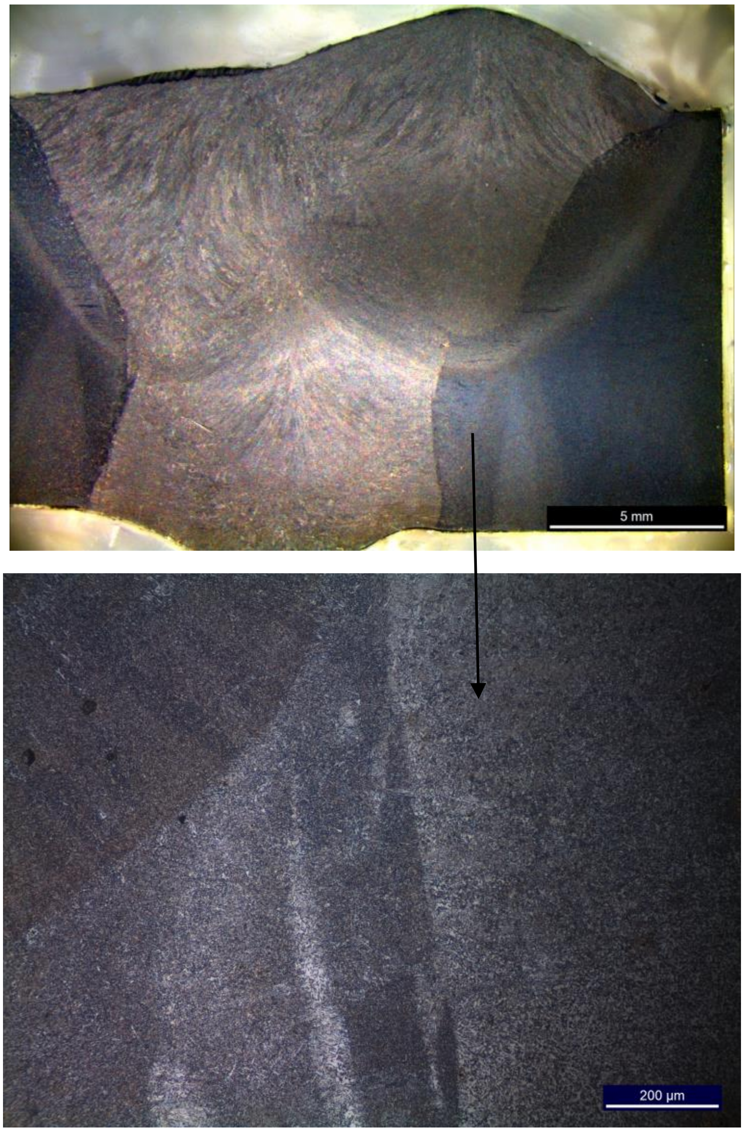

Figure 4.8: Heat affected zone in the 1st pass.

The HAZ in the 1st pass of the weld presents microstructure that consists of recovered martensite, ferrite, bainite and small amounts of remaining austenite ***(Figure 4.8)***.

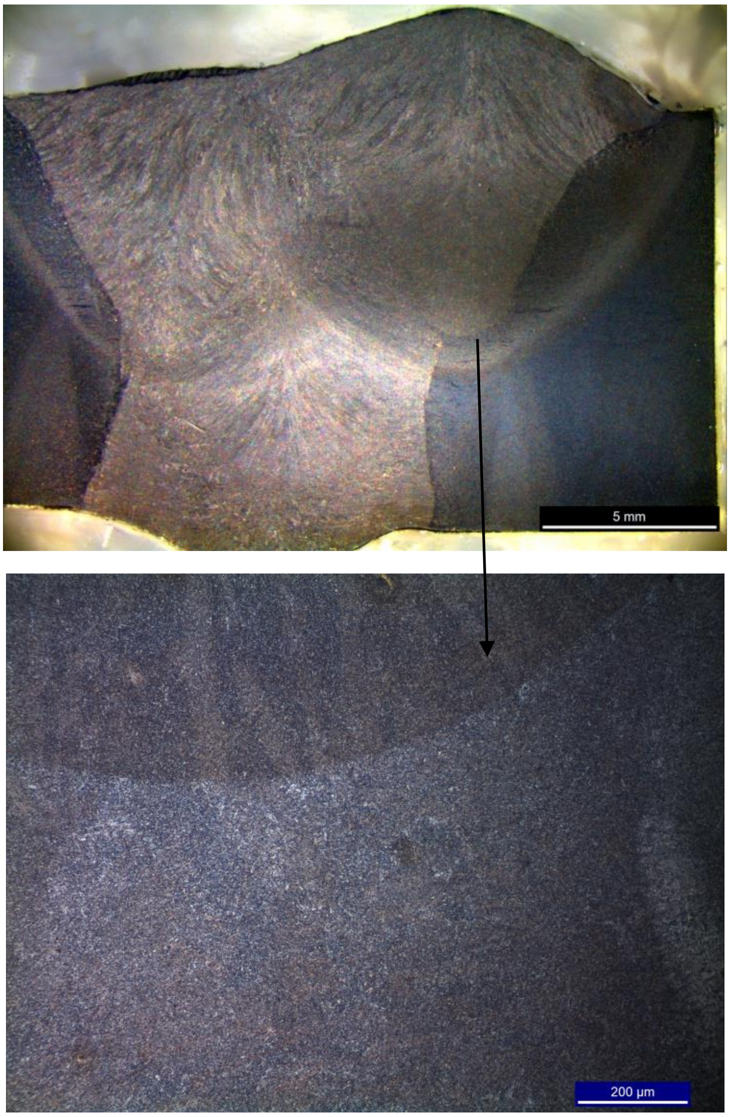

Figure 4.9: The interface of 4th pass HAZ of previous pass.

In ***Figure 4.9*** in the interface of the last 4th pass and the pass epitaxial growth of grains is observed.

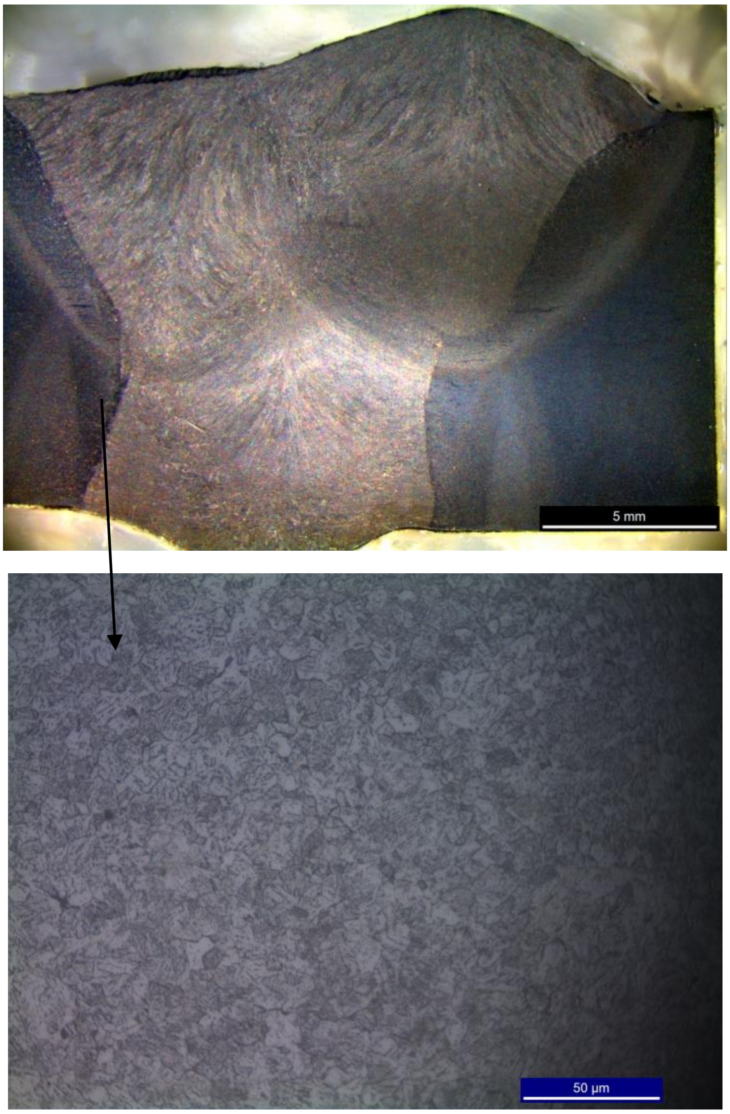

Figure 4.10: HAZ of the 1st pass

The HAZ in the 1st pass of the weld presents microstructure that consists of recovered martensite, ferrite, bainite and small amounts of remaining austenite (***Figure 4.10***).

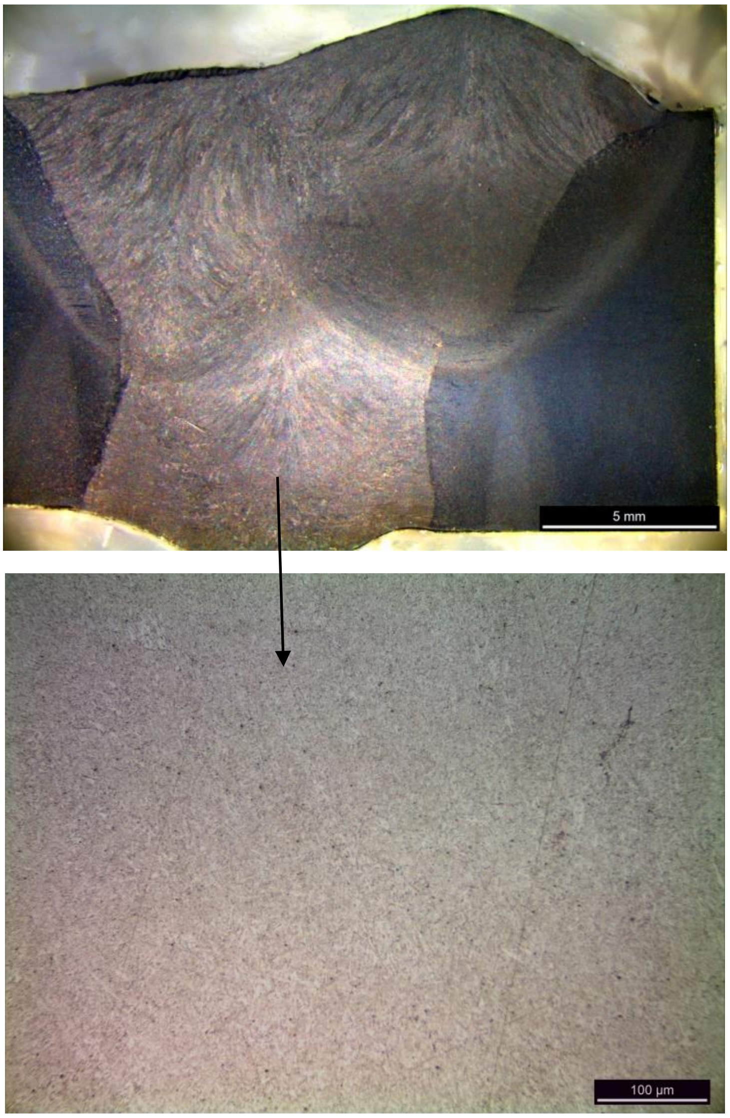

Figure 4.11: Microstructure of weld zone in the root of the weld.

The microstructure in the root of the weld consists of ferrite and bainite and presents dendritic formation of grains (***Fig. 4.11***).

4.2. Micro - hardness measurements

The micro - hardness measurements were performed on the same specimen, which was used for metallographic study. Two different sets of micro-hardness measurements were performed:

- in different heights of the weld section: in 1/3 and 2/3 height from the weld root
- along the axis of the weld, on the weld section.

The distance between two different imprints of every penetrator measurement were performed every 150μm, in order to avoid the interference among the measurements, but also to ensure that the measurements are close enough to report the variations in micro-hardness.

4.2.1. Micro-hardness measurements for similar S690-S690 FCAW

Firstly, 284 measurements were made vertically to the weld axis in different heights from the weld root, as aforementioned (1/3 and 2/3 height), (***Figure 4.14***).

The measurements in 1/3 height from the weld root show that the values in the weld zone rise up to 320 HV next to the weld axis, while they fall to 200 HV for the HAZ. The values in 2/3 height from the weld root are in general lower due to the annealing of this part of the weld. The values for the weld zone rise up to 280 HV, while for the HAZ fall to 200 HV.

After that, 49 measurements were made vertical to the welding, along the axis of the welding. The diagonal of the pyramid of the penetrator imprint was measured about the 50 μm. The measurements were made every three diagonals, as defined by the references. The results are represented in ***Figure 4.15***. According to these results, the values do not differ a lot from the values of the parent metal S690, the range from 270HV to 310HV. However, in the area among the 2nd and the 3rd- 4th passes, the values are lower 240HV, owing to the annealing of the 2nd pass.

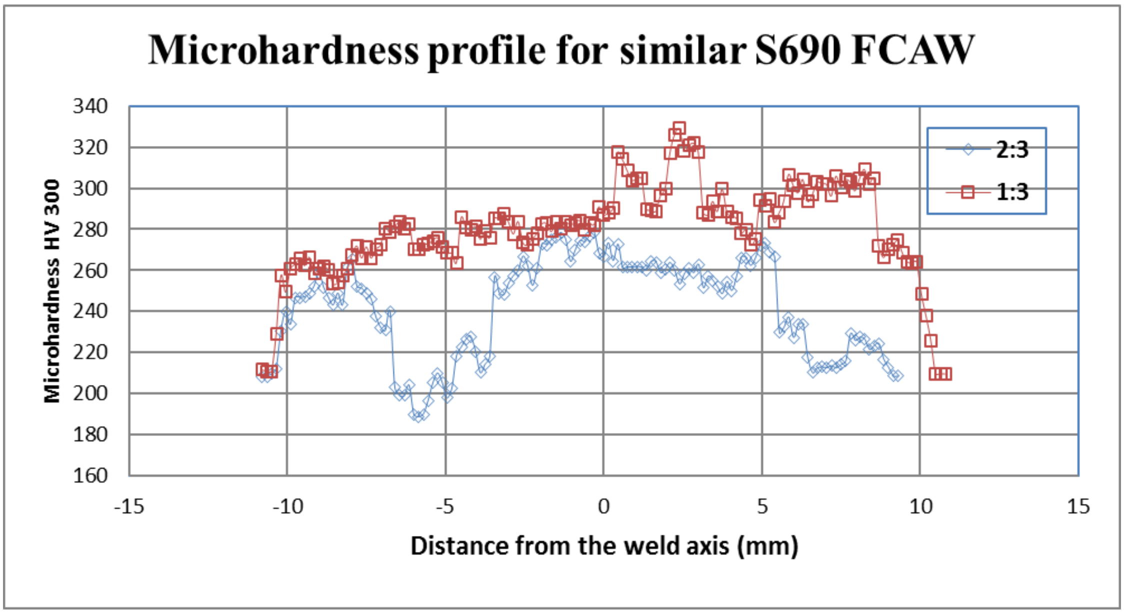

Figure 4.14: Micro-hardness profile for similar S690 - S690 FCAW

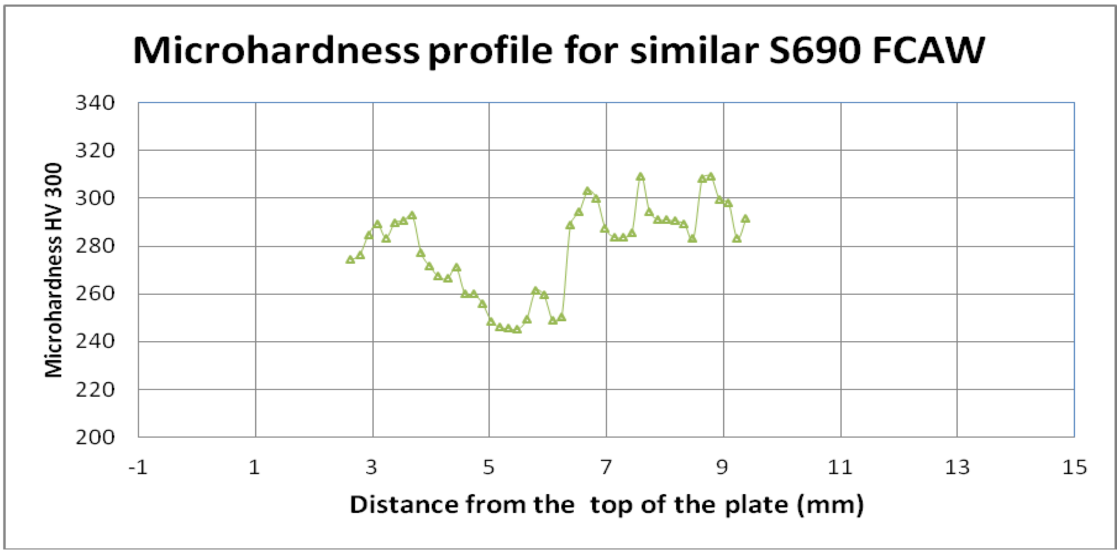

Figure 4.15: Microhardness profile for S690 - S690 FCAW lengthwise

4.2.2. Similar AH36- AH36 Friction Stir Weld

The measurements were made by the same way, as mentioned in the previous subsection. The results obtained are presented in ***Figures 4.16*** and ***4.17***.

In 15mm distance from the axis of the weld the parent metal hardness is obtained, 180HV in accordance to the literature.

The measurements on the section of the weld in 1/3 and 2/3 height of the weld gave the following results:

- In the lower part close to the weld root 1/3 height, show that the values in Stir Zone are 210HV, lower for the HAZ 200HV and finally 180HV for the parent metal (***Figure 4.16***).
- In 2/3 height the measurements in the SZ and the TMAZ zone raise to 230HV, while for the HAZ the values are lower: 200HV (***Figure 4.16***).

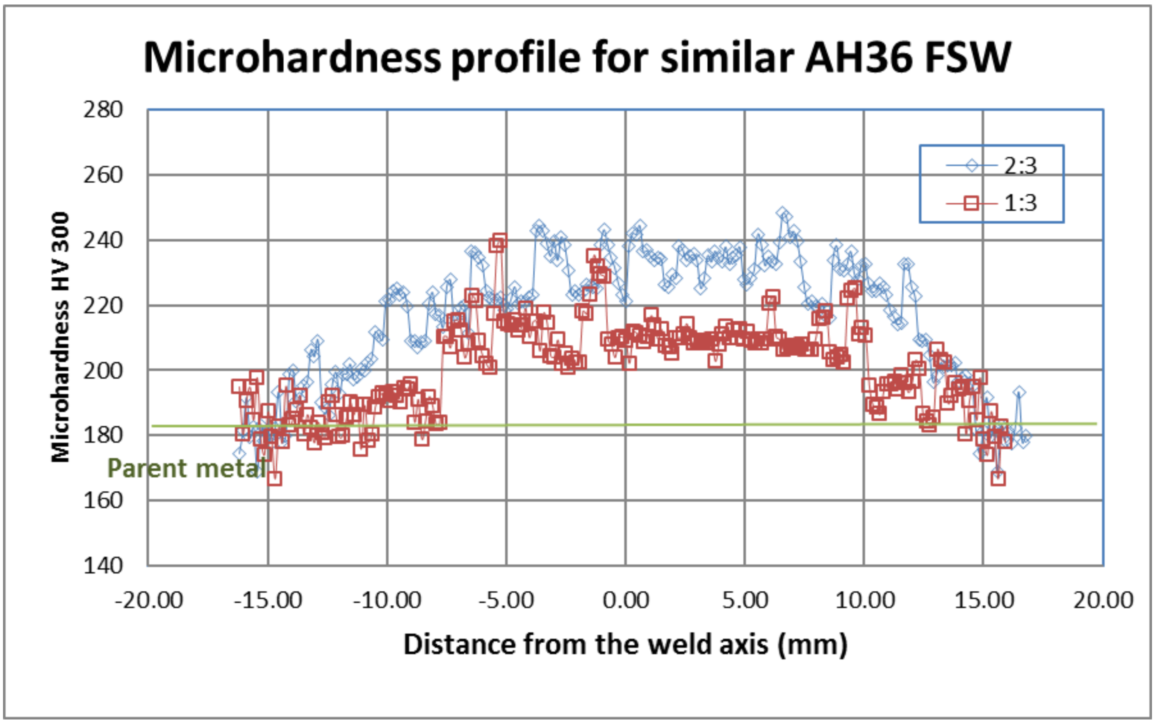

Figure 4.16: Microhardness profile for AH36 - AH36 FSW

The measurements on the section of the weld, along the axis show that on the top of the weld the values are close to the parent metal values and proceed to higher values, until 230-240HV on the weld root (***Figure 4.17***).

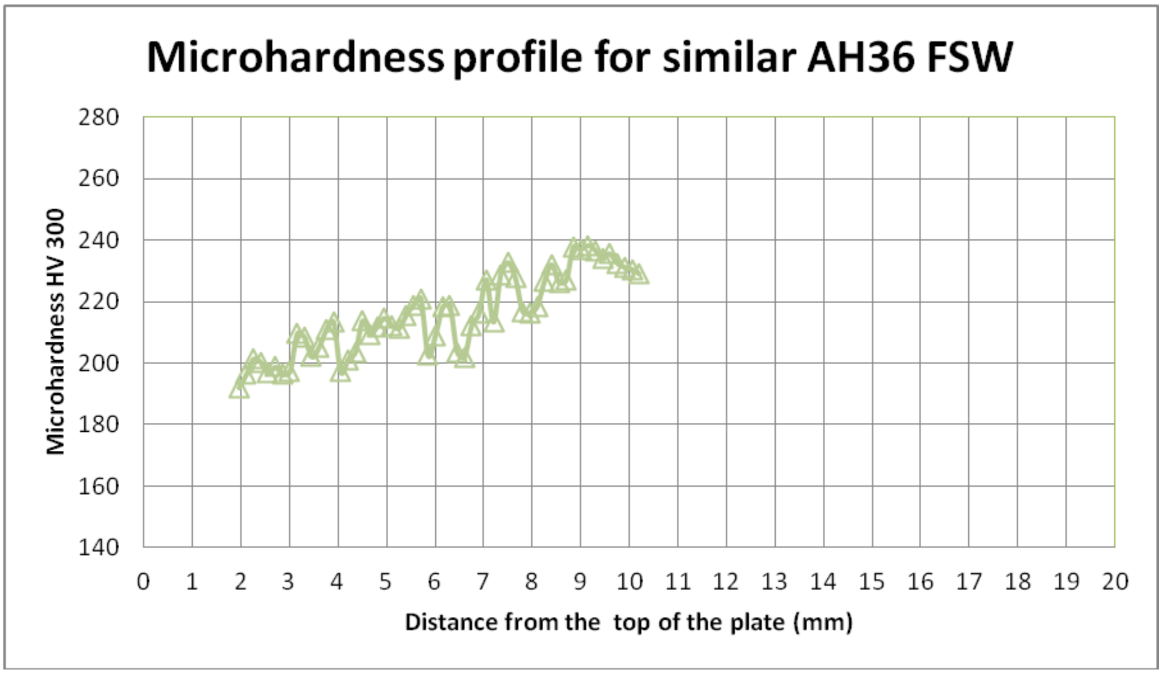

Figure 4.17: Microhardness profile for AH36 - AH36 FSW

4.3. Accelerating Tests in the Salt Spray Chamber

4.3.1. Exposure Program of the Specimens in the Climatic Chamber

The accelerating tests in the salt spray chamber were performed according to Planned Interval Test, as described in the previous Chapter 3. The experiment started on January 14th and finished on February 13th, 2015. The specimens' placement and removal from the chamber is described in ***Tables 4.1 and 4.2***. Different specimens were placed in the chamber, for the same time period, but in different moments of the experimental procedure, e.g. for 15 cycles (5 days) exposure one specimen was placed in day 1 and removed in day 5 (regular specimen), and another specimen was placed in day 25 and removed in day 30 (interval specimen). In the following tables 4.1, 4.2 with red color are presented the interval specimens, with black color are presented the regular ones, and with green color are presented the regular specimens, which remained in the chamber for the entire period (30 days).

After the removal from the chamber, a specific procedure was followed for each specimen. Each specimen was photographed, rinsed off with tap water, the corrosion products were removed, re-photographed and finally weighted in order to define the weight loss. All these data were recorded in a form. This form is shown in the ***Table 4.3***.

Time of stay in the chamber in days *(cycles)*	**Specimens**			
	Weld.		**Parent metal**	
	regular	**interval**	**regular**	**interval**
5 *(15)*	IIA2	IIIA2	HC1, HC2	IA3, IB3
10 *(30)*	IIB22	IIIB2	HC3, HC5	IC1, IC3
15 *(45)*	IA2	IIIC2	IA1, HC6	IIA1, IIA3
20 *(60)*	IC2	IVA2	HC7, HC8	IIB1, IIB3
25 *(75)*	IB2	IVB2	HC9, HC10	IIC1, IIC3
30 *(90)*	IB2, VA2		HC11, IB1, IIIA1, IIIA3	

Table 4 1: Program of specimen installation in the chamber, FCAW - PM S690

Time of stay in the chamber in days *(cycles)*	**Specimens**	
	Weld.	
	regular	**interval**
5 *(15)*	S40002	S40007
10 *(30)*	S40003	S400010
15 *(45)*	S40009	S400011
20 *(60)*	S40004	S400012
25 *(75)*	S40005	S400013
30 *(90)*	S40006, S40008	

Table 4.2: Program of specimen installation in the chamber, FSW AH36

Exposure time in the chamber (days)	
The characterization of specimen:	
Date of entry:	
Date of exit:	

Specified procedure:

a. Removal of the protective tape from the specimen

b. Photographing the specimen

c. Removal of corrosion products with the reagent (according to ISO 8407)

d. Cleaning with distilled water and ethanol

e. Drying in air

f. Re-photographing the specimen

g. Weighing

h. Installing in the dryer

i. Photo resolution

j. Observation in stereoscope

Initial weight (g)	m_i =
Final weight (g)	m_f =
Weight change	Dm = m_i - m_f =

Table 4.3 The form for the specimens after their removal from salt spray chamber.

4.3.2. Results of Accelerated Testing – Corrosion Rate

According to ASTM G31-72, the Corrosion Rate was calculated by the equation above:

$$\text{Corrosion\_rate} = \frac{K \times W}{A \times T \times D}$$

Where:

K: a constant (depending on the unit of measurement of corrosion rate (***Table 4.3***), equal to 8.76×10^4 for calculation in mm / year.

W: mass loss in g, to nearest 1 mg,

A: area of exposure in cm^2 to the nearest 0,01 cm^2. The exposure area was calculated for each specimen, considering the parallelogram with sides equal to the average of the two sides, minus the surface, which was covered by the protective tape. For each welded specimen was measured, through image processing from the stereomicroscope, the arc length of the weld. For the area, the peak areas of the surface of the melting zone (seam) and the rest of the specimen (HAZ and PM).

T: time of exposure in hours to the nearest 0.01h,

D: density in g/cm^3, equal to 7.86 g/cm^3.

According to ISO 14993 the depth of corrosion can be calculated in connection with the change in mass, by this equation:

$$\text{Depth of Corrosion} = \frac{W}{A \times D}$$

Where:

W: mass loss (g) with millimeter accuracy of g.

A: The display surface (cm^2) (accurately 0.01cm^2), as above.

D: steel density (g / cm^2) ≈ 7,86 g / cm^2 (For both AH36 and S690).

In the tables below (***Tables 4.4 - 4.7)*** the results for welded and parent metal specimens are presented. Each table shows the specimens' initial weight, the final weight, the weight loss (g) and % rate, the exposure time in hours, days and cycles, the exposed surface, the corrosion depth and then the corrosion rate of each specimen.

α/α	Specimen	Regular / Interval	Initial Weight (g)	Final Weight (g)	Difference (g)	Exposure time (hrs)	Cycles	Days	A (cm^2)	Corrosion depth (μm)	Corrosion rate (mpy)	Corrosion rate (mm / year)	Variation %
1	S40002	r	655,700	653,700	2,000	120	15	5	55,440	45,897	131,954	3,350	0,305
2	S40007	i	651,900	649,100	2,800	120	15	5	48,060	74,123	213,103	5,411	0,430
3	S40005	r	654,800	650,700	4,100	240	30	10	53,100	98,235	141,213	3,586	0,626
4	S400010	i	656,400	651,800	4,600	240	30	10	50,400	116,119	166,922	4,238	0,701
5	S40009	r	652,200	645,900	6,300	360	45	15	52,200	153,549	147,151	3,736	0,966
6	S400011	i	659,400	652,500	6,900	360	45	15	51,620	170,062	162,977	4,138	1,046
7	S40004	r	654,600	646,900	7,700	480	60	20	54,000	181,416	130,392	3,311	1,176
8	S400012	i	657,000	649,700	7,300	480	60	20	54,280	171,104	122,981	3,123	1,111
9	S40003	r	654,700	646,300	8,400	600	75	25	54,870	194,770	111,993	2,844	1,283
10	S400013	i	662,700	655,300	7,400	600	75	25	43,160	218,136	125,428	3,185	1,117
11	S40006	r	652,600	642,400	10,200	720	90	30	51,300	252,965	121,212	3,078	1,563
12	S40008	r	653,700	642,600	11,100	720	90	30	55,460	254,636	122,013	3,098	1,698

Table 4.4: Results for Accelerated Testing of Friction Stir Welding Specimens (S690 – S690)

α/α	Specimen	Regular / Interval	Initial Weight (g)	Final Weight (g)	Difference (g)	Exposure time (hrs)	Cycles	Days	A (cm^2)	Corrosion depth (μm)	Corrosion rate (mpy)	Corrosion rate (mm /year)
1	HC1	r	655,800	653,500	2,300	120	15	15	50,150	58,054	166,904	4,259
2	HC2	r	654,400	651,900	2,500	120	15	15	53,400	59,261	170,376	4,348
3	IA3	i	721,800	718,400	3,400	120	15	15	47,880	89,887	258,426	6,595
4	IB3	i	696,700	693,500	3,200	120	15	15	47,310	85,619	246,155	6,282
5	HC6	r	656,100	650,900	5,200	240	30	30	53,100	123,960	178,193	4,548
6	IIIA1	r	712,200	707,100	5,100	240	30	30	55,440	116,445	167,389	4,272
7	IC1	i	696,100	690,300	5,800	240	30	30	55,180	133,051	191,261	4,881
8	IC3	i	721,600	716,000	5,600	240	30	30	51,040	138,883	199,645	5,095
9	HC5	r	654,800	648,100	6,700	360	45	45	57,040	148,685	142,490	3,636
10	IA1	r	703,100	696,400	6,700	360	45	45	59,800	141,823	135,914	3,469
11	IIA1	i	709,800	702,500	7,300	360	45	45	56,730	162,886	156,099	3,984
12	IIA3	i	667,000	659,600	7,400	360	45	45	50,740	184,610	176,917	4,515
13	HC7	r	654,700	646,800	7,900	480	60	60	54,000	185,185	133,102	3,397
14	HC8	r	655,600	648,100	7,500	480	60	60	52,200	181,871	130,720	3,336
15	IIB1	i	706,500	698,700	7,800	480	60	60	54,000	182,841	131,417	3,354
16	IIB3	i	682,000	674,000	8,000	480	60	60	51,000	198,560	142,715	3,642
17	HC9	r	655,100	646,000	9,100	600	75	75	54,810	210,162	120,843	3,084
18	HC10	r	654,500	645,500	9,000	600	75	75	54,870	207,625	119,385	3,047
19	IIC1	i	689,200	680,900	8,300	600	75	75	55,180	190,401	109,481	2,794
20	IIC3	i	718,000	709,400	8,600	600	75	75	52,460	207,512	119,319	3,045
21	HC3	r	653,800	644,200	9,600	720	90	90	46,980	258,661	123,942	3,163
22	HC11	r	656,600	646,900	9,700	720	90	90	55,800	220,044	105,438	2,691
23	IB1	r	730,100	720,000	10,100	720	90	90	63,050	202,773	97,162	2,480
24	IIIA3	r	690,600	681,200	9,400	720	90	90	57,000	208,750	100,026	2,553

Table 4.5: Results for Accelerated Testing of Parent Metal Specimens S690

α/α	Specimen	Regular / Interval	Initial Weight (g)	Final Weight (g)	Difference (g)	Exposure time (hrs)	Cycles	Days	A (cm^2)	Corrosion depth (μm)	Corrosion rate (mpy)	Corrosion rate (mm /year)	Variation %
1	VIC4	r	932,000	930,000	2,000	116	14,500	4,833	47,312	53,782	159,954	4,061	0,215
2	VIIA5	r	943,000	941,000	2,000	116	14,500	4,833	47,259	53,842	160,134	4,066	0,212
3	VIA2	i	938,000	935,000	3,000	104	13,000	4,333	52,507	72,691	241,139	6,123	0,320
4	VIIC6	i	669,000	667,000	2,000	104	13,000	4,333	36,935	68,892	228,536	5,803	0,299
5	VIA5	r	943,000	939,000	4,000	229	28,625	9,542	43,221	117,744	177,388	4,504	0,424
6	VIIA4	r	941,000	937,000	4,000	229	28,625	9,542	43,945	115,805	174,466	4,430	0,425
7	VIC3	i	938,000	932,000	6,000	213	26,625	8,875	53,341	143,110	231,798	5,886	0,640
8	VIIC5	i	924,000	918,000	6,000	213	26,625	8,875	50,581	150,919	244,446	6,207	0,649
9	VIC1	r	949,000	943,000	6,000	326	40,750	13,583	46,453	164,331	173,909	4,416	0,632
10	VIIC2	r	938,000	933,000	5,000	326	40,750	13,583	44,289	143,632	152,003	3,860	0,533
11	VIA6	i	725,000	719,000	6,000	365	45,625	15,208	39,130	195,083	184,393	4,682	0,828
12	VIIA1	i	962,000	954,000	8,000	365	45,625	15,208	50,740	200,594	189,602	4,814	0,832
13	VIC5	r	936,000	929,000	7,000	478	59,750	19,917	44,686	199,300	143,846	3,652	0,748
14	VIIA6	r	655,000	650,000	5,000	478	59,750	19,917	30,762	206,795	149,256	3,790	0,763
15	VIA4	i	942,000	933,000	9,000	462	57,750	19,250	49,548	231,098	172,573	4,382	0,955
16	VIIC3	i	938,000	930,000	8,000	462	57,750	19,250	48,357	210,479	157,176	3,991	0,853
17	VIC6	r	715,000	707,000	8,000	587	73,375	24,458	36,749	276,965	162,782	4,133	1,119
18	VIIC4	r	930,000	922,000	8,000	587	73,375	24,458	46,750	217,714	127,958	3,249	0,860
19	VIA1	i	956,000	946,000	10,000	575	71,875	23,958	48,720	261,138	156,683	3,978	1,046
20	VIIA2	i	920,000	910,000	10,000	575	71,875	23,958	47,688	266,791	160,075	4,065	1,087
21	VIA3	r	939,000	930,000	9,000	691	86,375	28,792	45,900	249,464	124,551	3,163	0,958
22	VIC2	r	933,000	922,000	11,000	691	86,375	28,792	46,999	297,770	148,670	3,775	1,179
23	VIIC1	r	950,000	938,000	12,000	691	86,375	28,792	46,861	325,796	162,662	4,130	1,263

Table 4.6: Results for Accelerated Testing of Parent Metal Specimens AH36

α/α	Specimen	Regular / Interval	Initial Weight (g)	Final Weight (g)	Difference (g)	Exposure time (hrs)	Cycles	Days	A (cm^2)	Corrosion depth (μm)	Corrosion rate (mpy)	Corrosion rate (mm / year)	Variation %
1	IIA2	r	769,700	767,500	2,200	120	15	15	62,830	44,323	127,428	3,236	0,286
2	IIIA2	i	766,200	763,400	2,800	120	15	15	62,120	57,056	164,035	4,165	0,365
3	VA2	r	787,100	783,600	3,500	240	30	30	54,320	81,561	117,244	2,977	0,445
4	IIIB2	i	777,200	772,900	4,300	240	30	30	56,400	96,508	138,730	3,523	0,553
5	IA2	r	769,700	762,900	6,800	360	45	45	64,640	133,162	127,614	3,240	0,883
6	IIIC2	i	784,900	777,300	7,600	360	45	45	63,000	152,702	146,340	3,716	0,968
7	IC2	r	760,500	752,300	8,200	480	60	60	62,370	166,422	119,616	3,037	1,078
8	IVA2	i	769,000	760,600	8,400	480	60	60	60,140	176,803	127,077	3,227	1,092
9	IIC2	r	756,100	745,800	10,300	600	75	75	63,860	204,165	117,395	2,981	1,362
10	IVB2	i	768,700	758,700	10,000	600	75	75	51,300	246,749	141,881	3,621	1,301
11	IIB2	r	766,400	755,400	11,000	720	90	90	59,520	233,939	112,096	2,846	1,435
12	IB2	r	762,800	751,600	11,200	720	90	90	63,440	223,474	107,081	2,719	1,468

Table 4.7: Results for Accelerated Testing of Arc Welded Specimens (AH36 – AH36)

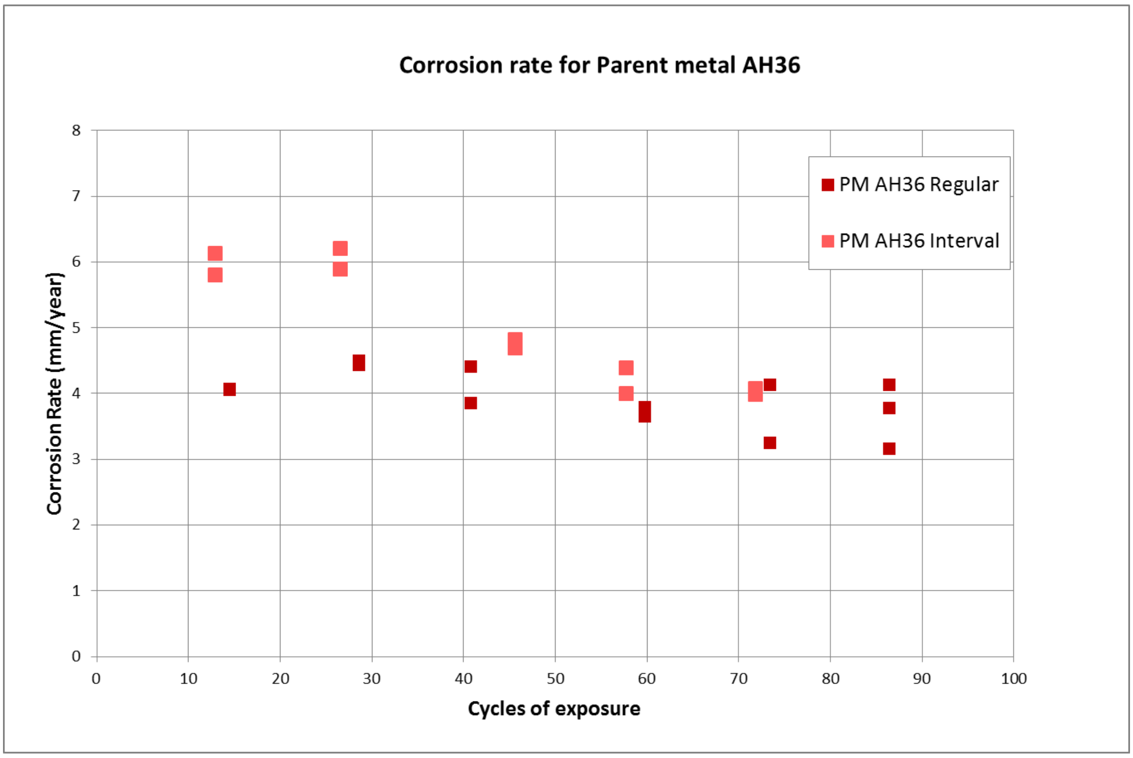

Figure 4.18: Corrosion Rate vs. cycles of exposure for Parent Metal AH36 specimens

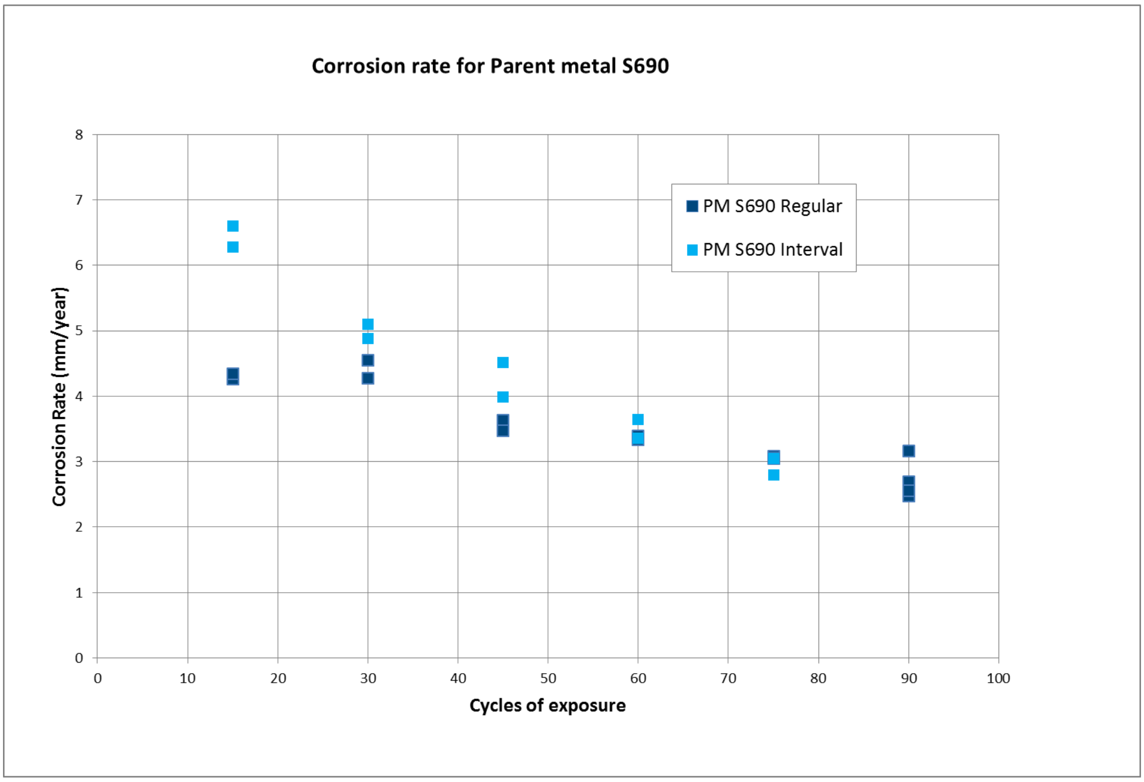

Figure 4.19: Corrosion Rate vs. cycles of exposure for Parent Metal S690 specimens

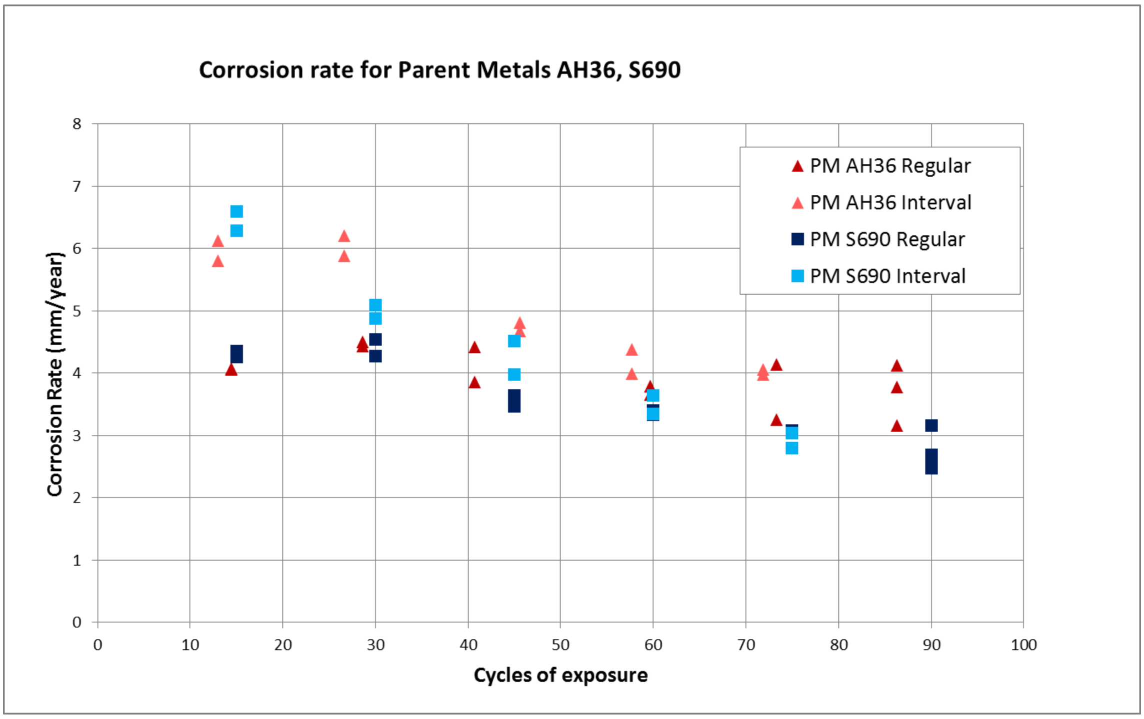

Figure 4.20: Corrosion rate vs. cycles of exposure for Parent Metal AH36 and S690 specimens

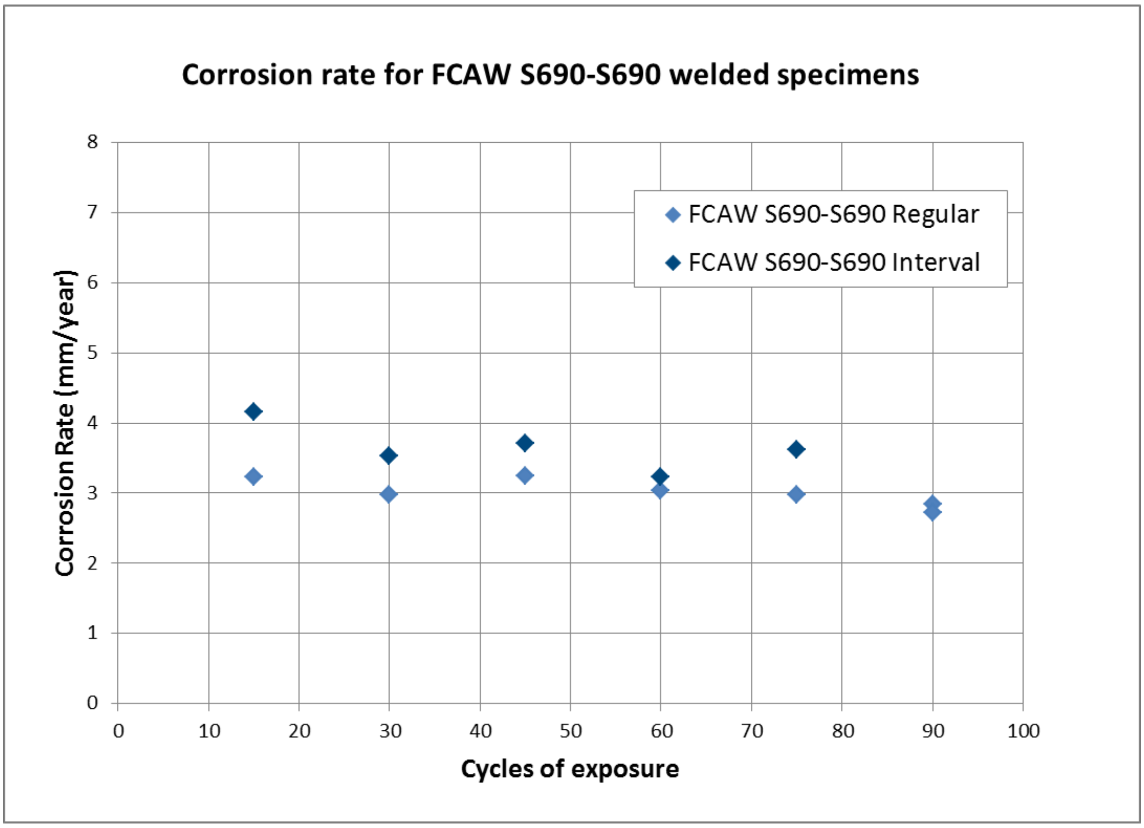

Figure 4.21: Corrosion rate vs. cycles of exposure for FCAW S690 welded specimens

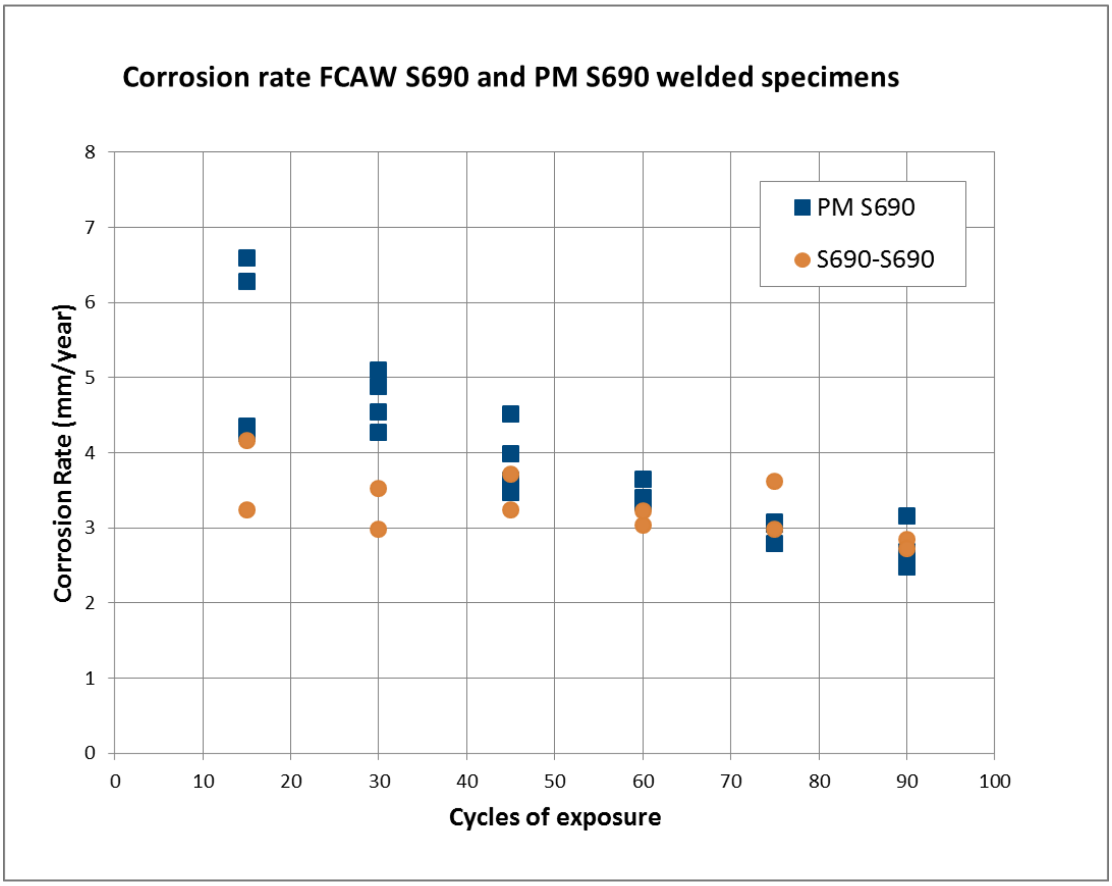

Figure 4.22: Corrosion Rate for Parent Metal and S690 and FCAW S690 welded specimens

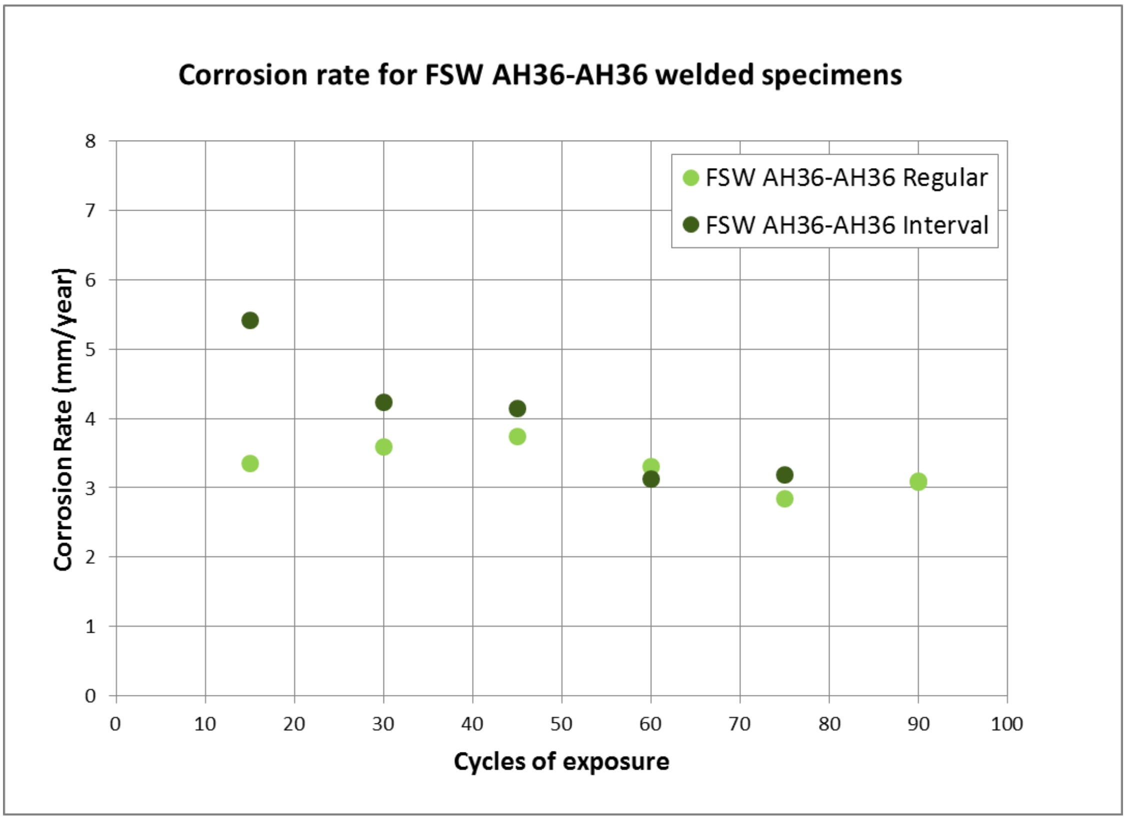

Figure 4.23: Corrosion Rate vs. cycles of exposure for FSW AH36 welded specimens

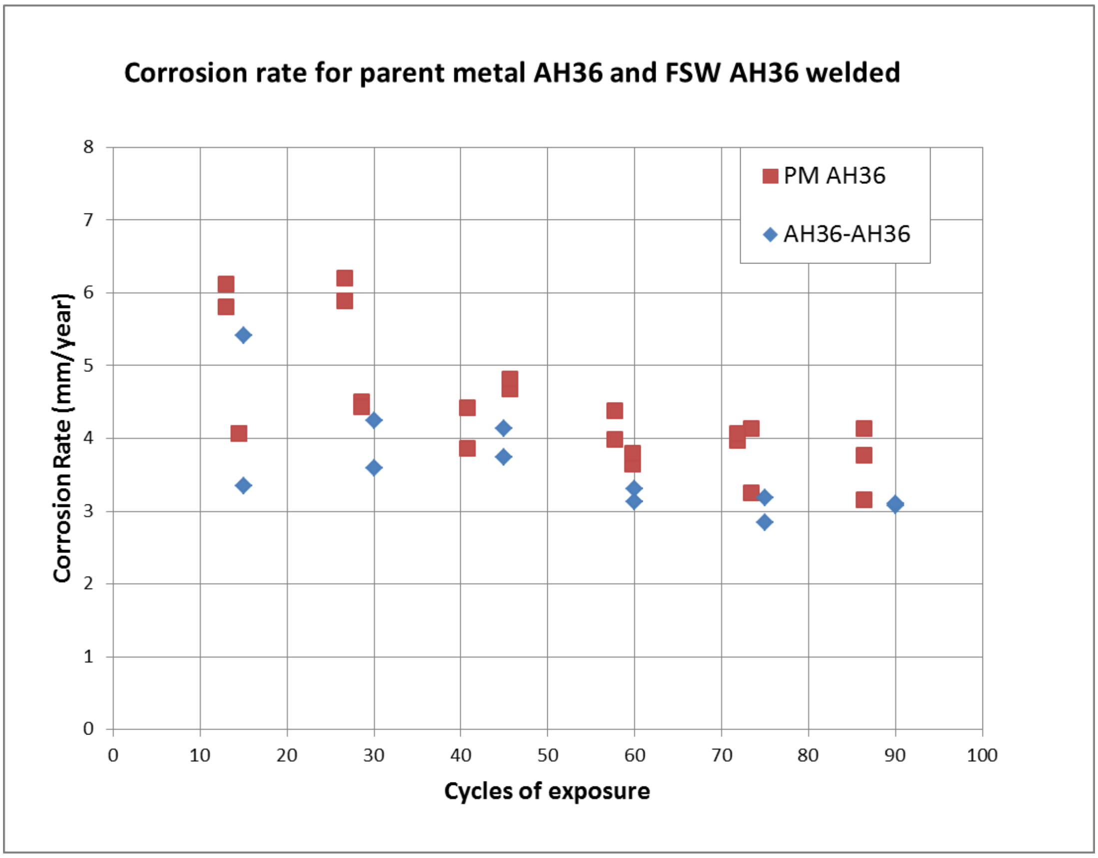

Figure 4.24: Corrosion Rate for Parent Metal and AH36 and FSW AH36 welded specimens

From the tables (***Table 4.4 - 4.7***) and figures (***Figures 4.18 – 4.24***) above, the following results are the most noteworthy:

- The average corrosion rate for the AH36 Parent Metal specimens is 4,398±0,49 mm/year (***Figure 4.18***, ***Table 4.5***).
- The average corrosion rate for the S690 Parent Metal specimens is 3,853±0,67 mm/year. (***Figure 4.19***, ***Table 4.4***).
- The S690 presents lower corrosion rate than AH36 Parent Metal (***Figure 4.20***).
- The average corrosion rate for the S690 FCAW specimens is 3,274±045 mm/year (***Figure 4.21***, ***Table.4.3***).
- The average corrosion rate for the AH36 FSW Parent Metal specimens is 3,591±058 mm/year. (***Figure 4.23***, ***Table 4.6***).
- The FSW specimens present lower corrosion rate than FCAW specimens.
- The highest corrosion rates show the interval specimens with small exposure times.
- For regular specimens observed increase in corrosion rate with increasing exposure cycles.
- In contrast, the corrosion rate of the interval specimens begins with high values and then decreases.
- For both welds (FCAW and FSW) is observed that the corrosion rate is lower than their Parent Metal corrosion rate (***Figure 4.21***, ***Figure 4.24***).
- With the increase in exposure cycles, the values of corrosion rate of regular and interval and specimens seem to converge (specimens that were exposed in the chamber for 60-70 cycles).

The ***Tables 4.4 – 4.7*** and the ***Figures.4.25 and 4.26***, concerning the calculated depth of corrosion in specimens versus exposure time, it is derived that the corrosion depth of the specimens increases almost linearly versus the exposure time for the specimens in the chamber, as expected.

For FCAW weld and S690 the final values reach at 250μm. For FSW the values for parent metal AH36 are higher, up to 300μm, while for FSW weld the values calculated at 250μm after 90 cycles of exposure.

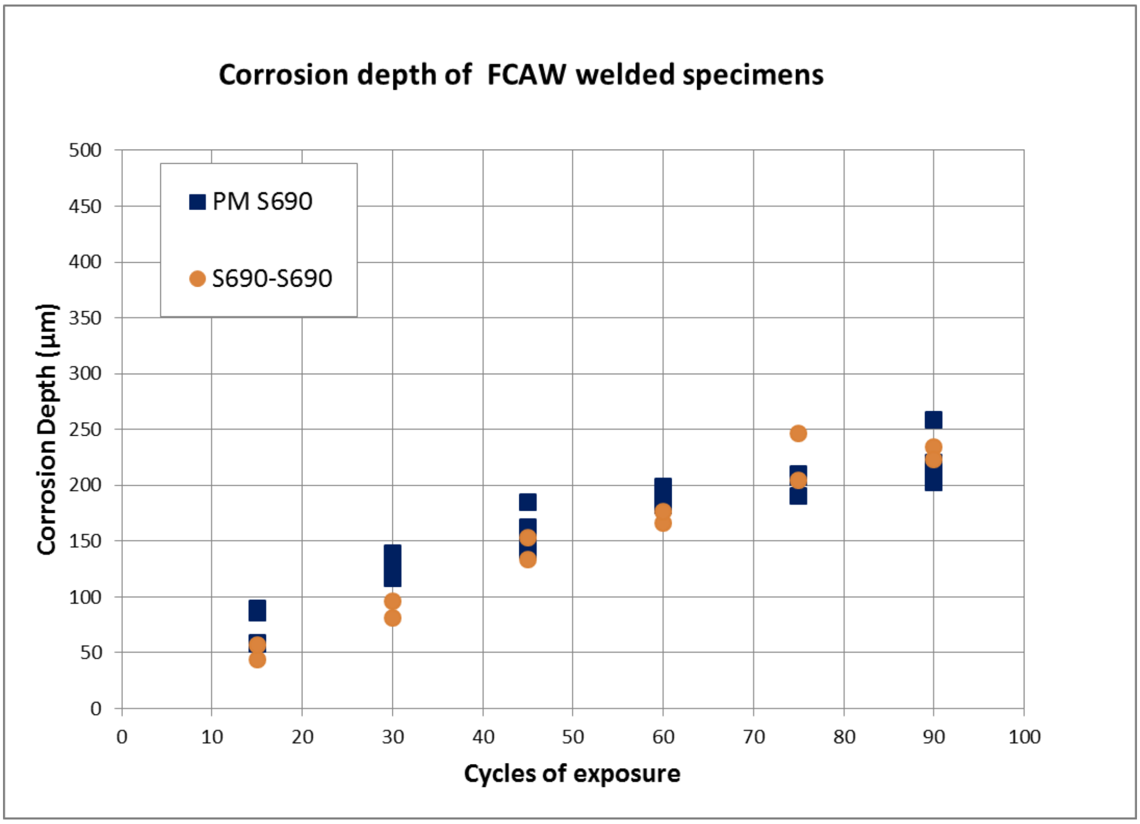

Figure 4.25: Corrosion depth versus Cycles of exposure for S690 PM - FCAW S690

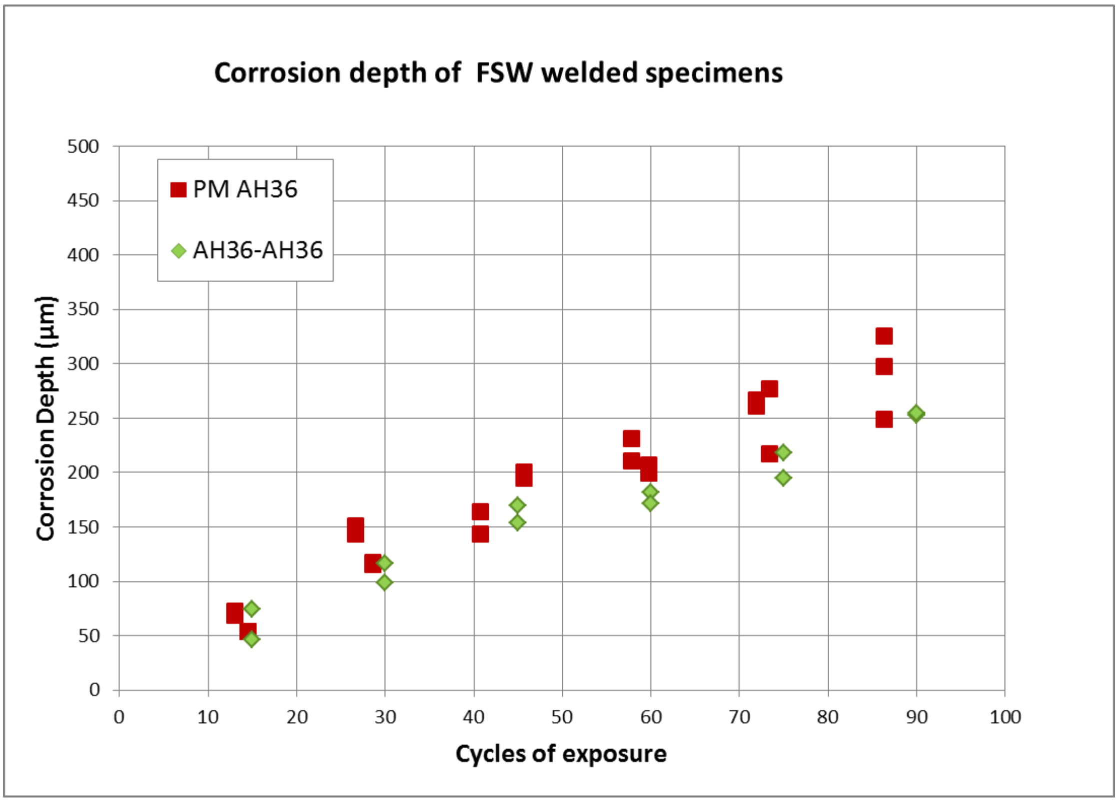

Figure 4.26: Corrosion depth versus Cycles of exposure for AH36 PM - FSW AH36

4.3.3. Macroscopic Observations

For the macroscopic study the specimens were photographed with a digital camera:

- before the installation in the salt spray chamber (***Figure 4.27(a)***),
- after their removal from the salt spray chamber (***Figure 4.27 (b)***),
- after the removal of corrosion products (***Figure 4.27 (c)***).

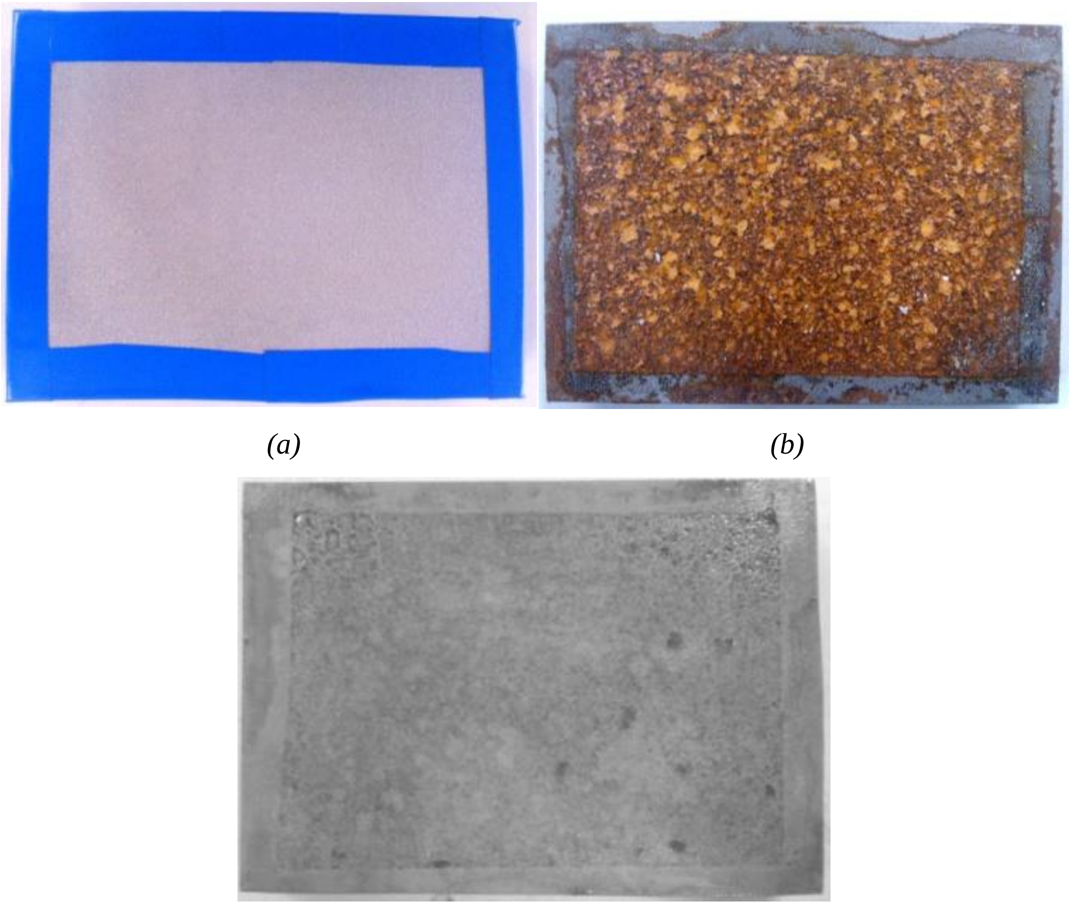

(a) *(b)*

(c)

Figure 4.27: (a) The sandblasted surface before the installation in the chamber, (b) The corroded surface after the chamber, (c) The cleaned surface after the removal of corrosion products

4.3.3.1. S690 Parent Metal specimens after the chamber

Observing the specimens exposed in the chamber for five (5) days, it is observed that exposed surface of each specimen completely covered by brown corrosion product. At the same time, they appear in places points with lighter color surrounded by grey outline.

Thereafter (10 days) these identified points are multiplied, grow in diameter and occupy increasingly larger area of the specimen. While in some specimens (mostly interval) observed the appearance of small craters. Some of these craters have been disrupted.

After of 15 days of staying in the chamber, the detected points are almost completely cover the surface of the specimen. The number of small craters increases, as well as the number of those who have disrupted.

After 20 days, these small craters linked together to form larger, the majority of which has been disrupted.

The combination of small craters to larger and their disruption is evolving until the end of the experiment. The upper layers of corrosion products can easily be broken and removed from the specimen.

All these are obvious in following ***Figure 4.28***:

Regular

Interval

HC1 15 Cycles

IA3 15 Cycles

IIIA1 30 Cycles

IC1 30 Cycles

IA1 45 Cycles IIA3 45 Cycles

HC8 60 Cycles IIB1 60 Cycles

HC9 75 Cycles IIC1 75 Cycles

IB1 90 Cycles IIIA3 90 Cycles

Figure 4.28: Comparison corroded surfaces of base metal AH36 specimens regular - interval, for different exposure times (15,30,45,60,75,90 cycles).

Comparing the specimens, which were placed from the start in the chamber according to the program (regular) to those, which were placed in the chamber later (interval), for the same residence times, it is observed that the phenomenon evolves more rapidly for the interval specimens. The difference is clearer for the specimens remain in the chamber for a short time, at different times, for example 5 days (0-5 and 25-30) and 10 days (0-10 and 20-30) (***Figure 4.28***).

4.3.3.2. Observations for the revealed surface of the S690 Parent Metal specimens after the removal of corrosion products

The removal of corrosion products from the surface of specimens reveals the morphology of corrosion. This form of corrosion, which is observed, is similar to that of pitting corrosion. The pits are evolving in width, joined with adjacent localized corrosion points by forming larger areas, while deepening eventually creating cavities. The depth of the cavities is increased as is increased the exposure time in the chamber of the specimens. It is, also, obvious, that the specimens have pits (***Figure 4.29***).

It was also observed that the corrosion initial products are removed easily from the surface of the specimen, but the difficulty is being increased as the residence time of the specimen in the chamber is being increased too, as it is shown below in ***Figure 4.29***.

Regular **Interval**

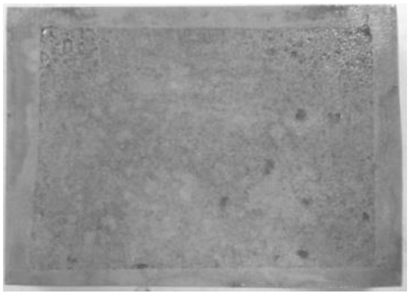

HC1 15 Cycles

IA3 15 Cycles

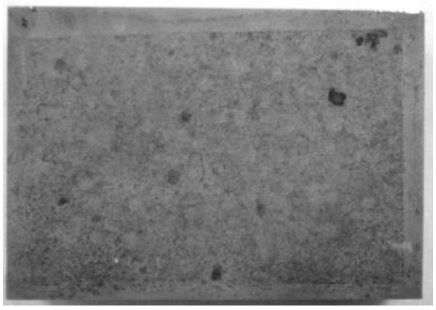

IIIA1 30 Cycles

IC1 30 Cycles

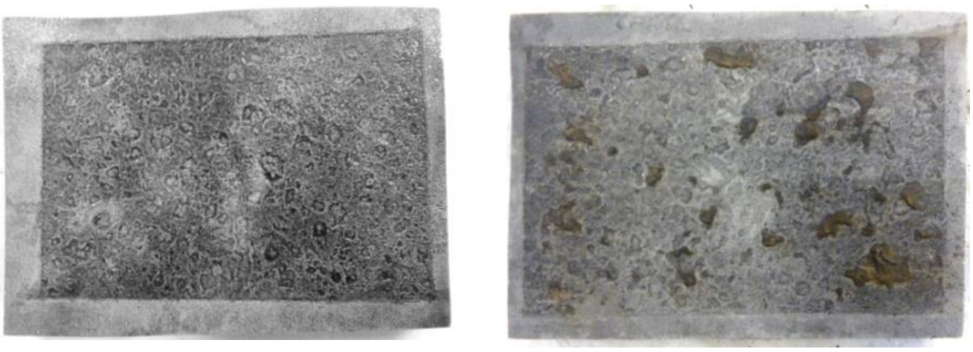

IA1 45 Cycles *IIA3 45 Cycles*

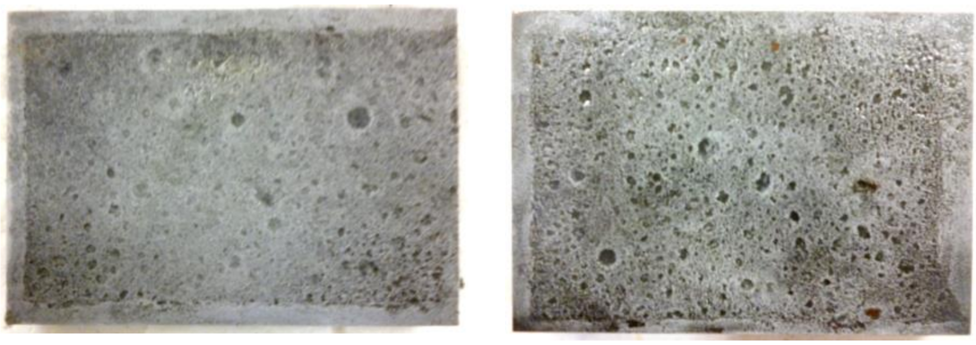

HC8 60 Cycles *IIB1 60 Cycles*

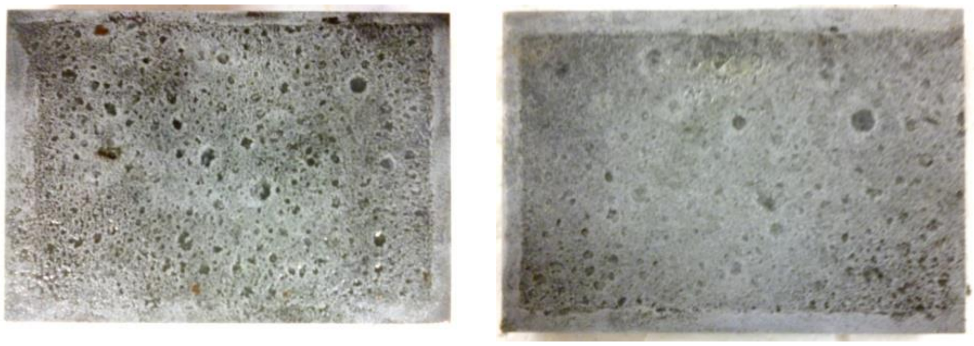

HC9 75 Cycles *IIC1 75 Cycles*

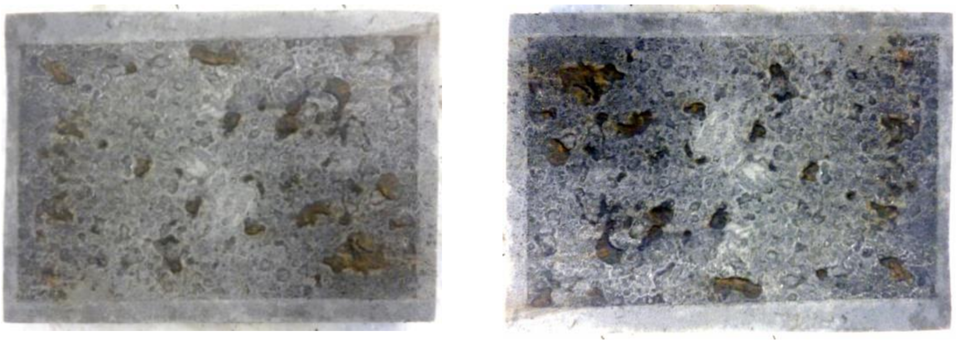

IB1 90 Cycles *IIIA3 90 Cycles*

Figure 4.29: Comparison of the base metal surfaces of the specimens regular - interval after removal of corrosion products for different exposure times).

4.3.3.3. Observations for the surface of the similar AH36 Friction Stir welded specimens after the chamber

It is observed that the development of corrosion on the specimens with welding follows the same pattern as in the base metal specimens. The images of specimens are listed below, after their removal form from the salt spray chamber are presented in ***Figure 4.30***.

Regular **Interval**

S40002 15 Cycles

S40007 15 Cycles

S40005 30 Cycles

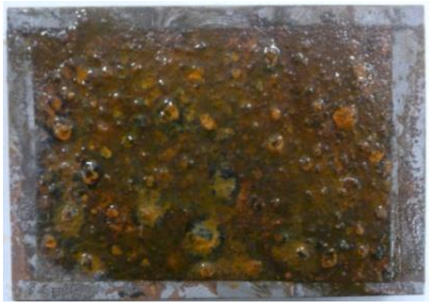

S400010 30 Cycles

S40009 45 Cycles

S400011 Cycles

S40004 60 Cycles

S400012 60 Cycles

S40003 75 Cycles

S400013 75 Cycles

S40008 90 Cycles

S40006 90 Cycles

Figure 4.30: Comparison of corroded surfaces of FSW specimens regular - interval, for different exposure times (15,30,45,60,75,90 cycles).

4.3.3.4. Observations for the surface of the similar AH36 Friction Stir welded specimens after the removal of corrosion products

The images below represent the welded specimens after the removal of corrosion products (***Figure 4.31***).

Regular **Interval**

S40002 15 Cycles

S40007 15 Cycles

S40005 30 Cycles

S400010 30 Cycles

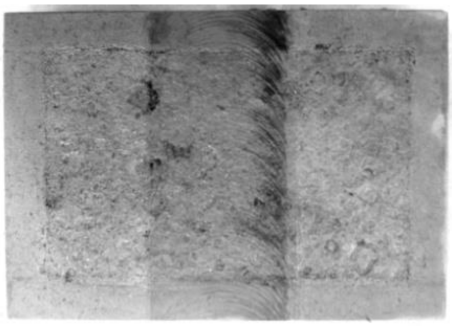

S40009 45 Cycles

S400011 Cycles

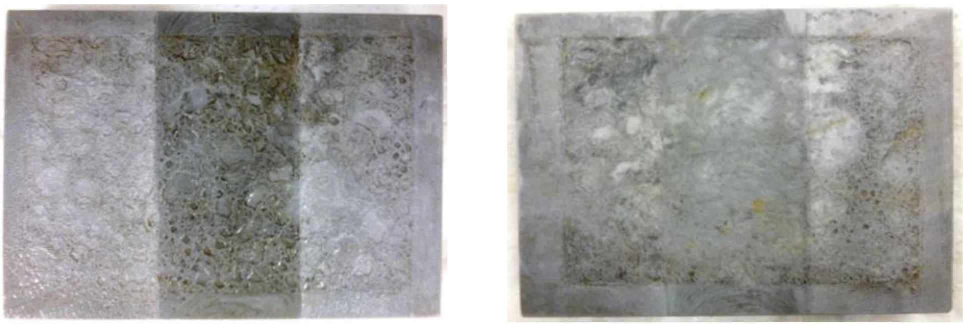

S40004 60 Cycles *S400012 60 Cycles*

S40003 75 Cycles *S400013 75 Cycles*

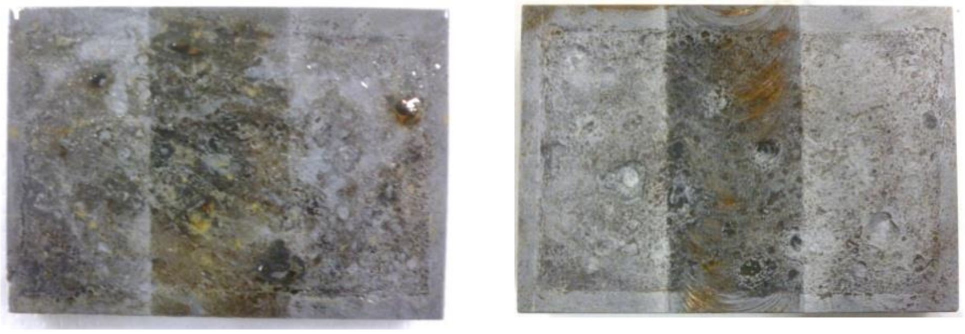

S40008 90 Cycles *S40006 90 Cycles*

Figure 4.31: Comparison of specimens (regular - interval) FSW for different exposure times, after the removal of corrosion products. The specimens of 90 cycles are all regular

From the observation of specimens, it is obvious that the phenomenon evolves on the surface of the specimen in a manner similar to that specimen without welding. Specifically, we can make the following observations:

- In the specimens that have remained in the chamber for long times, the emergence of large craters and cavities it is seen for both in the weld metal and the base metal of the specimen.
- The welded are of the specimens appears to be darker than the parent metal. This phenomenon can be attributed to the FSW process.

4.3.3.5. Observations on the surface of the similar S690 FCAW welded specimens after the chamber

It is observed that the development of corrosion on the specimens of S690 FCAW specimens follows the same pattern as in the AH36 FSW specimens (***Figure 4.32***). The images of specimens, are listed below, as they came out of the salt spray chamber (***Figure 4.32***).

Regular **Interval**

IIA2 15 Cycles

IIIA2 15 Cycles

VA2 30 Cycles

IIIB2 30 Cycles

IA2 45 Cycles

IIIC2 45 Cycles

IC2 60 Cycles

IVA2 60 Cycles

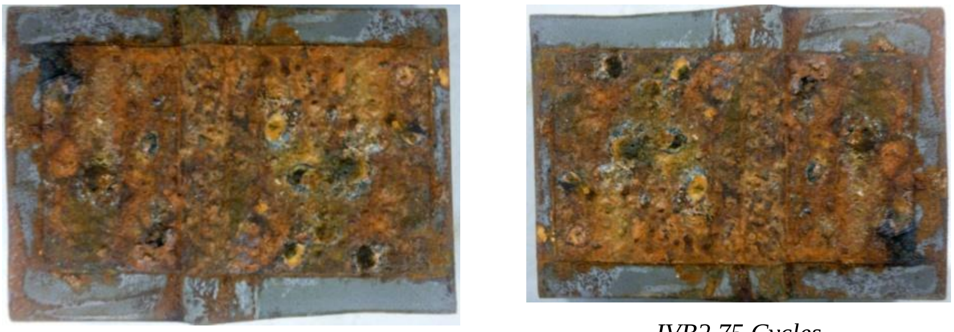

IIC2 75 Cycles

IVB2 75 Cycles

IB2 90 Cycles

IIB2 90 Cycles

Figure 4.32: Comparison of corroded surfaces of FSW specimens regular - interval, for different exposure times (15,30,45,60,75,90 cycles).

4.3.3.6 Observations for the surface of the similar S690 FCAW welded specimens after the removal of the corrosion products

Below are represented the specimens of S690 FCAW after the removal of the corrosion products (***Figure 4.33***):

Regular **Interval**

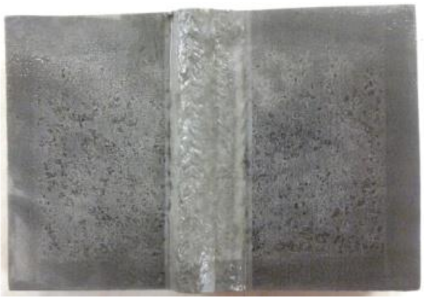

IIA2 15 Cycles

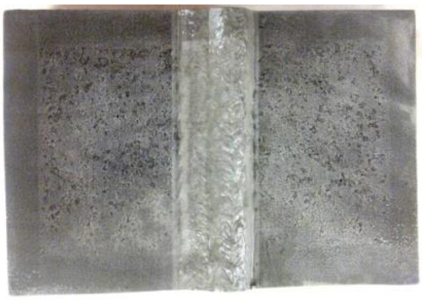

IIIA2 15 Cycles

VA2 30 Cycles

IIIB2 30 Cycles

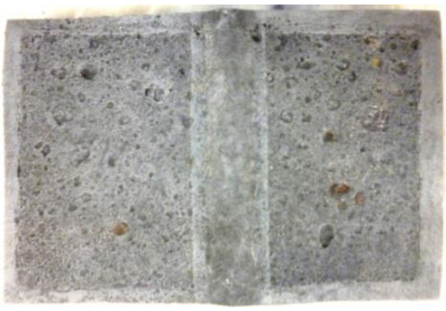

IA2 45 Cycles

IIIC2 45 Cycles

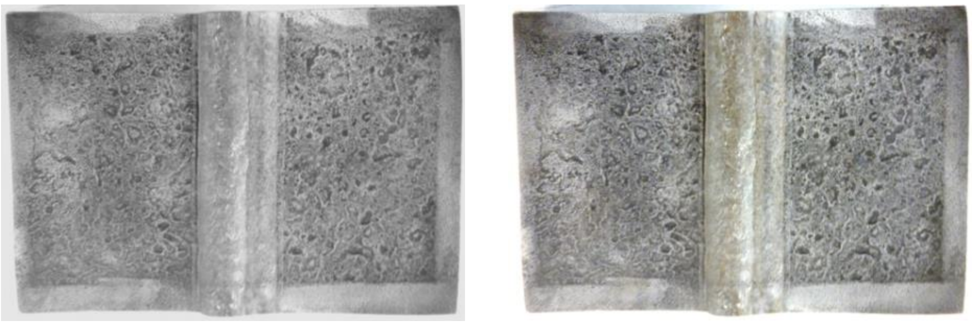

IC2 60 Cycle *IVA2 60 Cycles*

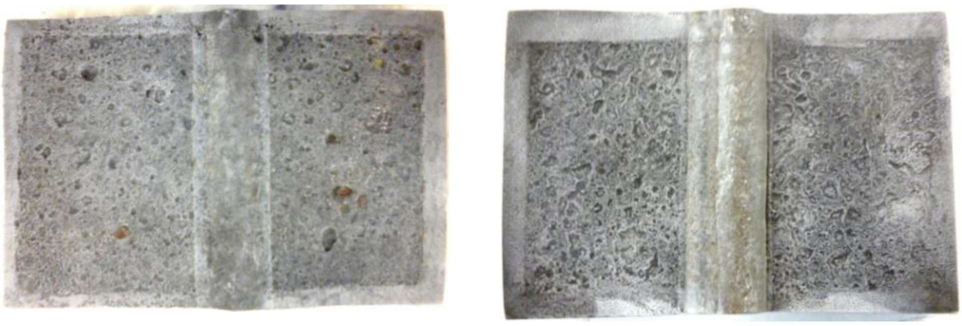

IIC2 75 Cycles *IVB2 75 Cycles*

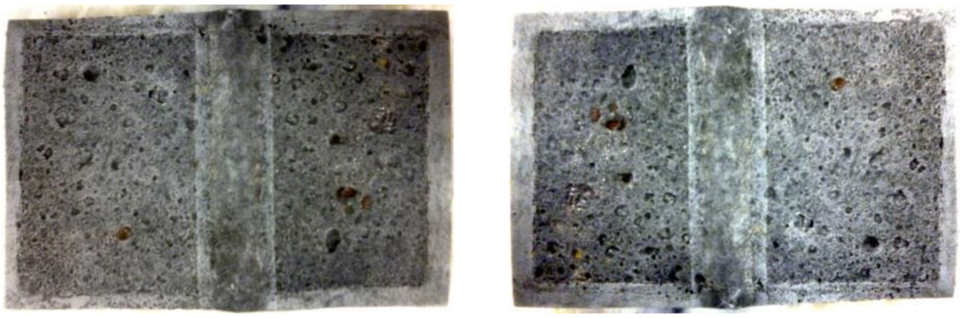

IB2 90 Cycles *IIB2 90 Cycles*

Figure 4.33: Comparison of specimens (regular - interval) FCAW for different exposure times, after the removal of corrosion products. The specimens of 90 cycles are all regular.

It is observed that the development of corrosion on the specimens of S690 FCAW specimens follows the same pattern as in the AH36 FSW specimens. The only difference that it is noteworthy is that the corrosion on welding is not so equable as it is in base metal and in FSW. In fact, the seam of the weld, appears to be more resistant to corrosion than the parent metal, without exhibiting obvious corrosion defects even after 75 cycles of corrosion in the salt spray chamber.

4.4. Structured white light 3D scanning

In the present thesis the mapping of the corroded surface was attempted, for three kinds of specimens, in total six (6) specimens, after the removal of the corrosion products:

- Parent Metal S690 specimens: IA1, regular, 15 days, IB1, regular, 30 days
- Similar AH36 Friction Stir Welded specimens: S40009, regular, 15 days, S40008, regular, 30 days
- Similar S690 FCA Welded specimens: specimen IA2, regular, 15 days, IB2, regular, 30 days

The sandblasted specimens were scanned, employing white light 3D scanning, before they were placed in the salt spray chamber, and after the removal of the corrosion products. The aim is to compare the relief of the surfaces before and after the corrosion process. The scanner scanned each specimen separately, creating a unique grid for every specimen. Moreover, in order to exploit the abilities of the method, two different soft wares were employed foe the process of the grids acquired: The CloudCompare and Rapidform XOR3.

The results are presented in the following paragraphs.

4.4.1. Grids acquired by Rapidform XOR3 and CloudCompare software, for the corroded surface of the specimens

The aim of the scanning was to examine the relief of the corroded surface, and to monitor, if possible, the depth of some of the pits, compared to the initial surface relief.

The grids, by Rapidform XOR3, of S690 parent metal, after 15 days of exposure reveal, that the maximum depth of the pits is identified, noticed with orange color, and is measured up to 0.1513 mm ***(Figure 4.34b).*** The grid acquired with cloud compare software shows that a general diminuition of the surface is detected, colored in light green and yellow color. According to the legend 0.15mm diminution is measured ***(Figure 4.34 c).*** The results of the two different softwares are in agreement.

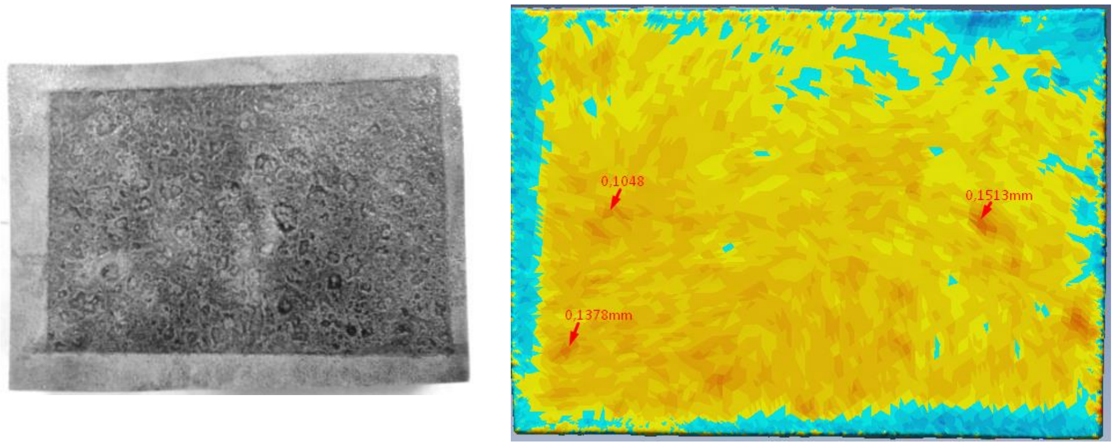

a. Parent Metal, S690, IAI, regular, 15 days

b. Grid acquired with Rapidform XOR3

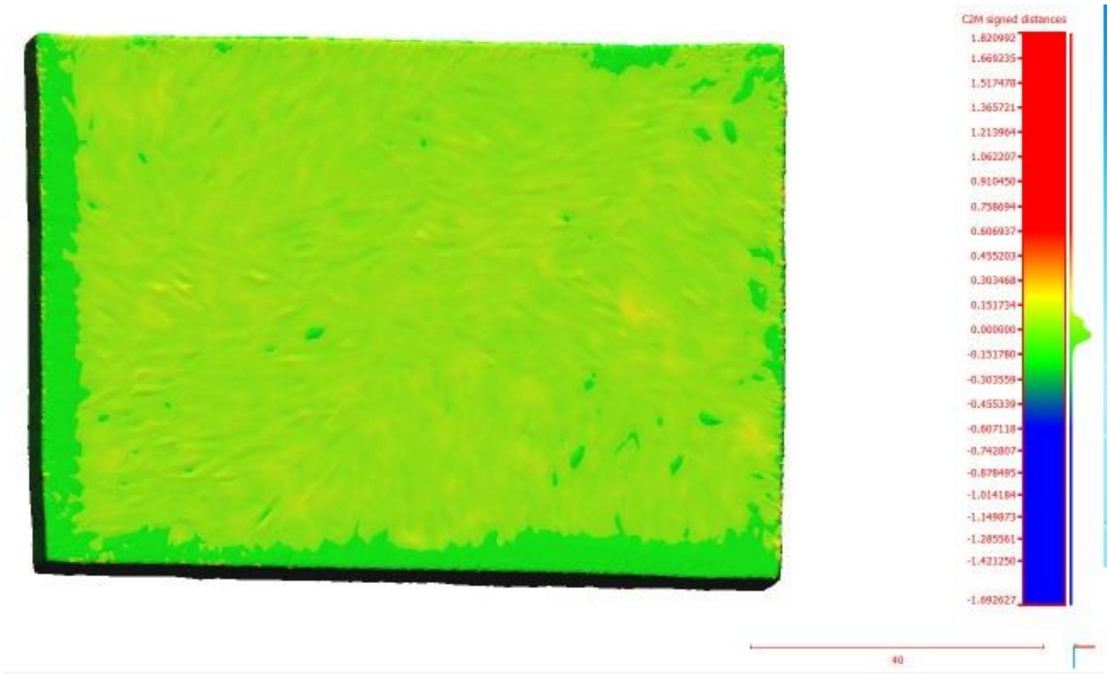

c. Grid acquired with CloudCompare XOR3

Figure 4.34: Grids for corroded surface of Parent Metal S690, IAI, after 15 days of exposure.

After 30 days of exposure, for S690 parent metal specimen, deeper pits are macroscopically noticed (Fig. 4.35 a). The grid by Rapidform XOR3 reveals that some pits of 0.4mm are recognized and one pit is measured up to 0.5114mm depth (***Figure 4.35b***). The same results are obtained from Cloudcompare software, presented with light red – orange color, indicating depth around 0.45mm (***Figure 4.35c***).

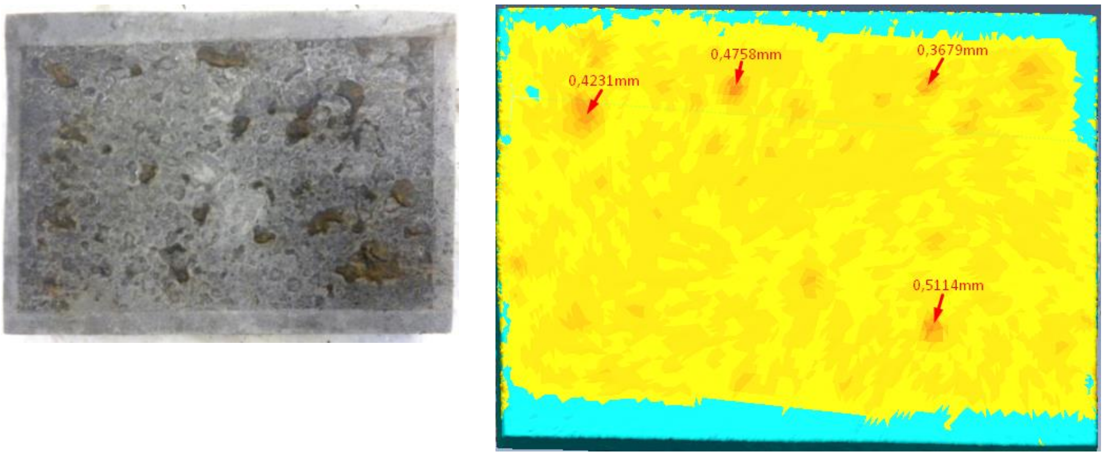

a.Parent Metal, S690, IBI, regular, 30 days

b. Grid acquired with Rapidform XOR3

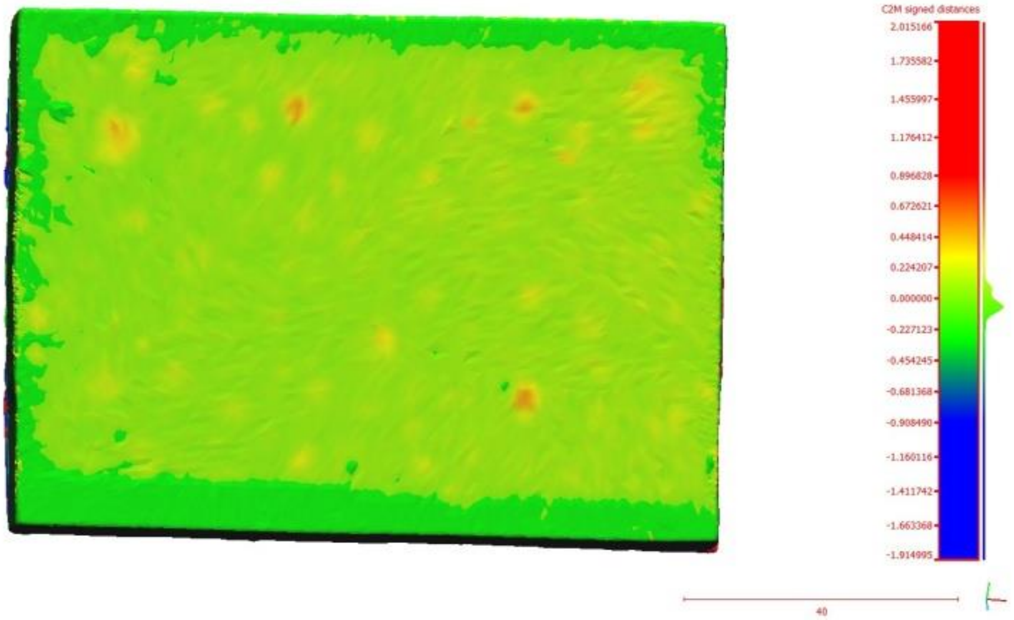

c. Grid acquired with CloudCompare

Figure 4.35: Grids for corroded surface of Parent Metal S690, IBI, regular, after 30 days of exposure

For FCAW S690-S690 welded specimen, only small pits are detected on the weld seam (***Figure 4.36***). However, the pits detected rise up to 0.5944mm (by Rapidform XOR3) (***Figure 4.35b***). Similar value for the same spot is measured by CloudCompare software, indicated with dark red color (***Figure 4.35c***). Both methods present the same patter for the relief of the corroded surface. It should be noticed that the deeper values detected after 15 days exposure for FCAW S690-S690 welded specimen is higher than these recorded for the parent metal, for the same exposure time (***see Figure 4.34***).

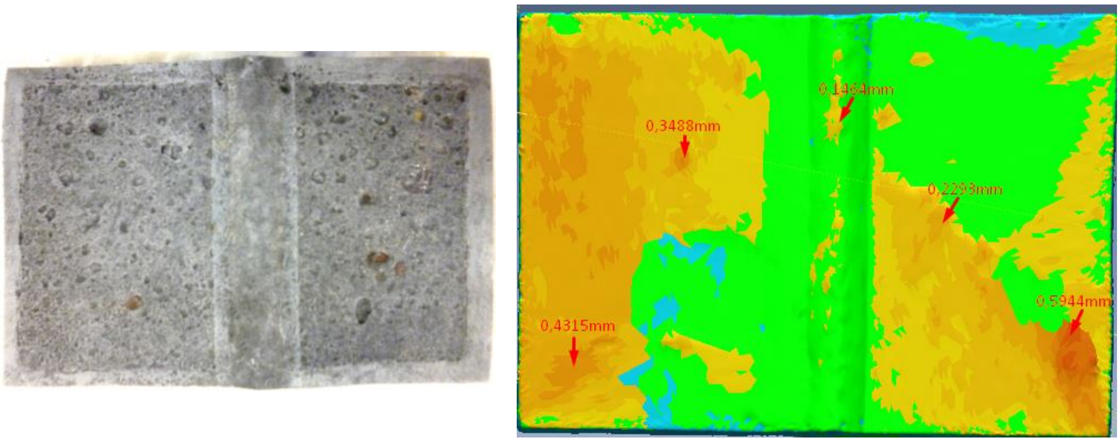

a.FCAW, S690, IA2, regular, 15 days *b. Grid acquired with Rapidform XOR3*

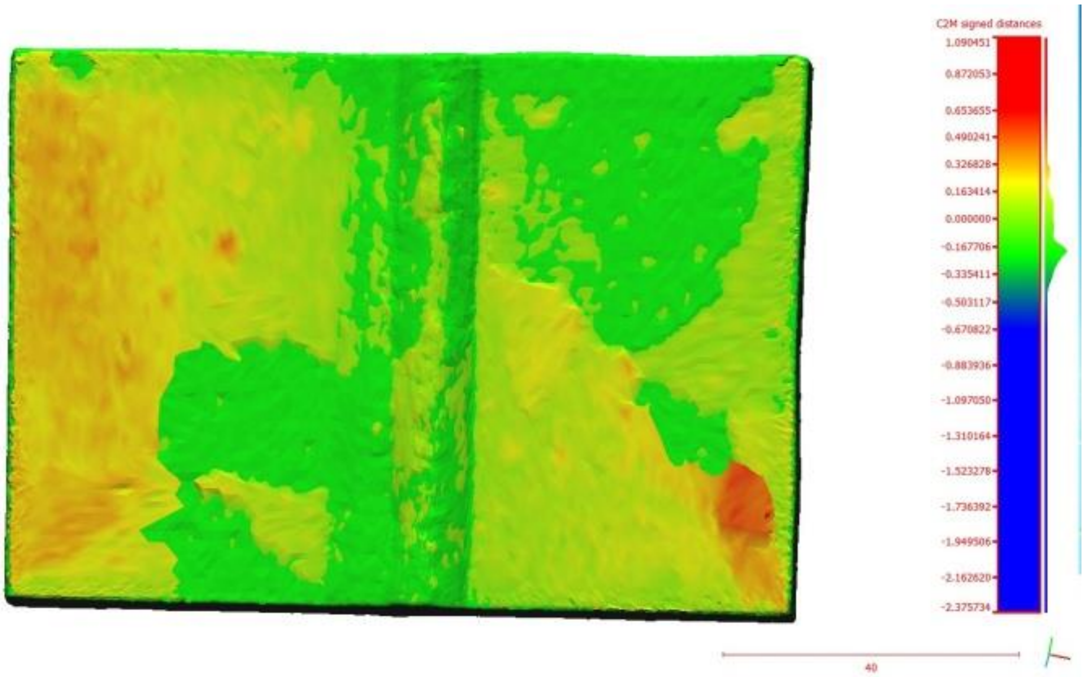

c. Grid acquired with CloudCompare

Figure 4.36: Grids for corroded surface of FCAW S690, IA2, regular, after 15 days of exposure

After 30 days of exposure, still no significant pits are detected on the weld seam, for FCAW S690 specimen ***(Figure 4.37).*** However now a general diminuition of the surface is revealed, more abundant are deep pits and value up to 0.6704mm is recorded ***(Figure 4.37b)***. The same pattern for the relief of the surface is indicated by CloudCompare image ***(Figure 4.37c)***. (b and c images are upside down)

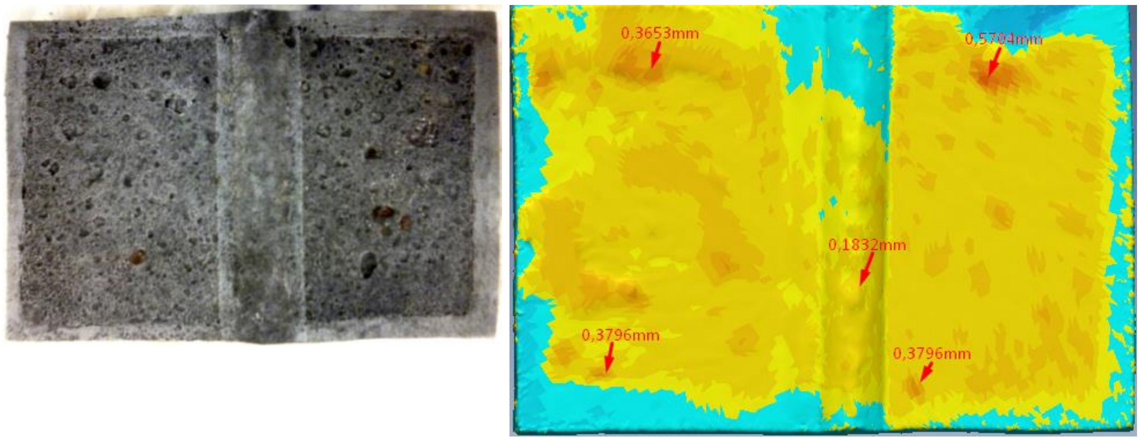

a.FCAW, S690, IB2, regular, 30 days

b. Grid acquired with Rapidform XOR3

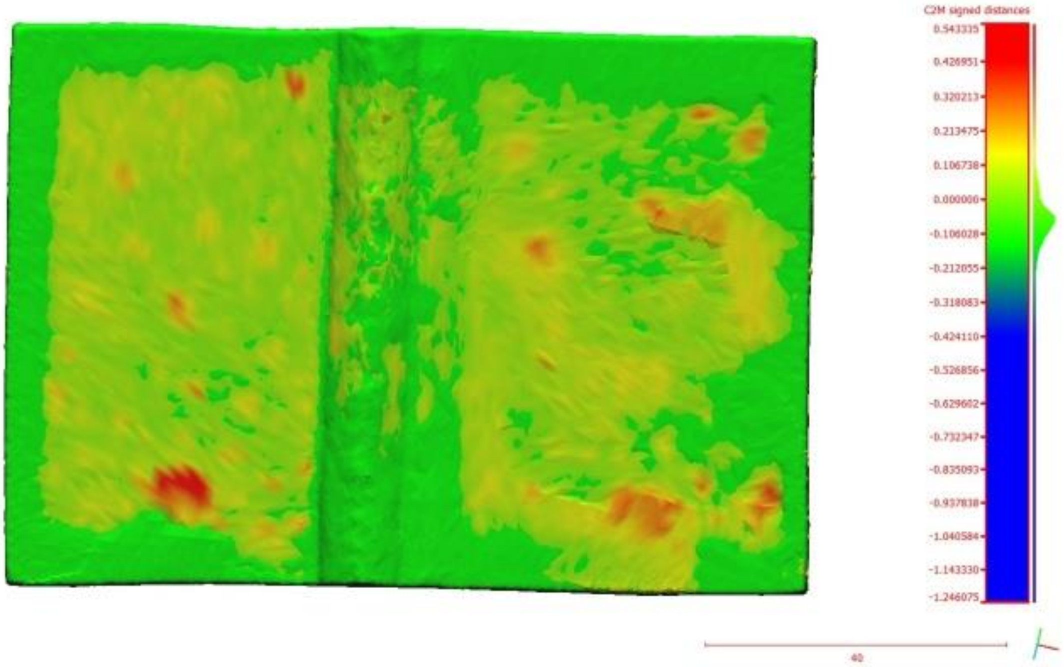

c. Grid acquired with CloudCompare

Figure 4.37: Grids for corroded surface of FCAW S690, IB2, regular, after 30 days of exposure

Friction Stir Welded AH36-AH36 specimen, after 15 days of exposure, show several pits of around 0.15-0.20 mm, concentrated mainly in one side of the weld ***(Figure 4.38).*** One pit of 0.4mm is also noticed ***(Figure 4.38b)***.

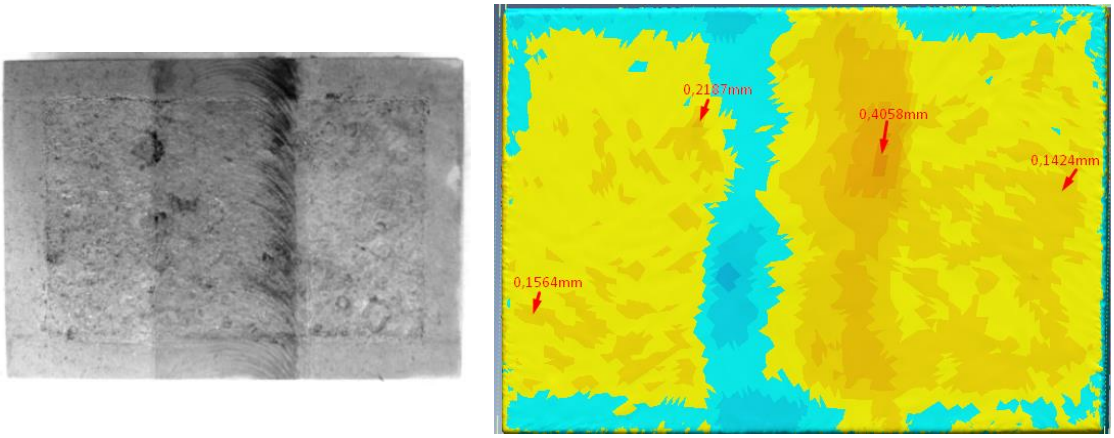

a. AH36 FSW, S40009, 15 days

b. Grid acquired with Rapidform XOR3

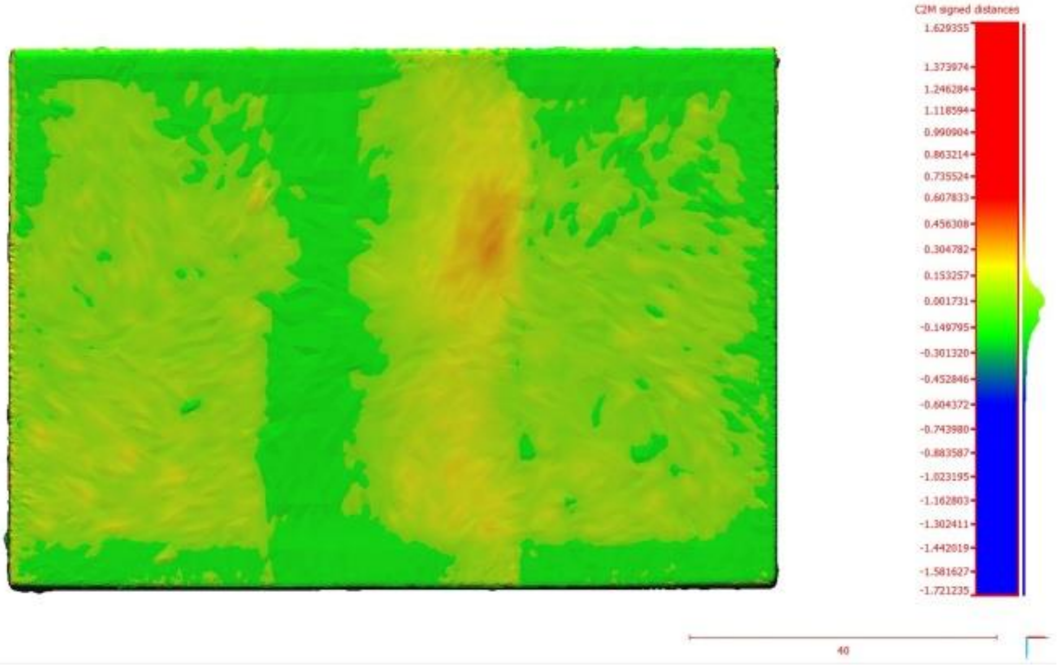

c. Grid acquired with CloudCompare XOR3

Figure 4.38: Grids for corroded surface of FSW AH36, S40009, regular, after 15 days of exposure

However, after 30 days of exposure the pit depth is increased and several areas of pitting around 0.3-0.4mm is noticed ***(Figure 4.39)***. The pitting is spread in the whole area of the specimen ***(Figure 4.39)***.

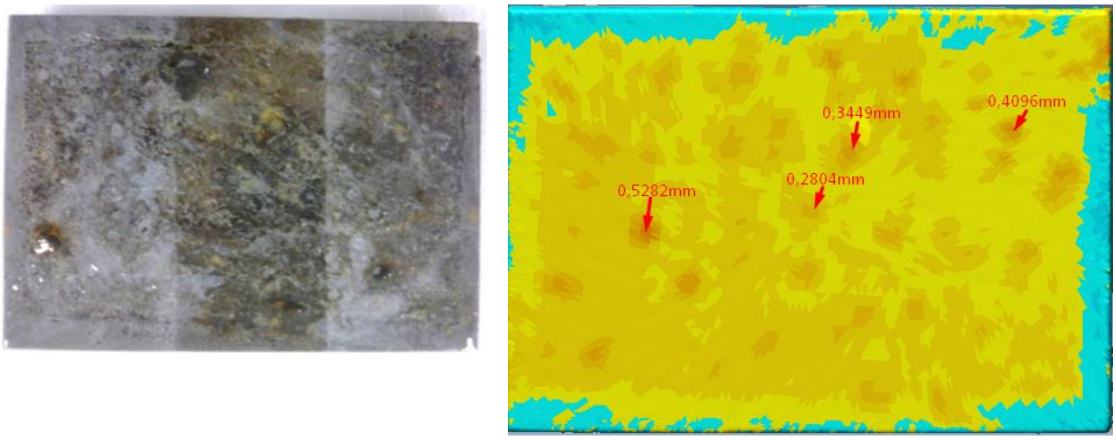

a. AH36 FSW, S40008, 30 days *b. Grid acquired with Rapidform XOR3*

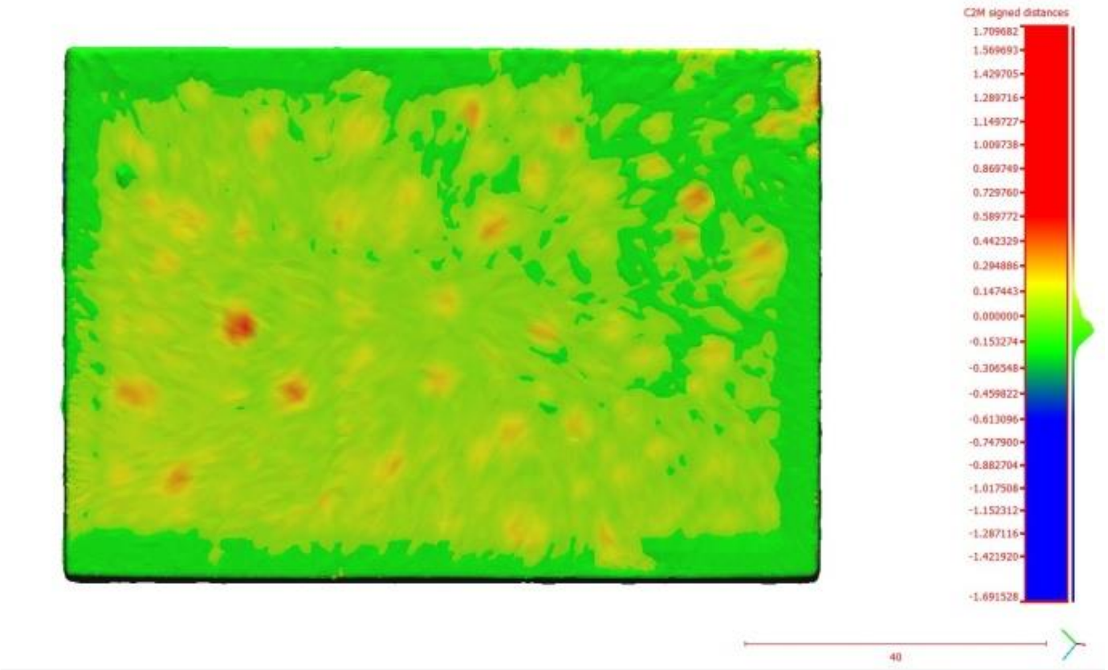

c. Grid acquired with CloudCompare

Figure 4.39 Grids for corroded surface of FSW AH36, S40008 regular, after 30 days of exposure

4.5. Electrochemical measurements for the corrosion study

In the experiments performed, in order to acquire the polarization curves, the same procedure was followed for all the experiments, in order to obtain comparable results.

Initially, the metal specimen is adapted in the cell, which is filled with the aqueous solution of NaCl 3.5% w / w. Then, the reference electrode is placed, Saturated Calomel Electrode.

The next step is to stabilize the open circuit potential of specimens in value of the corrosion potential of these (E_{oc}). Monitoring of Potential is obtain using the Virtual Potentiostat program. The value of the potential is observed until it is stabilized and does not change more than 1mV over 3 minutes time. This is necessary, since the application of electrochemical techniques requires the value of the potential of the open circuit to be stabilized. The next step is to start the application of electrochemical methods, which have been selected, i.e. linear polarization, Electrochemical Impedance Spectroscopy (EIS) method and Tafel curves, in this sequence, since the first two methods is non-destructive, while Tafel curves is a destructive method. The curves presented in the following paragraphs, are the best acquired, meaning with the less noise, after several repetitions of the experiment. All measurements were performed at ambient conditions in aerated NaCl 3.5% w/w solution.

4.5.1. Linear Polarization

After the stabilization of the potential, Versastat has to be activated. The polarization potential range is set to 20 mV. The metal electrode is polarized initially cathodic (-20mV vs E_{oc}) and then anodic (+ 20mV vs E_{oc}). Other parameters, which are defined are: the scan rate (scan rate = 0,1mV), and the selected saturated calomel electrode (SCE) as reference electrode.

4.5.1.1. AH36 Parent Metal and AH36 similar Friction Stir Welding

Seven consecutive repetitions were made for Linear Polarization for both specimens: AH36 Parent Metal and AH36 - AH36 Friction Stir Welding. The graphs of the best measurements are shown below in ***Figure 4.40 & 4.41***:

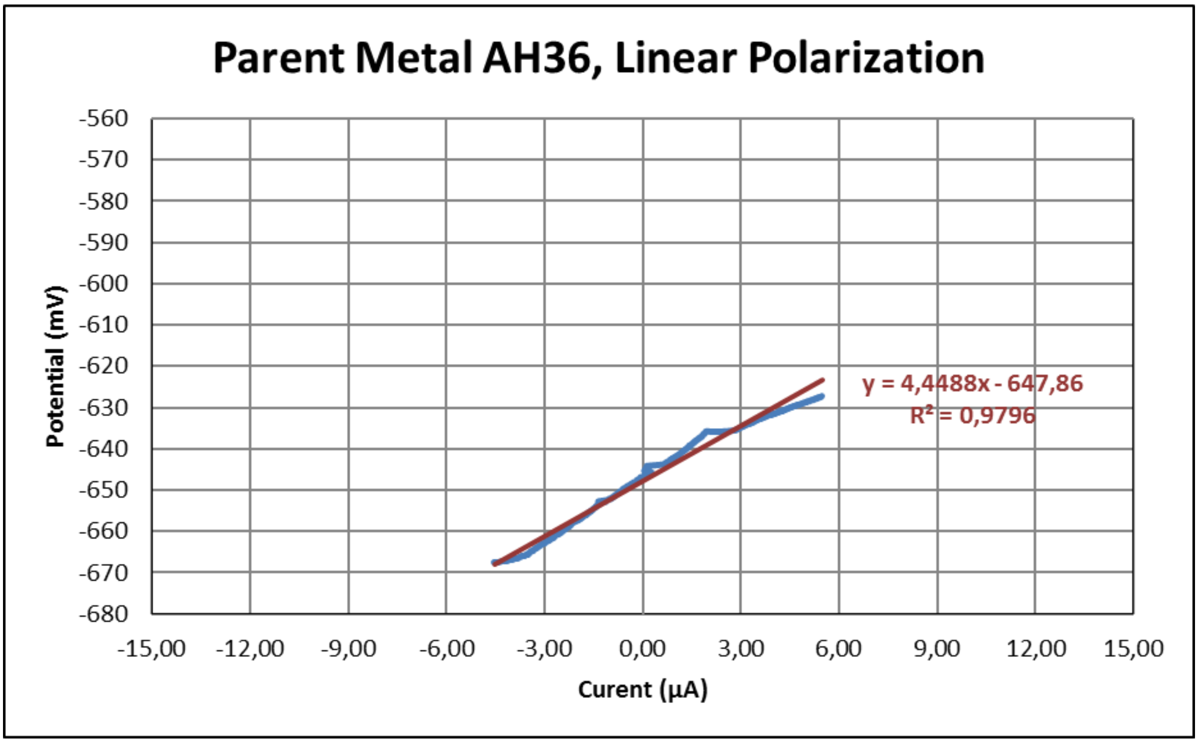

Figure 4.40: Current(μA) of Parent Metal AH36 vs Potential (mV)

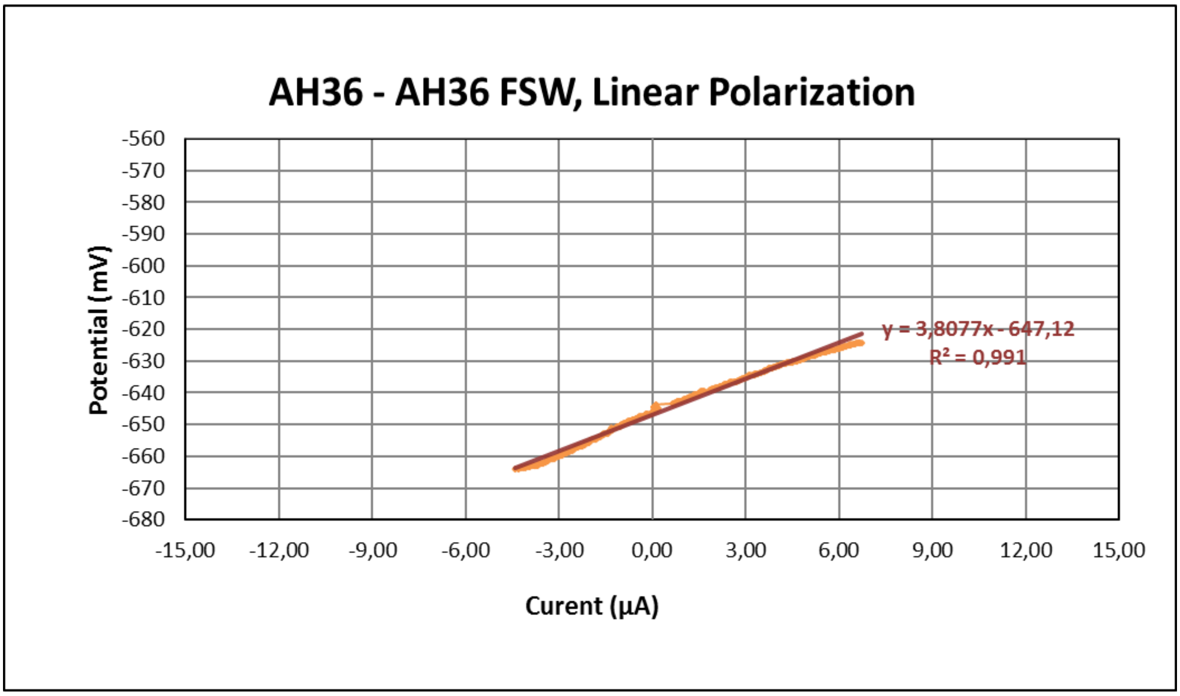

Figure 4.41: Current (μA) of AH36 - AH36 FSW vs Potential (mV)

4.5.1.2. S690 Parent Metal and similar S690 FCAW

Similar to previous measurements, the graphs of the best measurements for S690 Parent Metal and S690 - S690 FCAW are shown below in ***Figures 4.42 & 4.43***:

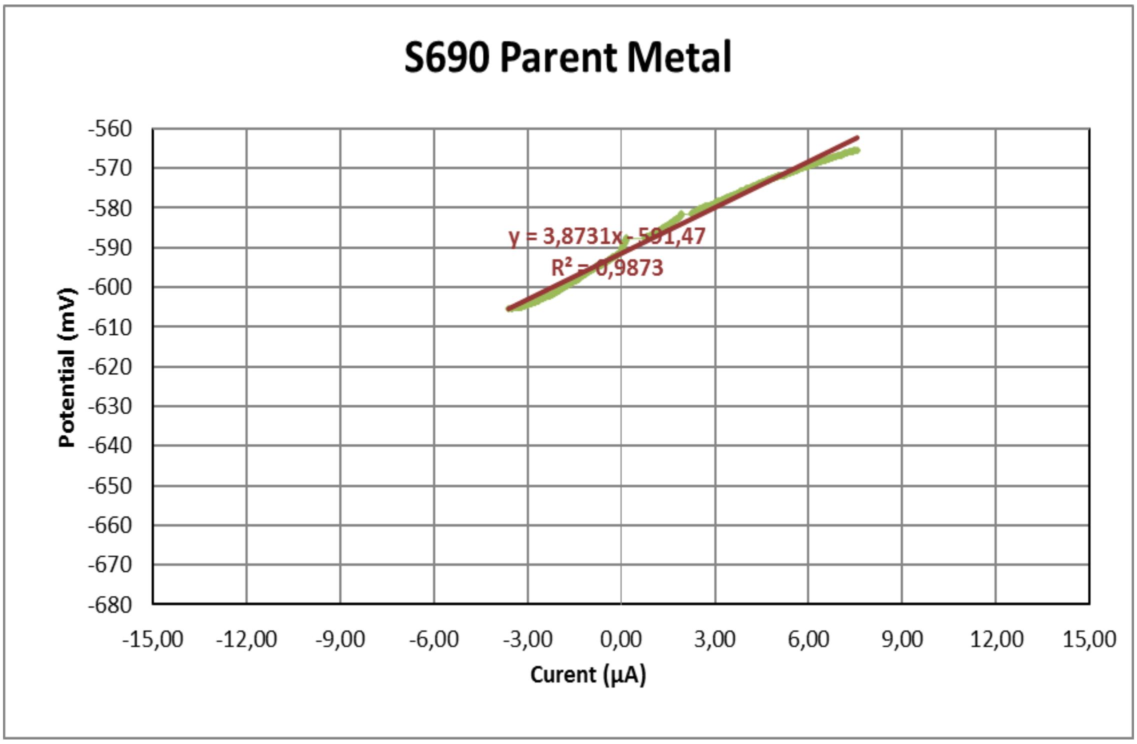

Figure 4.42: Current (μA) of S690 Parent Metal vs Potential (mV)

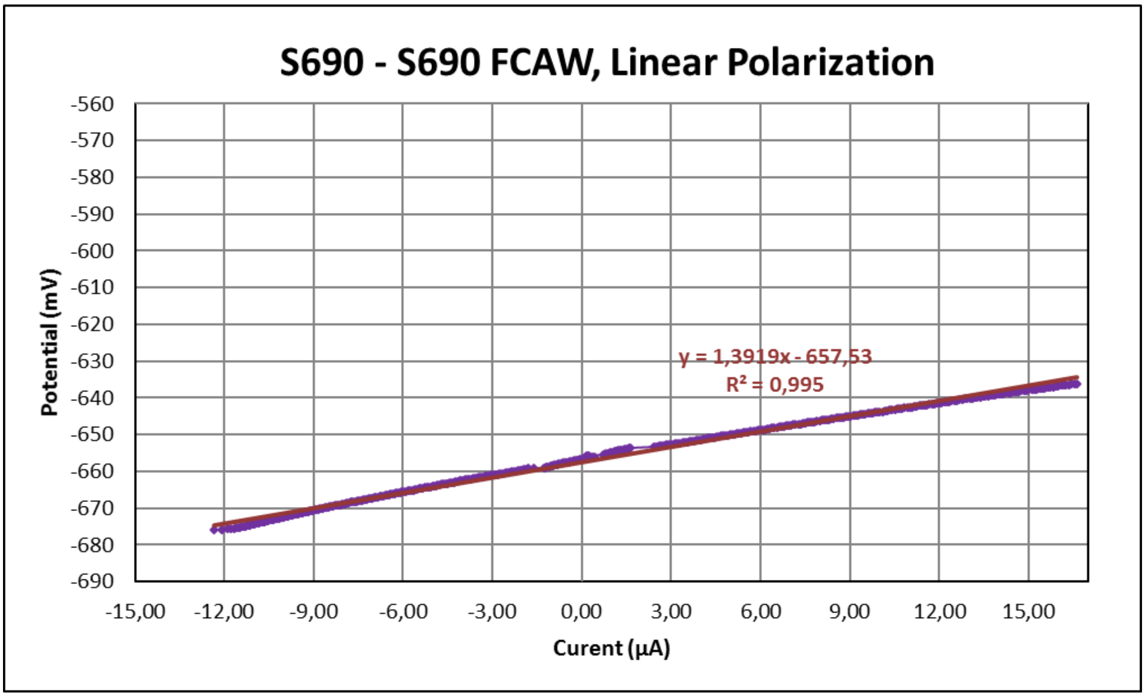

Figure 4.43: Current (μA) of S690 FCAW vs Potential (mV)

4.5.1.3. Comparison between Parent Metals (S690 & AH36) and their similar welding (S690 FCAW, AH36 FSW)

The Figures below (***Figures 4.44-46***) show the Comparison between Parent Metals (S690 & AH36) and their similar welding (S690 FCAW, AH36 FSW):

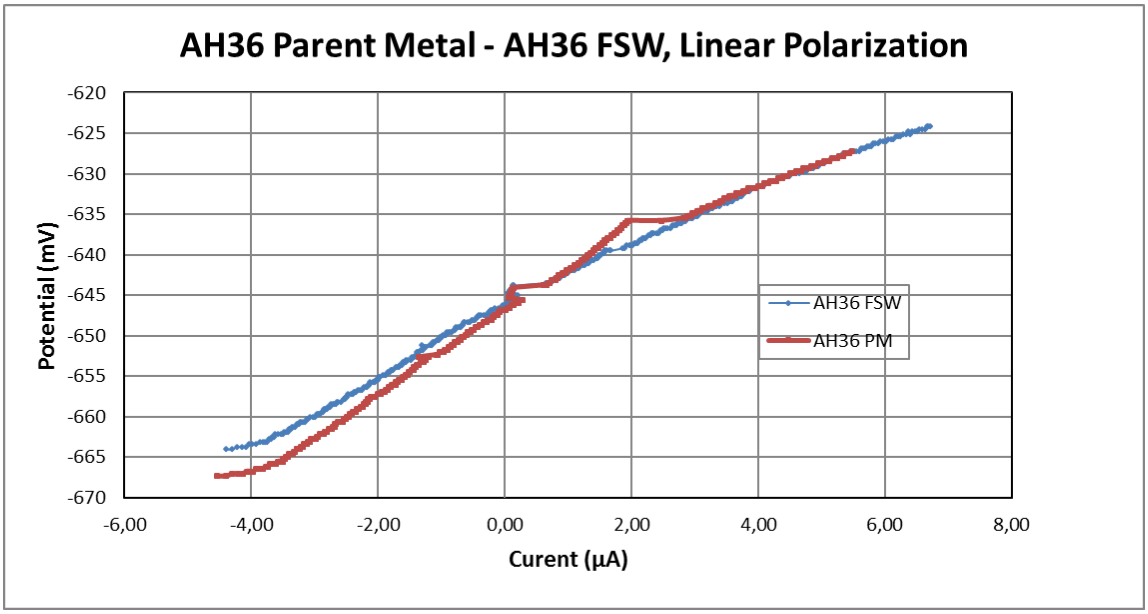

Figure 4.44: Current (μA) of AH36 Parent Metal - AH36 FSW vs Potential (mV)

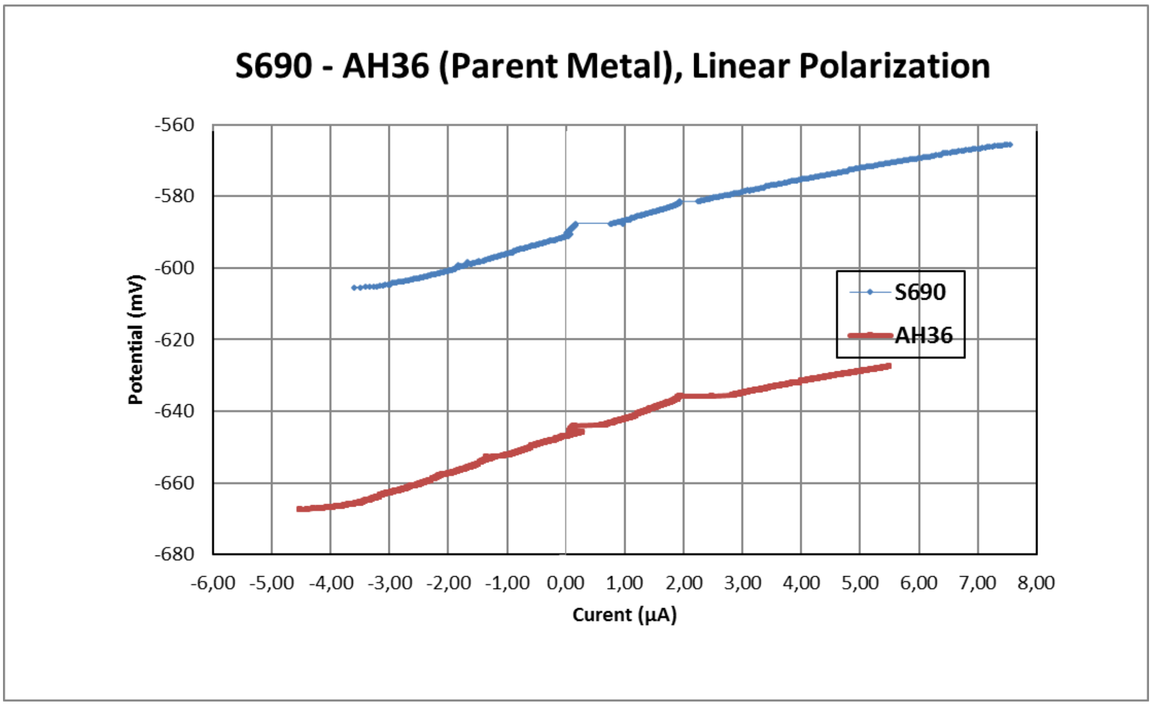

Figure 4.45: Current (μA) of AH36 Parent Metal - S690 Parent Metal vs Potential (mV)

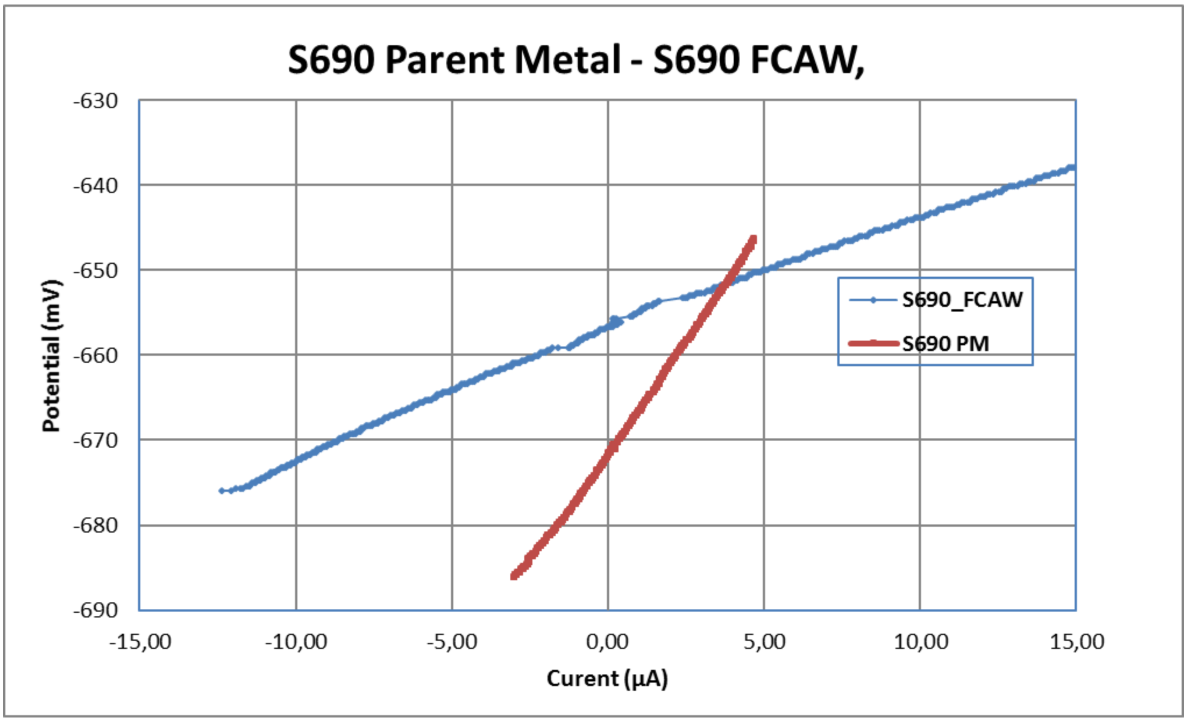

Figure 4.46: Current (μA) of AH36 Parent Metal - S690 Parent Metal vs Potential (mV)

4.5.2. Tafel method

Tafel extrapolation method is a method in which the specimen is polarized ±250mV vs. E_{oc}. For the present Potentiostat, the sweep starts to polarize cathodically and continues to the anodic part of the curves. The experiments were performed employing Saturated Calomel as reference electrode and 3.5% NaCl, aerated electrolyte at ambient conditions. The Tafel polarization method is a destructive electrochemical method, thus the surface of the specimen cannot be used for another experiment, unless it is polished again. Several experiments were performed, especially for the parent metals, in order to acquire the representative curves without noise. In the following paragraphs the most representative curves are presented.

4.5.2.1. Parent Metal AH36 and similar AH36-AH36 Friction Stir Weld

Two repetitions were made for Tafel method for both specimens: AH36 Parent Metal and AH36 - AH36 Friction Stir Welding. Tafel is a destructive method, so after the first measurement, the specimen had to be prepared again, for the next measurement. The graphs of the best measurements are shown below.

The Tafel curve for AH36 shows that the value for Ecorr is -600mV and for icorr 5μA/cm^2 ***(Figure 4.47).***

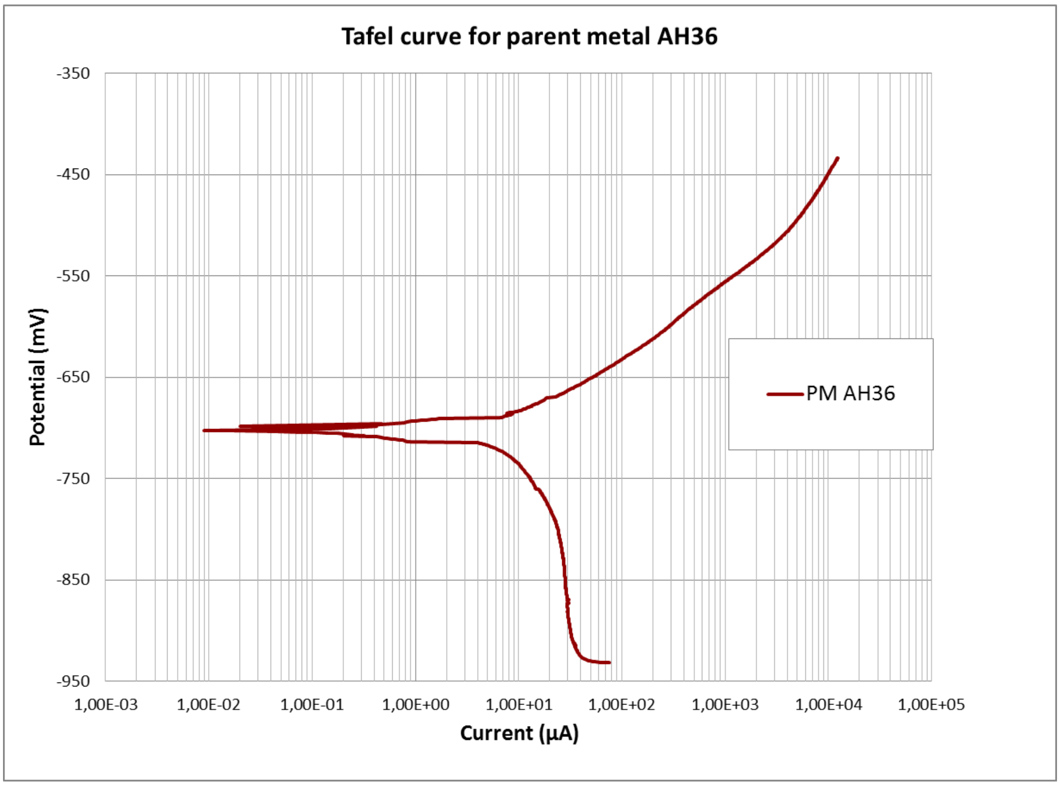

Figure 4.47: *Tafel curve of AH36 Parent Metal*

The Tafel curve for FSW similar AH36-AH36 shows that E_{corr} is -600mV, while i_{corr} is 2µA/cm^2 ***(Fig.4.48)***.

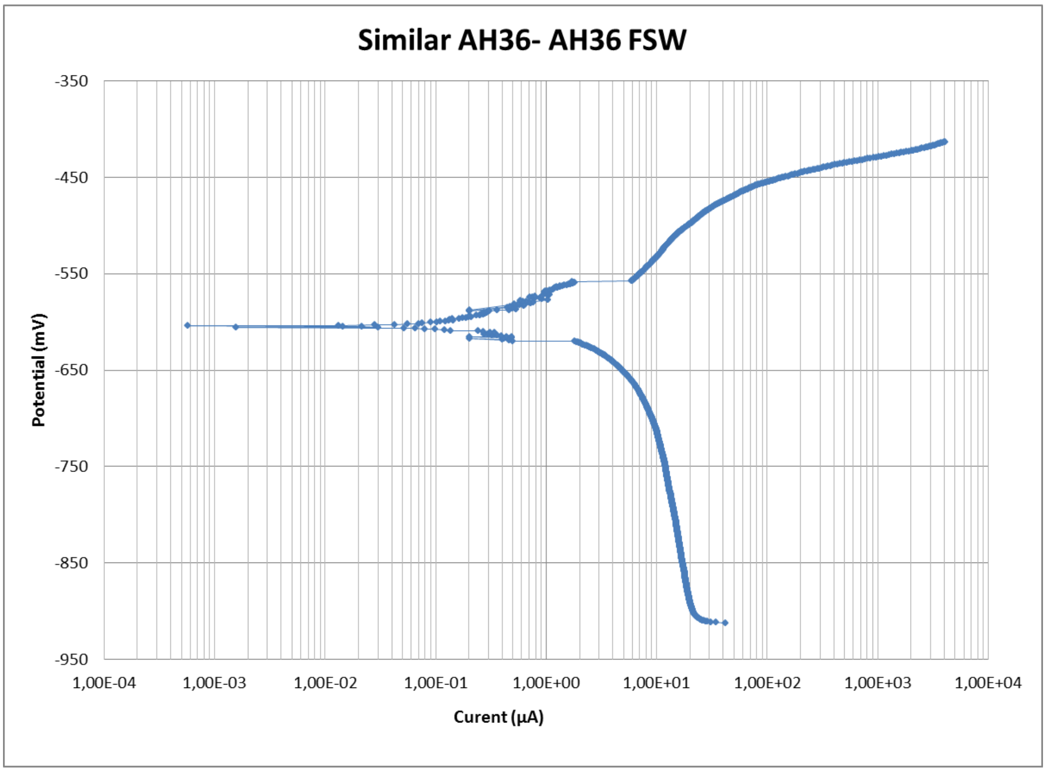

Figure 4.48: Current (µA) of AH36-AH36 FSW vs Potential (mV)

4.5.2.2. Parent Metal and similar S690 FCAW

Similar to previous measurements, the graphs of the best measurements for S690 Parent Metal and S690 - S690 FCAW are shown in the figures below. In Figure 4.49 the Tafel curve for parent metal S690 is presented. The Ecorr for S690 is measured at -670mV, while the icorr is equal to 10mA/cm^2 ***(Figure 4.49)***.

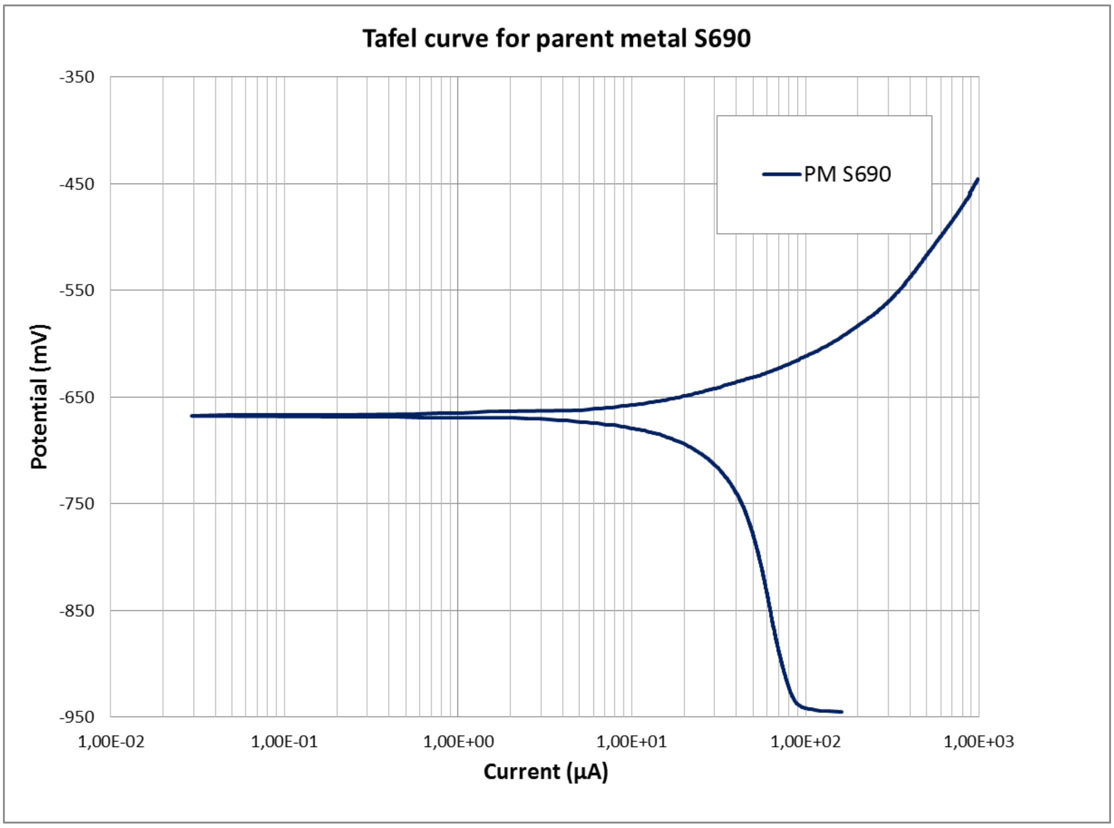

Figure 4.49. Tafel curve of S690 Parent Metal.

The Tafel curve for similar S690-S690 FCAW shows that the Ecorr is -680mV, while icorr is around 5μA/cm^2 ***(Figure4.50).***

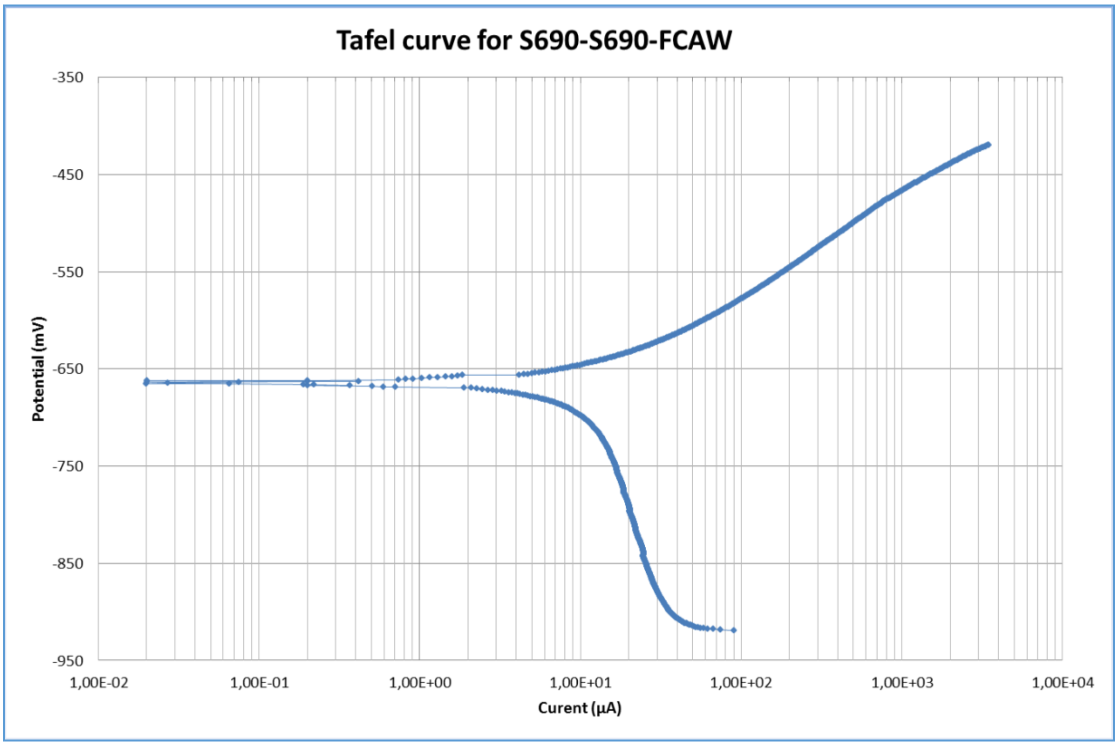

Figure 4.50: Tafel curve of S690 – S690 FSW.

4.5.2.3. Comparison between Parent Metals (S690 & AH36) and their similar welding (S690 FCAW, AH36 FSW)

In the following paragraphs the Tafel curves of both parent metals AH36, S690 are presented ***(Figure 4.51).*** The comparison reveals that Ecorr for AH36 is lower than S690, implying higher susceptibility to corrosion, while the icorr values are higher for S690 parent metal indicating higher corrosion rates ***(Figure 4.51)***.

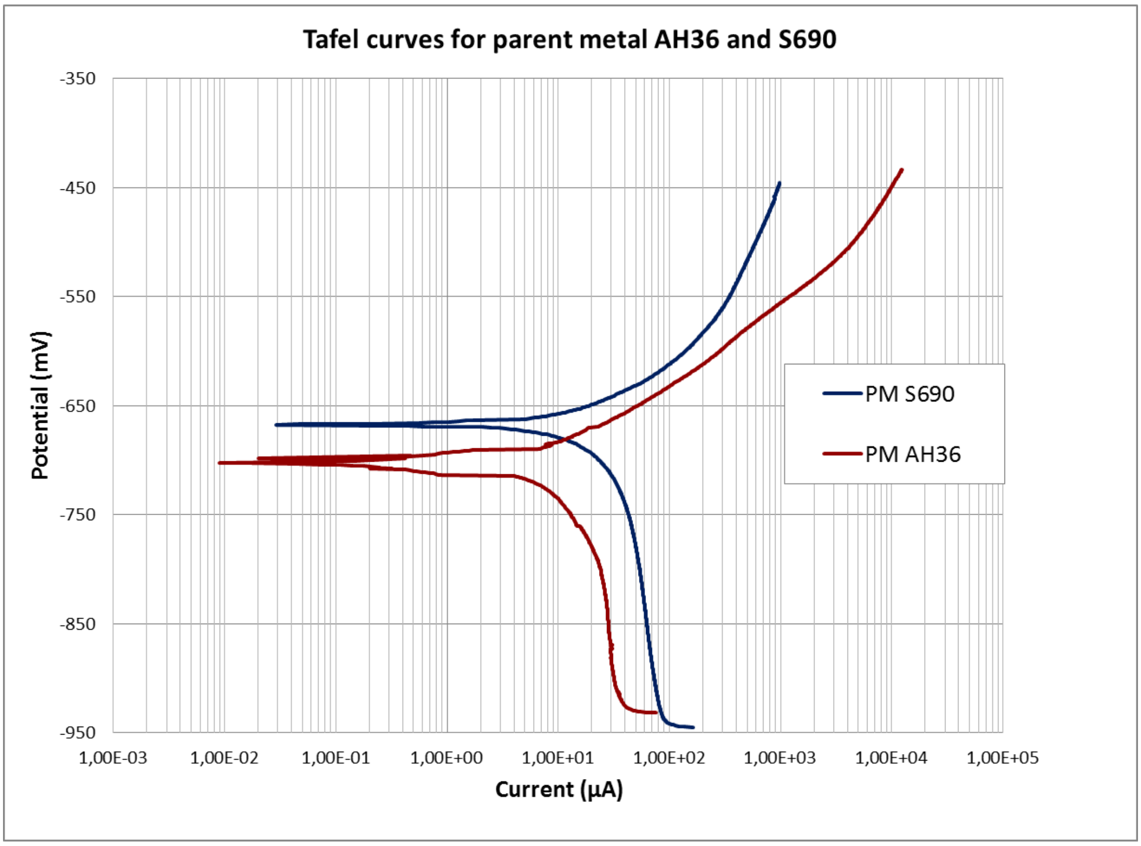

Figure 4.51: Tafel curves for both parent metals AH36, S690.

In the ***Figure 4.52*** the Tafel curves of both parent metals AH36 and FSW similar AH36-AH36 is presented. The comparison reveals that Ecorr for FSW AH36-AH36 is higher than parent metal AH36, implying lower susceptibility to corrosion, while the icorr values are higher for AH36 parent metal and FSW AH36-AH36 are rather similar (2μA/cm^2 and 5μA/cm^2 respectively) indicating similar corrosion rates ***(Figure 4.52)***.

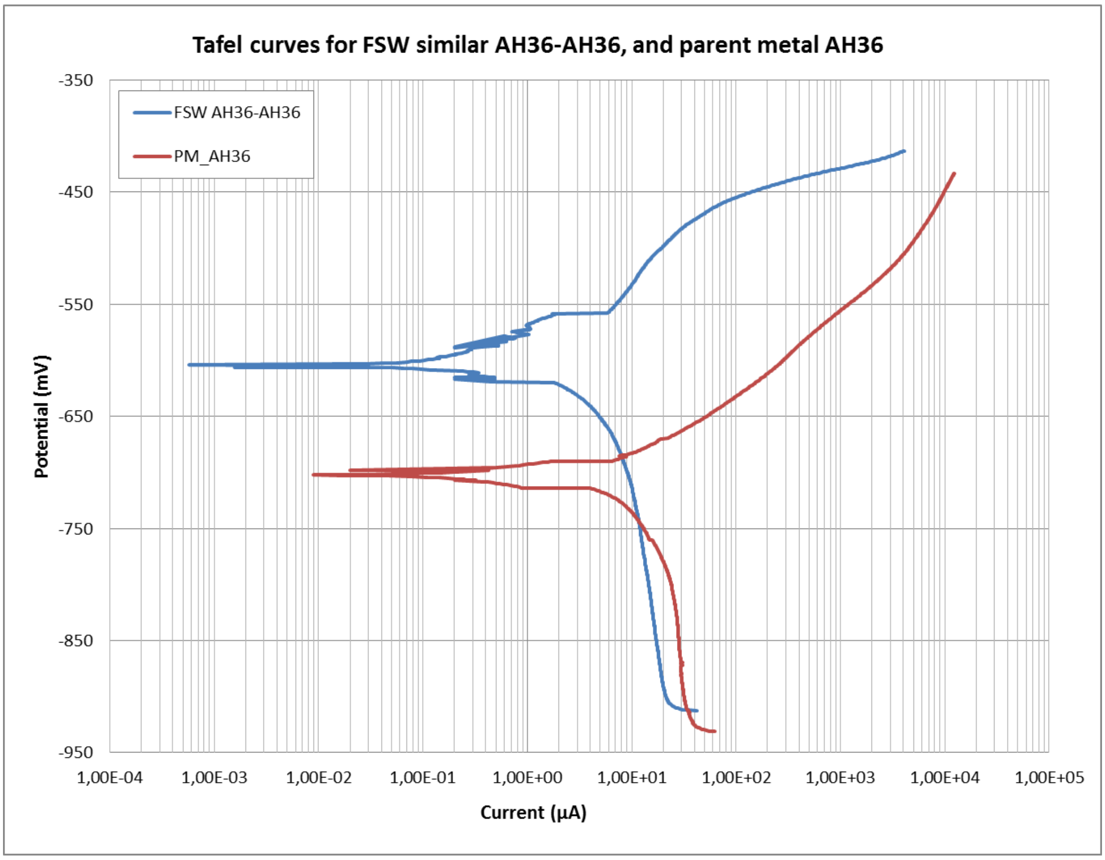

Figure 4.52: Tafel curves for similar FSW AH36-AH36 and parent metal AH36.

In the ***Figure 4.53*** the Tafel curves of both parent metals S690 and FCAW similar S690-S690 is presented. The comparison reveals that Ecorr that both parent metal S690 and FCAW S690-S690 present similar corrosion behavior concerning the Ecorr -670mV - -680mV, while the icorr values are double for parent metal S690, (5μA/cm^2 for FCAW and 10μA/cm^2 for parent metal) ***(Figure 4.53)***.

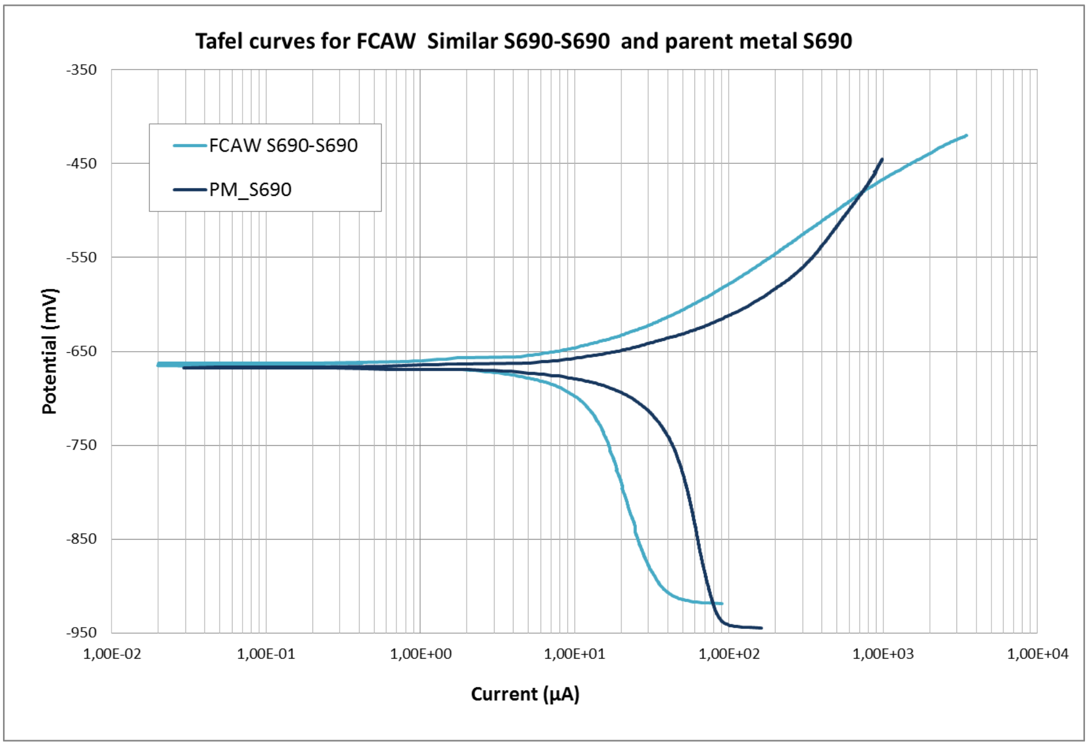

Figure 4.53: Tafel curves for similar FCAW S690-S690 and parent metal S690.

4.5.3. Impedance Spectroscopy (EIS)

Electrochemical impedance is measured by applying an AC potential to the electrochemical cell and then measuring the current through the cell. Assume that we apply a sinusoidal potential excitation. The response to this potential is an AC current signal. This current signal can be analyzed as a sum of sinusoidal functions (a Fourier series). In the following figures the Bode diagrams performed in the present thesis are presented.

In ***Figure 4.54*** the Bode curves for both parent metals are presented. The Rs of the solution is 5Ohms, while the Rp of both parent metals rise to 1000 Ohms, indicating similar Polarization Resistance for both metals.

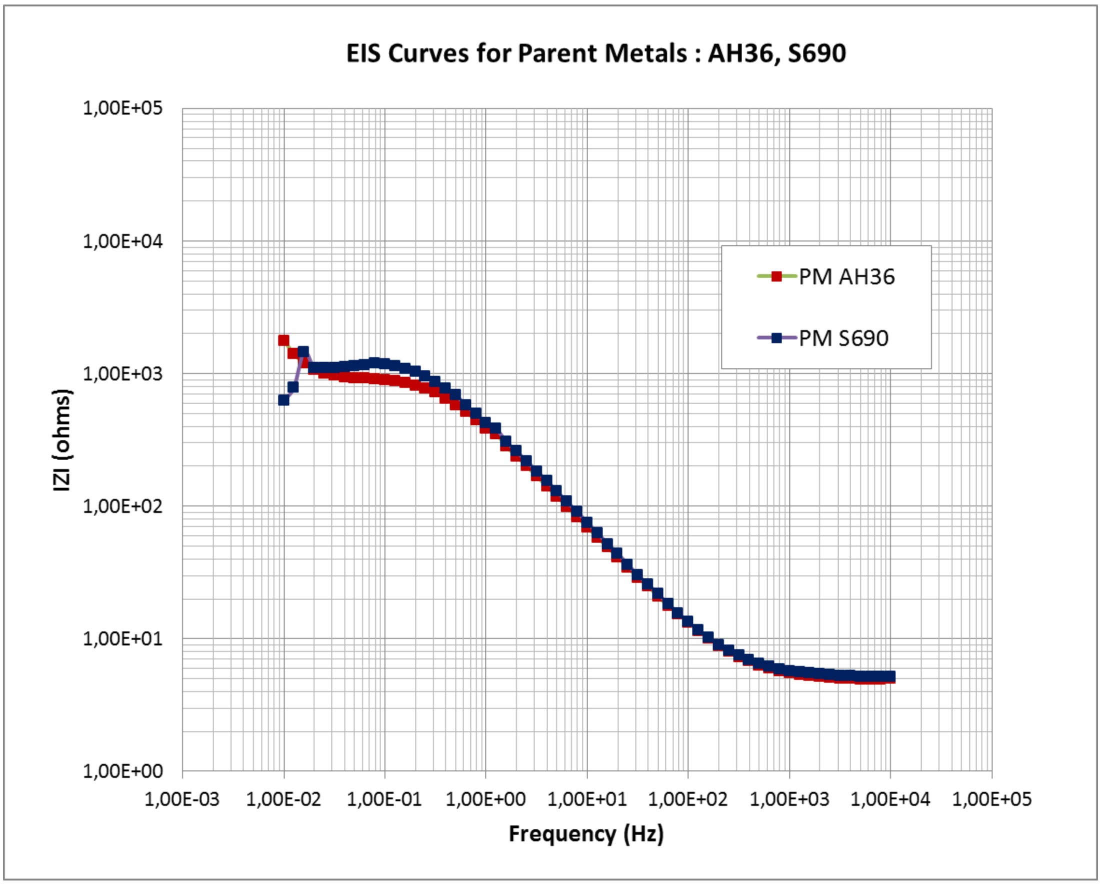

Figure 4.54: Bode diagram for parent metals AH36, S690

Figure 4.55 presents the Bode curves for parent AH36 and similar AH36-AH36 FSW. From the plot comes out that Rp for FSW AH36-AH36is higher for FSW, 10000 Ohms, while for Parent Metal AH36 is lower. These results show that Polarization Resistance for friction stir welded specimen is higher indicating lower susceptibility to corrosion.

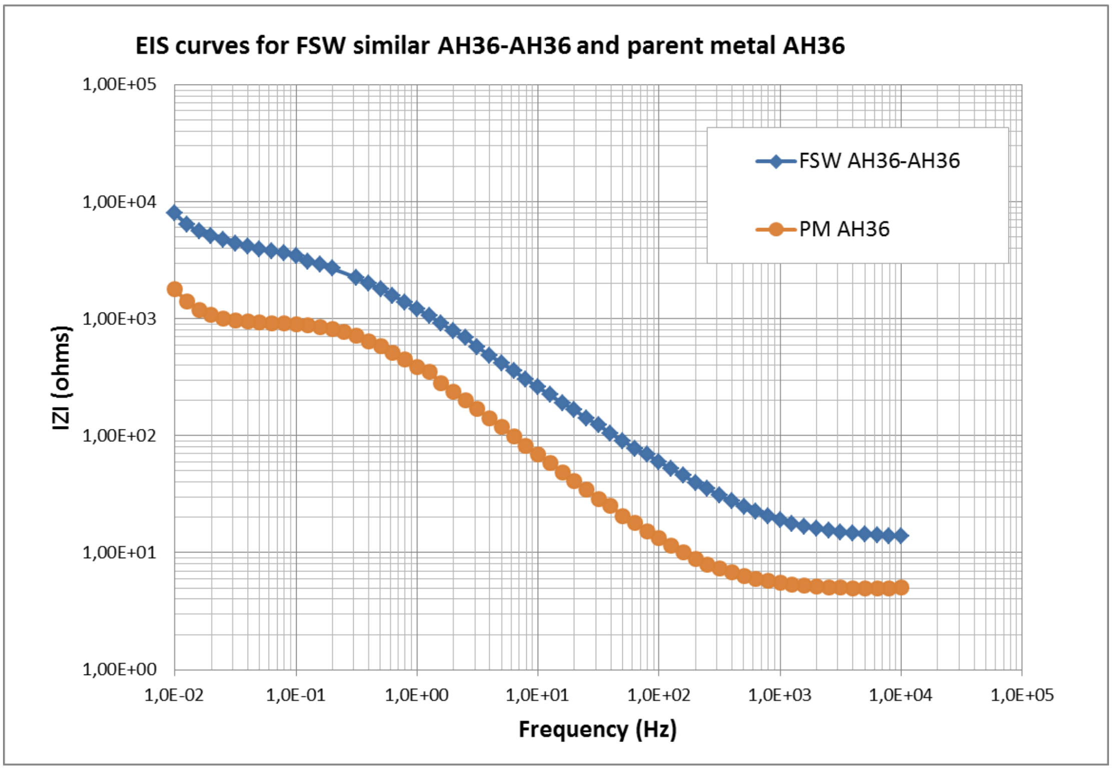

Figure 4.55: Bode diagram for parent metal AH36 and Friction Stir Weld AH36-AH36.

The Bode plots for S690 parent metal and FCAW S690-S690, reveal that the welded specimen presents higher Polarization Resistance 2000 Ohms than the parent metal, showing higher resistance to corrosion than the parent metal (***Figure 4.56***).

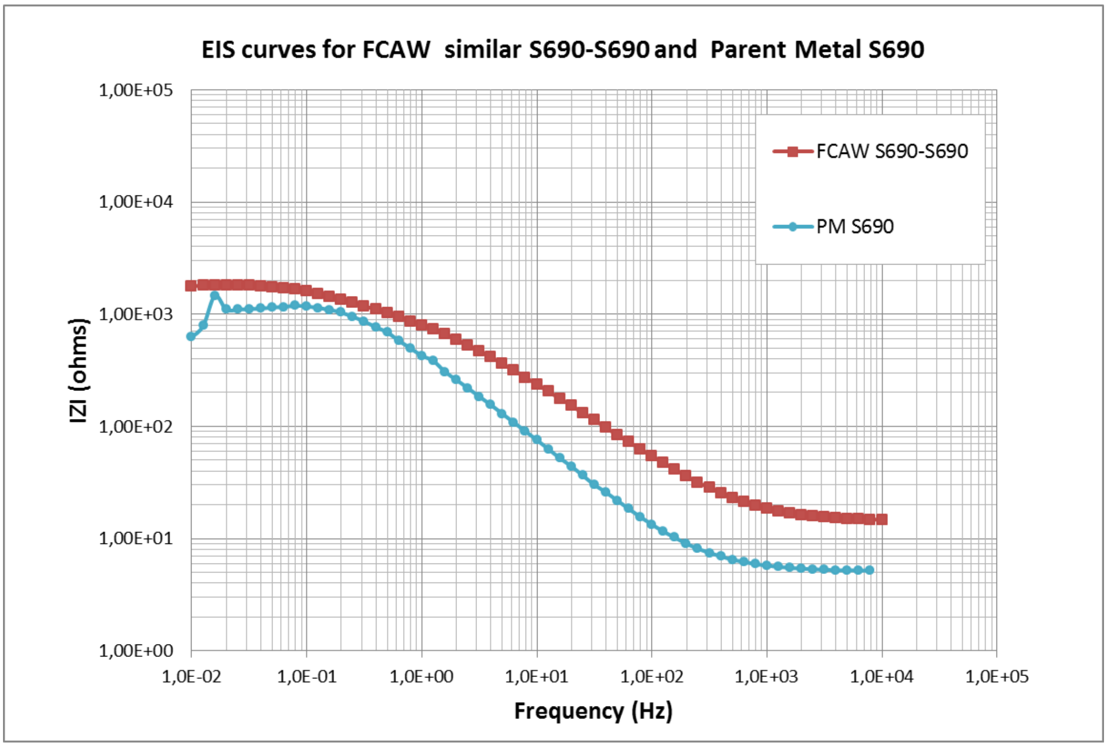

Fig. 4.56. Bode diagram for parent metal S690 and FCAW S690-S690

Chapter 5: Conclusions

The purpose of the thesis is to study and compare the corrosion behavior of arc welding, a conventional welding method (FCAW), with the friction stir welding (FSW), a new method of welding in shipbuilding.

For these welds, two different shipbuilding steels have been used: the common shipbuilding steel (AH36) and a high strength low alloy steel, (HSLA - S690).

The metallography of the welds and their micro-hardness are studied initially. The study of corrosion was made by two methods: electrochemical and standardized methods of accelerated aging in a salt spray chamber. Furthermore, it was attempted to measure the three-dimensional shape of a corroded specimen's surface and compare it with the surface of a non-corroded one, by using a structured white light 3D scanner.

The conclusions that are imported by this work are the following:

Regarding material properties:

- Ferritic-perlitic microstructure was observed for parent metal AH36 (strong orientation, due to the production process (rolling) of the steel plates), while the microstructure of S690 consists of perlite, bainite and martensite recovery.
- The microstructure in the weld root presents ferrite and perlite,while the microstructure in the Stir Zone presents acicular ferrite Widmastätten and perlite for AH36-AH36 FSW.
- For S690-S690 FCAW: The HAZ in the 1st pass of the weld presents microstructure that consists of recovered martensite, ferrite, bainite and small amounts of remaining austenite, when in the interface of the last 4th pass and the pass epitaxial growth of grains is observed. The microstructure in the root of the weld consists of ferrite and bainite and presents dendritic formation of grains.

The main conclusions of the micro-hardness measurements are listed below:

- The average hardness of AH36 is 180 Vickers. S690 has clearly higher hardness, at 280 Vickers.
- The highest values of hardness were observed for similar S690 FCAW, vertical to the welding, along the axis of the welding (270HV to 310HV).
- The lower values were observed, at HAZ for the similar S690 FCAW, where the values fall to 200HV. Same values were measured for similar AH36 FSW at HAZ.

Accelerating Tests in the Salt Spray Chamber showed these:

- The average corrosion rate for the AH36 Parent Metal specimens is 4,398±0,49 mm/year.
- The average corrosion rate for the S690 Parent Metal specimens is 3,853±0,67 mm/year.
- The S690 presents lower corrosion rate than AH36 Parent Metal (Fig. 4.20).
- The average corrosion rate for the S690 FCAW specimens is 3,274±045 mm/year.
- The average corrosion rate for the AH36 FSW Parent Metal specimens is 3,591±058 mm/year.
- The FSW specimens present lower corrosion rate than FCAW specimens.
- The highest corrosion rates show the interval specimens with small exposure times.
- For regular specimens observed increase in corrosion rate with increasing exposure cycles.
- In contrast, the corrosion rate of the interval specimens begins with high values and then decreases.
- For both welds (FCAW and FSW) is observed that the corrosion rate is lower than their Parent Metal corrosion rate.
- With the increase in exposure cycles, the values of corrosion rate of regular and interval and specimens seem to converge (specimens that were exposed in the chamber for 60-70 cycles).
- The corrosion depth of the specimens increases almost linearly versus the exposure time for the specimens in the chamber, as expected.

From structured white light 3D scanning, these conclusions below were noted:

- The grids, by Rapidform XOR3, of S690 parent metal, after 15 days of exposure reveal, that the maximum depth of the pits is identified, noticed with orange color, and is measured up to 0.1513 mm ***(Fig.4.34b).*** The grid acquired with cloud compare software shows that a general diminuition of the surface is detected, colored in light green and yellow color. According to the legend 0.15mm diminution is measured ***(Fig.4.34 c).*** The results of the two different softwares are in agreement.
- After 30 days of exposure, for S690 parent metal specimen, deeper pits are macroscopically noticed (Fig. 4.35 a). The grid by Rapidform XOR3 reveals that some pits of 0.4mm are recognized and one pit is measured up to 0.5114mm depth (Fig. 4.35b). The same results are obtained from Cloudcompare software, presented with light red – orange color, indicating depth around 0.45mm (Fig. 4.35c).

- For FCAW S690-S690 welded specimen, only small pits are detected on the weld seam (Fig 4.36). However the pits detected rise up to 0.5944mm (by Rapidform XOR3) (Fig. 4.35b). Similar value for the same spot is measured by CloudCompare software, indicated with dark red color (Fig. 4.35c). Both methods present the same patter for the relief of the corroded surface. It should be noticed that the deeper values detected after 15 days exposure for FCAW S690-S690 welded specimen is higher than these recorded for the parent metal, for the same exposure time (see Fig. 4.34).
- After 30 days of exposure, still no significant pits are detected on the weld seam, for FCAW S690 specimen ***(Fig. 4.37).*** However now a general diminuition of the surface is revealed, more abundant are deep pits and value up to 0.6704mm is recorded ***(Fig. 4.37b)***. The same pattern for the relief of the surface is indicated by CloudCompare image ***(Fig. 4.37c)***. (b and c images are upside down)
- Friction Stir Welded AH36-AH36 specimen, after 15 days of exposure, show several pits of around 0.15-0.20 mm, concentrated mainly in one side of the weld ***(Fig. 4.38).*** One pit of 0.4mm is also noticed ***(Fig. 4.38b)***.
- However, after 30 days of exposure the pit depth is increased and several areas of pitting around 0.3-0.4mm is noticed ***(Fig. 4.39)***. The pitting is spread in the whole area of the specimen ***(Fig. 4.39).***

The conclusions below were imported from the results of electrochemical measurements:

- For parent metals: i_{corr} is almost 10μA/cm^2 for S690 and 5μA/cm^2 for AH36. Ecorr is 700mV for AH36 and -650mV for S690.
- The comparison reveals that Ecorr that both parent metal S690 and FCAW S690-S690 present similar corrosion behavior concerning the Ecorr -670mV - -680mV, while the icorr values are double for parent metal S690, (5μA/cm^2 for FCAW and 10μA/cm^2 for parent metal).
- Ecorr for FSW AH36-AH36 is higher than parent metal AH36, implying lower susceptibility to corrosion, while the icorr values are higher for AH36 parent metal and FSW AH36-AH36 are rather similar (2μA/cm^2 and 5μA/cm^2 respectively) indicating similar corrosion rates.

The values of Ecorr, icorr and Rp (polarization resistance) for parent metals AH36, S690, did not show significant differences. The corresponding values for the S690-S690 similar FCAW and similar AH36-AH36 FSW have similar behavior.

In conclusion, it should be noted that the two metals and their welds do not show great difference in their corrosion behavior.

Chapter 6: References

[1] ASTM G 31 - 72, "Standard Practice for Laboratory Immersion Corrosion Testing Metals," (Reapproved 1999).

[2] British Standard EN 1043 - 1:1996, "Destructive tests on welds in metallic materials. Hardness testing - Part 1: Hardness test on arc welded joints".

[3] ISO 14993:2001 (E), "Corrosion of metals and alloys – Accelerated testing involving cyclic exposure to salt mist, “dry”and “wet” conditions".

[4] ISO 8407:1991 (E), "Corrosion of metals and alloys - Removal of corrosion products from corrosion specimens"".

[5] British Standard EN 1321:1997, "Destructive tests on welds in metallic materials - Macroscopic and microscopic examination welds".

[6] Παντελής Δ.Ι., Χρυσουλάκης Γ.Δ., "Επιστήμη και Τεχνολογία Μεταλλικών Υλικών", Αθήνα: Παπασωτηρίου, 2007.

[7] Παπάζογλου Β.Ι., "Επιστήμη και τεχνολογία των συγκολλήσεων", Αθήνα: Παπασωτηρίου, 1995.

[8] Abilio M. P. de Jesus, Rui Matos, Bruno F. C. Fontoura, Carlos Rebelo, Luis Simoes da Silva, Milan Veljkovic, "A comparison of the fatiqge behavior between S355 and S690 steel grades", *Journal of constructional steel research,* pp. 140-150, 2012.

[9] ABS (American Bureau of Shipping), "Rules for Materials and Welding, Part 2",2014.

[10] "ASM Handbook," vol. 134, 2003.

[11] ASM International, "Corrosion of Weldments", 2006.

[12] American Welding Society, "Fusion Welding Processes", Miami, AWS, 2003.

[13] Babu S.S. David, S.A. Quintana, M.A., "Modelling microstructure development in selfshielded FCAW", *Welding Journal,* pp. 80(4): 91s-97s, 2001.

[14] Gadallah R., Fahmy R., Khalifa T, "Influence of Shielding Gas Composition on the properties of Flux-Cored Arc Welds of Plain Crbon Steel", *International Journal of Engineering ant Technology Innovation,* vol. 2, no. Cairo, 2012.

[15] IACS (International Accociation of Classification Sosieties), ""Requirements concering Materials and Welding", 2014.

[16] Jones D. A., "Principles and prevention of corrosion - 2nd edition", 2014.

[17] Kobe Steel Ltd., "Essential Factors in Gas Metal Arc Welding 4th edition", Tokyo, 2011.

[18] Myers T., "Choosing a shielding gas for FCAW", *Welding Journal,* pp. 89(3): 30-33.

[19] "Operating Manual Q. Fog Cyclic Corrosion".

[20] Mystica Augustine Michael Duke, "Friction Stir Welding of Steel," *International Journal of Research in Engineering and Technology.*

[21] N. B. Mostafa, M. N. Khajavi "Optimization of Welding Parametrs for Weld Penetration in FCAW", *Jouranl of Achievements in Materials and Manufacturing Engineeiring, Iran,* vol. 16, no. 1-2, 2006.

[22] R. A. Ricks, P. R. Howell, G. S. Barritte, "The nature of acicular ferrite in HSLA steel weld metals", *Journal of Materials Science,* 1992.

[23] R. S. Mishra, Z. Y. Ma, ""Friction Stir Welding and proccesing".," *Materials Science and Enginnering,* pp. 1-78, 2005.

[24] Sindo Kou, "Welding Metallurgy, second edition", 2003.

[25] [Online]. Available: http://um3d.dc.umich.edu/wp-content/uploads/2012/07/7-toolmark.jpg

[26] [Online]. Available: http://www.csm-instruments.com/Vickers-indentation-using-CSMs-Micro-Scratch-Tester

[27] [Online]. Available: http://www.gim-international.com/issues/articles/id1666-Structured_Light_Scanners.html

[28] [Online]. Available: https://www.hera.org.nz/Category?Action=View&Category_id=522

[29] [Online]. Available: http://www.iiviinfrared.com/1-Micron-Optics-Materials/1micron-laser-overview.html

[30] [Online]. Available: http://www.metals4u.co.uk/How-to-Mig-Weld.asp

[31] [Online]. Available: http://www.substech.com/dokuwiki/doku.php?id=metallurgical_microscope

[32] [Online]. Available: http://www.thefullwiki.org/Structured-light_3D_scanner

[33] [Online]. Available: http://www.spartial-vision-inspection-features

[34] [Online]. Available: http://www.twi-global.com/technical-knowledge/job-knowledge/hardness-testing-part-1-074/

[35] [Online]. Available: http://www.gamry.com

ANNEXES

ANNEX A: Calendar Program of Installation - Removal of Specimens from the Salt Spray Chamber

January 2015

Monday	Tuesday	Wednesday	Thursday	Friday	Saturday	Sunday
			1	**2**	**3**	**4**
5	**6**	**7**		**9**	**10**	**11**
12	**13**	**14** Beginning of the test, Enter: PM: HC1, HC2, HC3, HC5, IA1, HC6, HC7, HC8, HC9, HC10, HC11, IB1, IIIA1, IIIA3 FSW: S40002, S40003, S40004, S40005, S40006, S40008, S40009 FCAW: IIA2, IIB2, IA2, IC2, IIC2, IB2, VA2	**15**	**16**	**17**	**18**
19 Enter: PM: IIC1*, IIC3* FSW: S400013* FCAW: IVB2* Exit: PM: HC1, HC2 FSW: S40002 FCAW: IIA2	**20**	**21**	**22**	**23**	**24** Enter: PM: IIB1*, IIB3* FSW: S400012* FCAW: IVA2* Exit: PM: HC6, IIIA1 FSW: S40005 FCAW: VA2	**25**
26	**27**		**29** Enter: PM: IIA1*, IIA3* FSW: S400011* FCAW: IIIC2* Exit: PM: HC5, IA1 FSW: S40009 FCAW: IA2	**30**	**31**	

February 2015

Monday	Tuesday	Wednesday	Thursday	Friday	Saturday	Sunday
						1
2	**3** Enter: PM: IC1*, IC3* FSW: S400010* FCAW: IIIB2* Exit: PM: HC7, HC8 FSW: S40004 FCAW: IC2	**4**	**4**	**6**	**7**	**8** Enter: PM: IA3*, IB3* FSW: S40007* FCAW: IIIA2* Exit: PM: HC9, HC10 FSW: S40003 FCAW: IIC2
9	**10**	**11**	**12**	**13** End of the test Exit: PM: IA3*, IB3*, IC1*, IC3*, IIA1*, IIA3*, IIB1*, IIB3*, IIC1*, IIC3*, IB1, HC11, IIIA3, HC3 FSW: S40007*, S400010*, S400011*, S400013, S400012*, S40008, S40006 FCAW: IIIA2*, IIIB2*, IIIC2*, IVA2*, IVB2*, IB2, IIB2	**14**	**15**
16	**17**	**18**	**19**	**20**	**21**	**22**
23	**24**	**25**	**26**	**27**	**27**	

Note: At the tables above, the specimens which are written in blue are the parent metal specimens, in orange are the similar AH36 friction stir welding specimens and in black are the similar S690 FCAW specimens. Also, the specimens by an asterisk (*) are the interval ones. Finally, for each specimen, the described procedure of chapter 4 was followed.

Specimens of Parent Metal S690

In the following pages are presented the parent metal specimens: the sandblasted surface, the corroded surface after the exposure in accelerated weathering testing and the cleaned surface after the removal of corrosion products, for a certain number of cycles: 15, 30, 45, 60, 75, 90, for the regular and the interval specimens (Dimensioning 70x100x12 mm^3).

HC1 (5 Days - 15 Cycles)

The sandblasted surface

The corroded surface

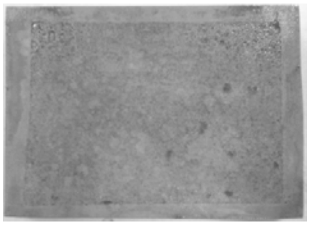

The cleaned surface

HC2 (5 Days - 15 Cycles)

The sandblasted surface

The corroded surface

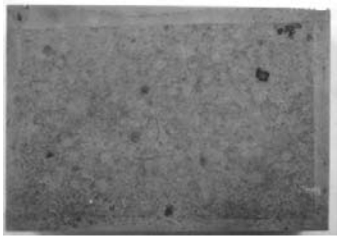

The cleaned surface

IA3 - Interval 5 Days - 15 Cycles)

The sandblasted surface

The corroded surface

The cleaned surface

IB3 – Interval (5 Days - 15 Cycles)

The sandblasted surface

The corroded surface

The cleaned surface

IIIA1 (10 Days - 30 Cycles)

The sandblasted surface

The corroded surface

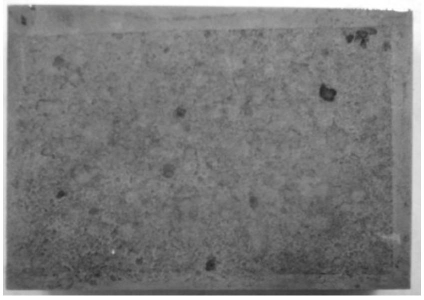

The cleaned surface

HC6 (10 Days - 30 Cycles)

The sandblasted surface

The corroded surface

The cleaned surface

ANNEX B: Specimens before and after their exposure into the Salt Spray Chamber

IC1 - Interval (10 Days - 30 Cycles)

The sandblasted surface

The corroded surface

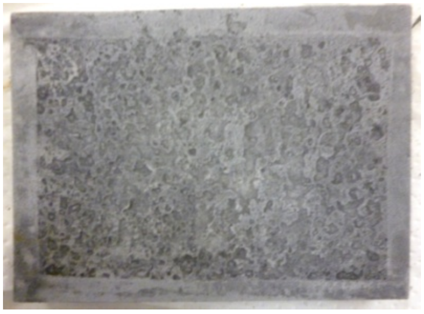

The cleaned surface

IC3 - Interval (10 Days - 30 Cycles)

The sandblasted surface

The corroded surface

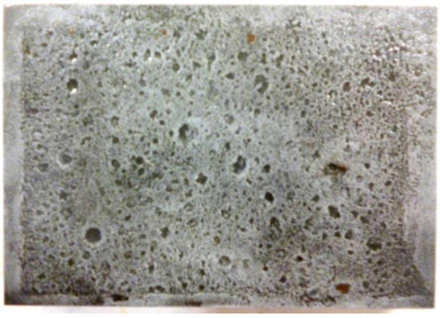

The cleaned surface

IA1 (15 Days - 45 Cycles)

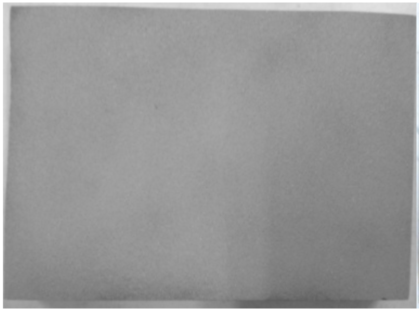
The sandblasted surface


The corroded surface

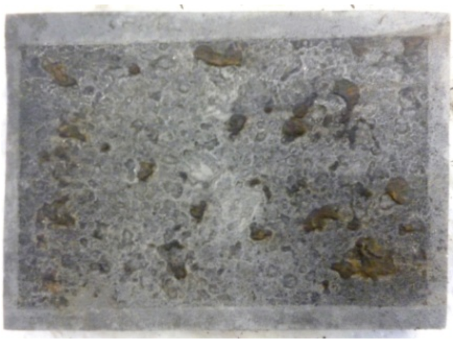
The cleaned surface

HC5 (15 Days - 45 Cycles)


The sandblasted surface


The corroded surface

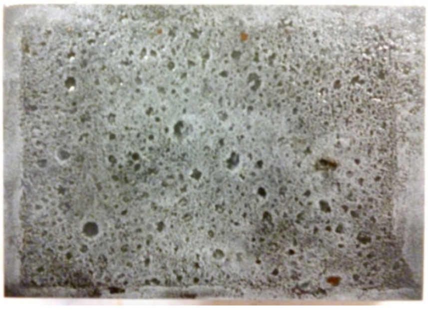
The cleaned surface

IIA1 - Interval (15 Days - 45 Cycles)

The sandblasted surface

The corroded surface

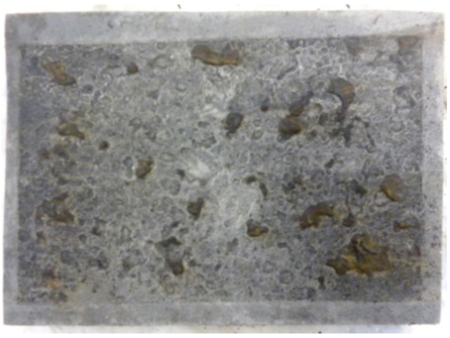

The cleaned surface

IIA3 - Interval (15 Days - 45 Cycles)

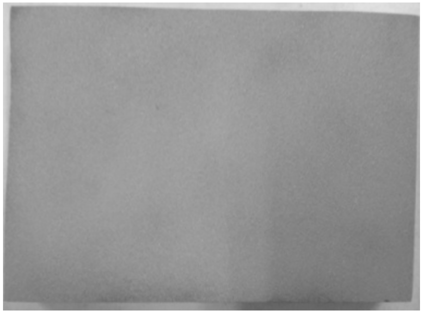

The sandblasted surface

The corroded surface

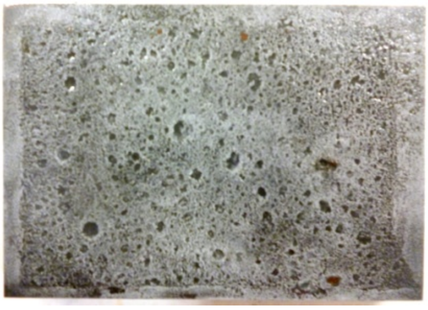

The cleaned surface

HC7 (20 Days - 60 Cycles)

The sandblasted surface

The corroded surface

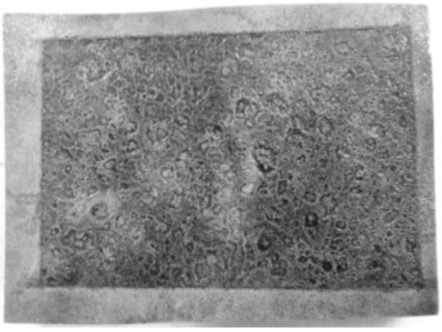

The cleaned surface

HC8 (20 Days - 60 Cycles)

The sandblasted surface

The corroded surface

The cleaned surface

IIB1 - Interval (20 Days - 60 Cycles)

The sandblasted surface

The corroded surface

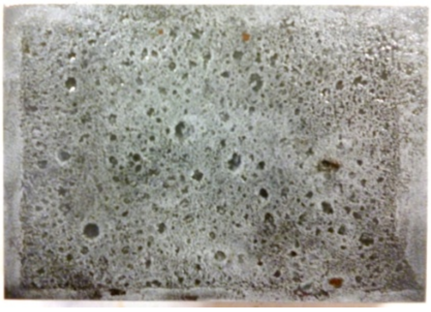

The cleaned surface

IIB3 - Interval (20 Days - 60 Cycles)

The sandblasted surface

The corroded surface

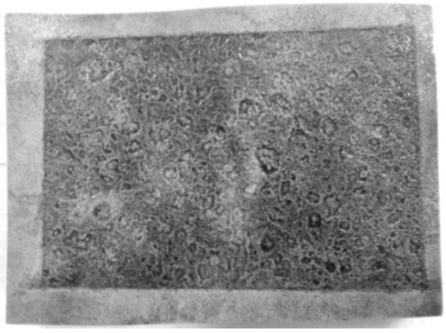

The cleaned surface

HC9 (25 Days - 75 Cycles)

The sandblasted surface

The corroded surface

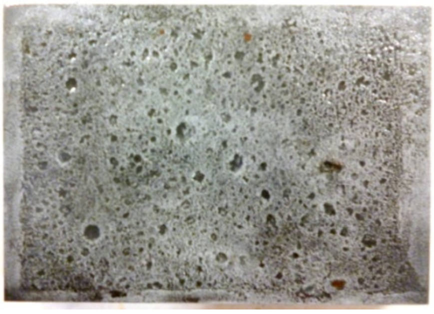

The cleaned surface

HC10 (25 Days - 75 Cycles)

The sandblasted surface

The corroded surface

The cleaned surface

IIC1 - Interval (25 Days - 75 Cycles)

The sandblasted surface

The corroded surface

The cleaned surface

IIC3 - Interval (25 Days - 75 Cycles)

The sandblasted surface

The corroded surface

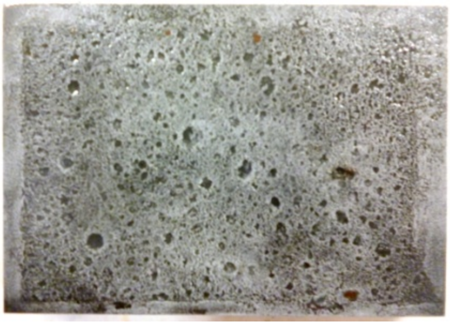

The cleaned surface

IB1 (30 Days - 90 Cycles)


The sandblasted surface


The corroded surface

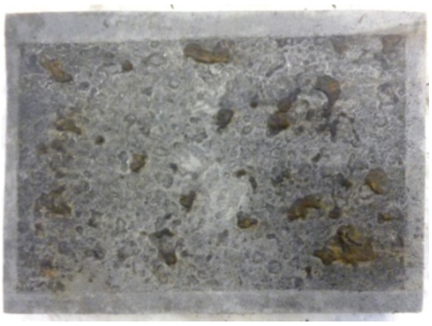
The cleaned surface

HC11 (30 Days - 90 Cycles)


The sandblasted surface


The corroded surface


The cleaned surface

IIIA3 (30 Days - 90 Cycles)

The sandblasted surface *The corroded surface*

The cleaned surface

HC3 (30 Days - 90 Cycles)

The sandblasted surface

The corroded surface

The cleaned surface

12 Specimens of Arc Welding S690 - S690

In the following pages are presented the arc welded specimens : the sandblasted surface, the corroded surface after the exposure in accelerated weathering testing and the cleaned surface after the removal of corrosion products, for a certain number of cycles : 15, 30, 45, 60, 75, 90 , for the regular and the interval specimens (Dimensioning 70x110x12 mm^3).

IIA2 (5 Days - 15 Cycles)

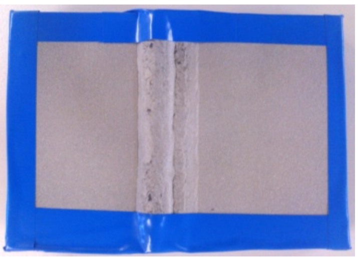

The sandblasted surface *The corroded surface*

The cleaned surface

IIIA2- Interval (5 Days - 15 Cycles)

The sandblasted surface *The corroded surface*

The cleaned surface

ANNEX B: Specimens before and after their exposure into the Salt Spray Chamber

VA2 (10 Days - 30 Cycles)

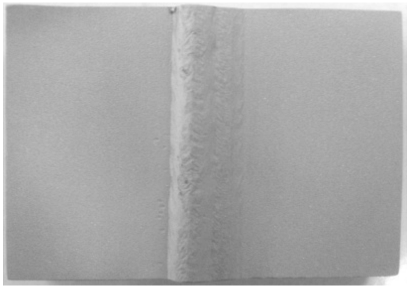

The sandblasted surface

The corroded surface

The cleaned surface

IIIB2- Interval (10 Days - 30 Cycles)

The sandblasted surface

The corroded surface

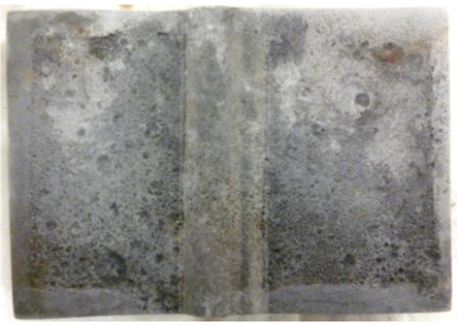

The cleaned surface

IA2 (15 Days - 45 Cycles)

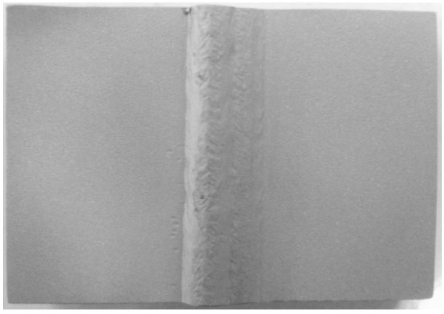

The sandblasted surface

The corroded surface

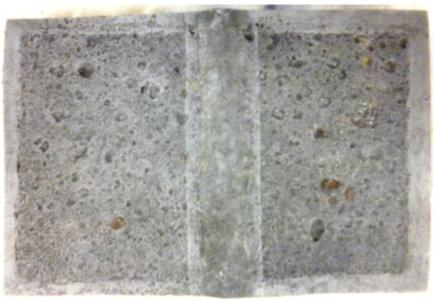

The cleaned surface

IIIC2- Interval (15 Days - 45 Cycles)

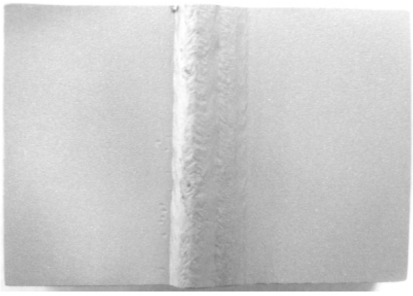

The sandblasted surface

The corroded surface

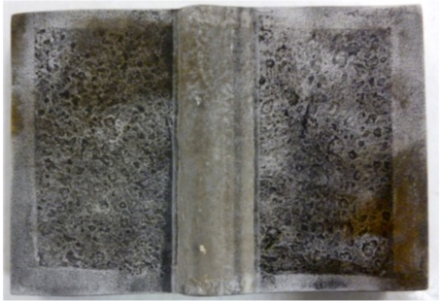

The cleaned surface

IC2 (20 Days - 60 Cycles)

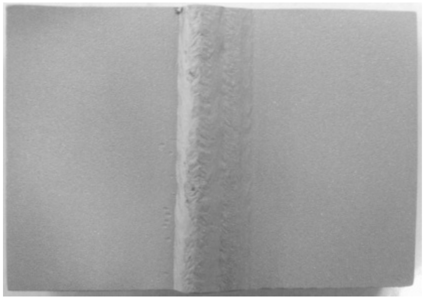

The sandblasted surface

The corroded surface

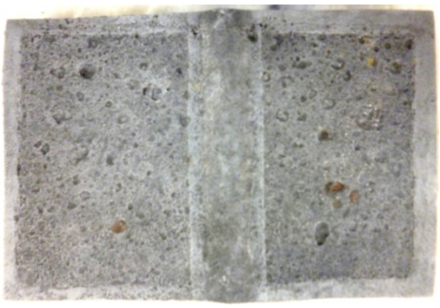

The cleaned surface

IVA2- Interval (20 Days - 60 Cycles)

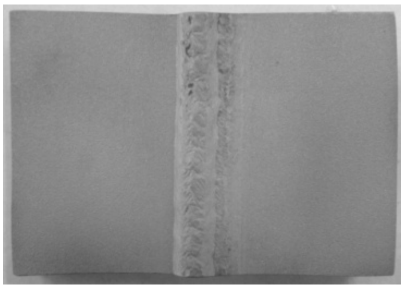

The sandblasted surface

The corroded surface

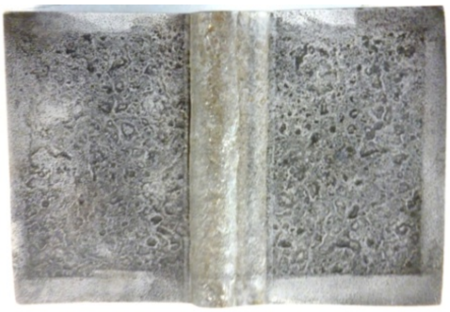

The cleaned surface

IIC2 (25 Days - 75 Cycles)

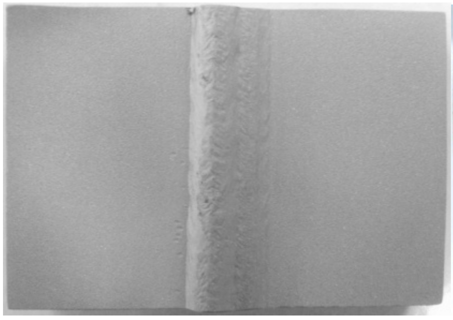

The sandblasted surface

The corroded surface

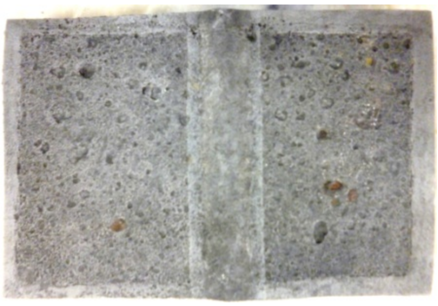

The cleaned surface

IVB2- Interval (25 Days - 75 Cycles)

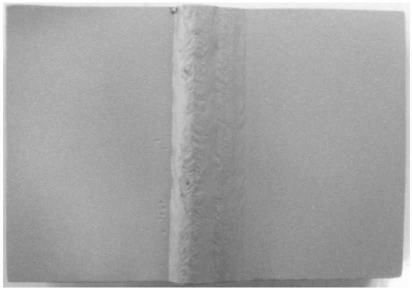

The sandblasted surface

The corroded surface

The cleaned surface

IB2 (30 Days - 90 Cycles)

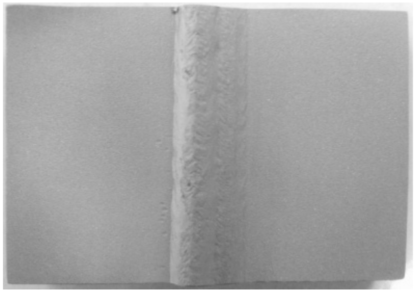

The sandblasted surface

The corroded surface

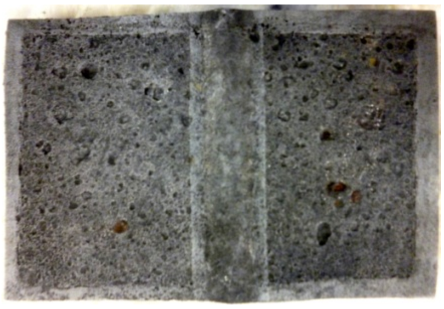

The cleaned surface

IIB2 (30 Days - 90 Cycles)

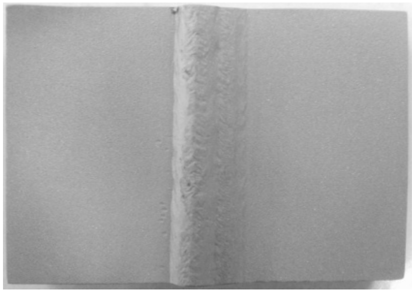

The sandblasted surface

The corroded surface

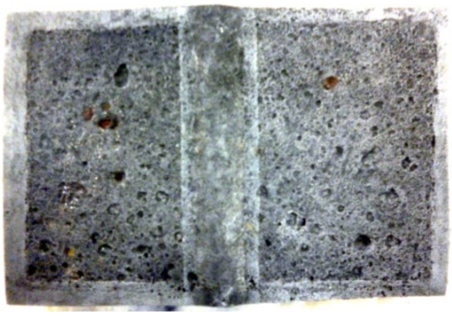

The cleaned surface

12 Specimens of Friction Stir Welding AH36 - AH36

In the following pages are presented the FSW specimens : the sandblasted surface, the corroded surface after the exposure in accelerated weathering testing and the cleaned surface after the removal of corrosion products, for a certain number of cycles : 15, 30, 45, 60, 75, 90 , for the regular and the interval specimens. (Dimensioning 70x100x12 mm^3)

S40002 (5 Days - 15 Cycles)

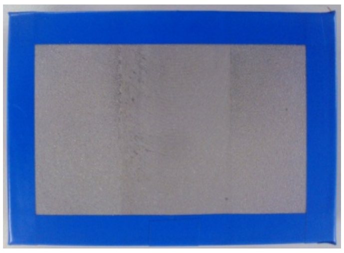

The sandblasted surface

The corroded surface

The cleaned surface

S40007- Interval (5 Days - 15 Cycles)

The sandblasted surface

The corroded surface

The cleaned surface

ANNEX B: Specimens before and after their exposure into the Salt Spray Chamber

S40005 (10 Days - 30 Cycles)

The sandblasted surface

The corroded surface

The cleaned surface

S400010- Interval (10 Days - 30 Cycles)

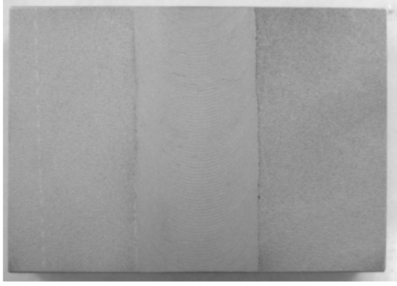

The sandblasted surface

The corroded surface

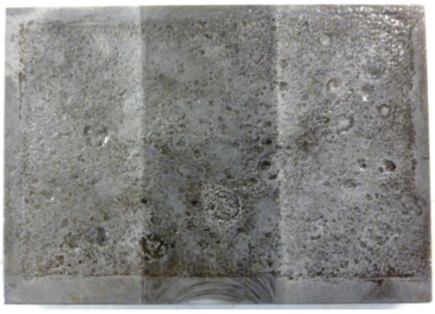

The cleaned surface

S40009 (15 Days - 45 Cycles)

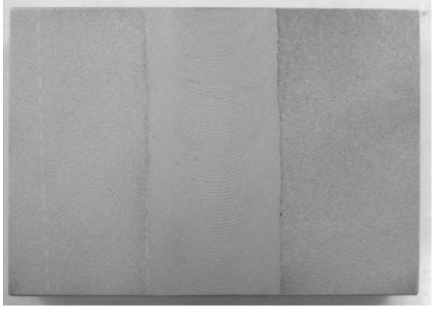

The sandblasted surface

The corroded surface

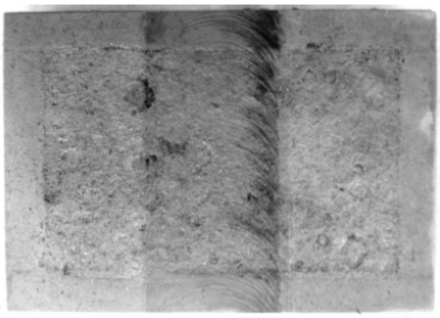

The cleaned surface

S400011- Interval (15 Days - 45 Cycles)

The sandblasted surface

The corroded surface

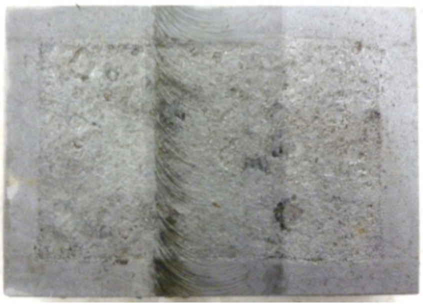

The cleaned surface

ANNEX B: Specimens before and after their exposure into the Salt Spray Chamber

S40004 (20 Days - 60 Cycles)

The sandblasted surface

The corroded surface

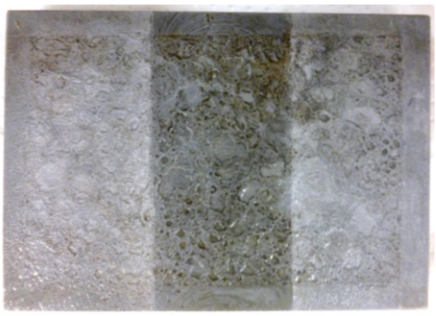

The cleaned surface

S400012- Interval (20 Days - 60 Cycles)

The sandblasted surface

The corroded surface

The cleaned surface

S40003 (25 Days - 75 Cycles)

The sandblasted surface

The corroded surface

The cleaned surface

S400013- Interval (25 Days - 75 Cycles)

The sandblasted surface

The corroded surface

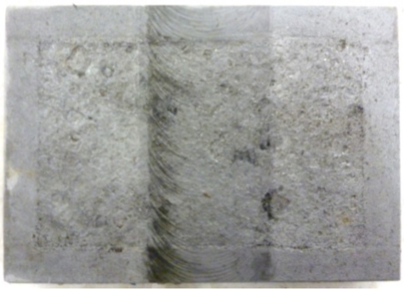

The cleaned surface

S40008 (30 Days - 90 Cycles)

The sandblasted surface

The corroded surface

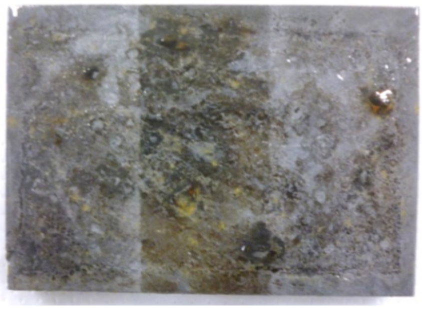

The cleaned surface

S40008 (30 Days - 90 Cycles)

The sandblasted surface

The corroded surface

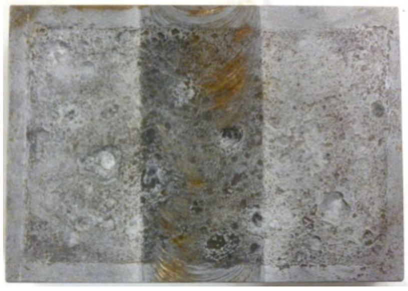

The cleaned surface

Note: In the second picture of each group of specimens, it is seemed the imprint of the blue adhesive tape, with which we covered the one side of each specimen.